Technical University of Berlin
Mechanical Engineering and Transport Systems
Institute of Aeronautics and Astronautics
Chair of Aircraft Design and Aerostructures

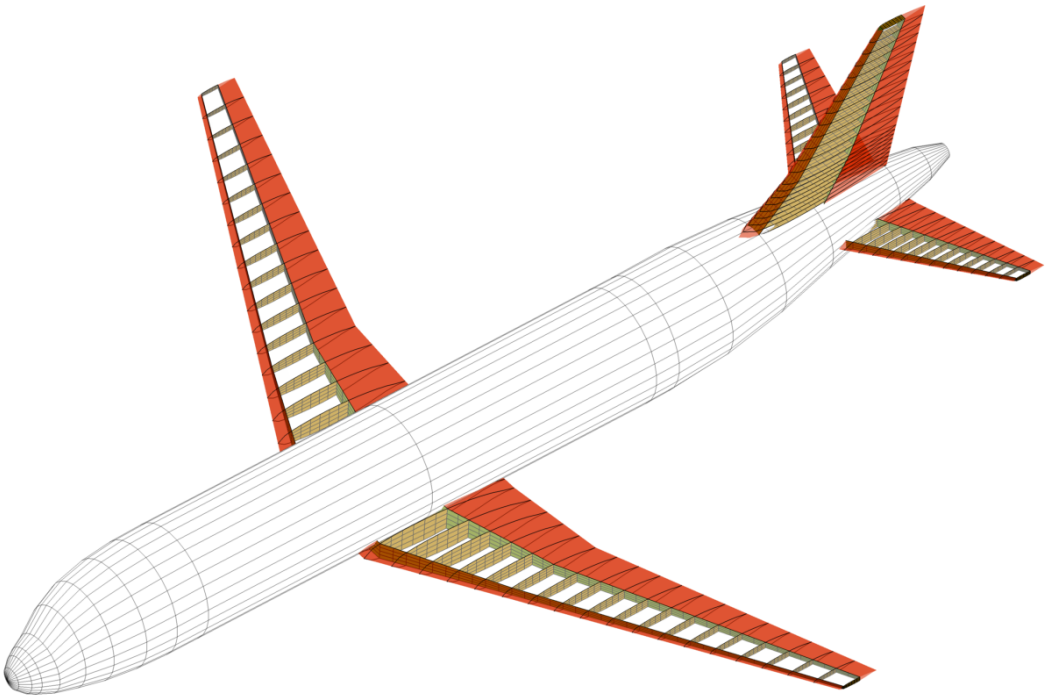

Development of a Structural Modelling Tool During the Conceptual Design Phase

Author
Kağan Atçı

Matriculation 338131
B.Sc. TU Berlin, 2016

Supervisor
Prof. Dr. Ing. Andreas Bardenhagen

Advisor
Claire Helene Jacob, M.Sc.

Thesis Submitted in Partial Fulfillment of the Requirements for the Degree of Master of Science in Aerospace Engineering

Berlin, August 15th 2018

Abstract

The demand for automation in product research and development has significantly increased over the years. This situation has also been impacting the aerospace domain, as institutes from various disciplines are striving to expand their knowledge into an automated multidisciplinary design and optimization environment. As part of this fact, a knowledge-based application named Structural Modeling Tool (SMT) has been developed at the Institute of Aeronautics and Astronautics of TU Berlin.

The objective of SMT is to generate parametric structural wing box models for pre-generated wing geometries with a high aspect ratio in CPACS format autonomously. The structural modeling sequence consists of two sub-sequences: model generation and model optimization. In model generation block, an initial wing box model is parameterized based on conventional aircraft structure elements (Spars, Ribs, and Wing Covers). This is followed by generating the finite element model of the structural geometry and external loads, as well as the computation of the structural mass in reference to finite element geometry and input material. During model optimization, the finite element wing box model is analyzed for every input load case concerning von Mises stress and buckle displacements. Based on these outputs, the wing box model is iteratively optimized regarding stress and stability (buckle) criteria, by sizing the parts and modifying the structural layout. As the final step of the model optimization sequence, an optimal model is combined using the parts with the highest stiffness resulted from every load case.

This thesis is dedicated to detail the concept of the developed SMT and it's functionality in six chapters. In the first chapter the main concept is introduced based on the literature study. In second chapter, the theoretical background of the developed concept is introduced. The third chapter describes the flow of the model generation sequence through steps, conditions, rules, and capabilities. Similarly, the model optimization sequence is elaborated in the fourth chapter. In the fifth chapter, a test application of SMT is performed using the wing of a reference aircraft in flight conditions referred to the related certification codes of EASA and the results are discussed. These parts are concluded with a summary of the mentioned structural parts and recommendations of the author for future works in the final chapter.

Keywords: Wing Box Modeling, Structural Sizing, Topology Optimization, Knowledge-Based Engineering, CPACS, Finite Element Analysis

Zusammenfassung

Die Nachfrage an Automatisierung in Produktforschung und -entwicklung ist in den letzten Jahren deutlich gestiegen. Diese Situation/Entwicklung hat auch Auswirkungen auf die Luft- und Raumfahrtbranche, in der Institute aus verschiedenen Disziplinen immer mehr anstreben Im Rahmen rahmen dieser Nachfrage wurde eine wissensbasierte (knowledge based) Anwendung für die Modellierung der Flügelstrukturen im Institut für Luft- und Raumfahrttechnik der Technischen Universität Berlin entwickelt.

Das Ziel der SMT liegt darin, parametrische Flügelstrukturen als sogenannte Wing-Box-Modelle, anhand der vorgegebenen hochgestreckten Flügelgeometrien in CPACS-Format automatisiert zu erzeugen. Die Strukturmodellierung teilt sich in zwei Module auf: Modellerzeugung und Modelloptimierung. Bei der Modellerzeugung wird ein erstes Wing-Box-Modell mithilfe von konventionellen Strukturelementen (Holme, Rippen und Flügelbehäutungen) des Leichtbaukonzepts parametrisiert. Infolge dessen erfolgt die Erzeugung des FE-Modells aus der Strukturgeometrie mit Schalenelementen, die Modellierung der Außen- und Flächenlasten als Knotenkräfte. Weiterhin wird die strukturelle Masse anhand der FE-Geometrie und des Eingabematerials berechnet. Während der Modelloptimierung wird das FE-Modell des parametrisierten Flügelkastens für jeden Input-Lastfall in Hinsicht auf von Mises Vergleichsspannung, sowie Beulfelder analysiert. Unter Berücksichtigung der Ausgabeparameter der FE-Analyse, findet ein iterativer Optimierungsprozess im Flügelkasten im Bezug auf Spannungs- und Beulkriterien statt. Bei diesem Optimierungsprozess geht es um Dickenanpassung der Flügelstrukturteile, sowie Modifizierung der Flügelstrukturtopologie. Als letzter Schritt der Modelloptimierung wird ein optimales Strukturmodell kombiniert, indem die optimierten Strukturteile, die sich aus allen Lastfällen ergeben, evaluiert werden.fällen ergeben, evaluiert werden.

Im Rahmen dieser Abschlussarbeit wurde die Entwicklung des SMT-Konzeptes und -Funktionalität beschrieben. Dieses Thema wird in sechs Kapiteln behandelt. Im ersten Kapitel wird das Hauptkonzept aufbauend auf die Literaturrecherche eingeführt. Im zweiten Kapitel werden die theoretischen Hintergründe des entwickelten Konzepts vorgestellt. Im dritten Kapitel wird der Ablauf der Modellgenerierung durch Schritte, Bedingungen, Regeln und Fähigkeiten dargestellt. Ähnlich wird die Modelloptimierung im vierten Kapitel erarbeitet. Eine Beispielanwendung der SMT an dem Tragflügel des Referenzflugzeugs CSR-01 und unter den von der EASA vorgeschriebenen Lastfällen, wird im fünften Kapitel demonstriert und die Ergebnisse nach verschiedenen Aspekten ausgewertet. Im Schlussteil der Arbeit werden diese Teile mit einer Zusammenfassung und Ausblick geschlussfolgert.

Contents

List of Tables

List of Figures

Nomenclature

Scalars

Δ	Difference operator between two values	–
ϵ	Normal strain	–
η	Relative chordwise coordinate	–
η	Relative spanwise coordinate	–
γ	Shear strain	–
λ	Eigenvalue	–
ν	Poisson's ratio	Pa
ρ	Density	$\frac{kg}{m^3}$
σ	Normal stress	Pa
σ_M	Mises stress	Pa
σ_{yield}	Yield stress	Pa
τ	Shear stress	Pa
a	Speed of sound	$\frac{m}{s}$
c	Aerodynamic coefficient	–
c_L	Lift coefficient at the ICA	–
E	Young's modulus	Pa
F	Concentrated load, Force	N
G	Shear modulus	Pa
g	Gravitational acceleration	$\frac{m}{s^2}$
k	Factor	–
m	Mass	kg

Ma	Mach-Number	$-$
N_{elem}	Number of elements	$-$
n_{LC}	Load factor of the load case	$-$
N_{size}	Iteration limit of the sizing optimization	$-$
N_{topol}	Iteration limit of the topology optimization	$-$
P	Pressure	Pa
T	Temperature	K
t	Thickness	m
u	Elastic displacement	m
V	Volume	m^3
v	Velocity	$\frac{m}{s}$
W	Work	J
X, Y, Z	Cartesian coordinates	m

Vectors

$\overline{\epsilon}$	Strain vector
$\overline{\sigma}$	Stress vector
$\overline{d}$	Nodal displacement vector
$\overline{d}_B$	Nodal displacement vector of the buckle analysis
$\overline{F}$	Concentrated load vector
$\overline{f}$	Nodal load vector
$\overline{p}$	Volume load vector
$\overline{q}$	Surface load vector
$\overline{u}$	Elastic displacement vector

Matrices

$\overline{\overline{\mathbf{D}}}$	Differential tensor
$\overline{\overline{\mathbf{E}}}$	Linear elasticity tensor
$\overline{\overline{\mathbf{G}}}$	Shape functions tensor
$\overline{\overline{\mathbf{I}}}$	Unit matrix
$\overline{\overline{\mathbf{K}}}$	Element stiffness matrix

$\overline{\overline{\mathbf{k}}}$ Analytical stiffness matrix

$\overline{\overline{\mathbf{K}}}_G$ Geometric element stiffness matrix

Indices

1, 2, 3 Directional indices with respect to Cartesian coordinates

λ Stability sizing value

σ Stress sizing value

air Value the air at an altitude

bf Block Fuel

$climb$ climb Fuel

col Value of an element column

$crit$ Critical value

cs Value of a component segment

$elem$ Value of an element

ext External

$fuel$ Value of a fuel type

i Counter index

ica Values regarding initial cruise altitude

int Internal

mat Value of a material type

max Maximum value

new Modified value

$part$ Value of a structural part

rel Relaxation value

s Value of a segment

$safe$ Safety margin value

$struc$ Value of the entire wing box structure

$targ$ Targeted value

thr Threshold value

tol	Tolerance value
txf	Taxi Fuel
$wing$	Value of a wing

Glossary

AI Artificial Intelligence

API Application Programming Interface

CAD Computer Aided Design

CeRAS Central Reference Aircraft data System

CFD Computational Fluid Dynamics

CFRP Carbon Fiber Reinforced Plastics

CPACS Common Parametric Aircraft Configuration Schema

CS Certifications and Specifications

CPU Central Processing Unit

DLR German Aerospace Center

DOF Degree of Freedom

EASA European Aviation Safety Agency

FEA Finite Element Analysis

GUI Graphical User Interface

HTP Horizontal Tail Plane

ICA Initial Cruising Altitude

ISA International Standard Atmosphere

KBE Knowledge-Based Engineering

KBS Knowledge-Based System

MAC Mean Aerodynamic Chord

MATLAB Matrix Laboratory

MDO Multidisciplinary Design Optimization

MTOW Maximum Take-Off Weight

RAM Random-Access Memory

SMT Structural Modeling Tool

TiGL TIVA Geometry Library

TiXI TIVA XML Interface

TIVA Technology Integration for the Virtual Aircraft

UID Unique Identifier

XML Extended Markup Language

XSD XML Schema Definition

Chapter 1

Introduction

Throughout the years of modern aviation, demands on decreasing noise and emissions, as well as costs of the aircraft have risen enormously. This consequence has motivated industries and institutions to develop alternative ways for a much efficient air transportation. In this regard, future visions such as Horizon 2020 [23], ACARE 2020 [8] and Flightpath 2050 [17] set by European Union indicates that the aircraft in the future will be significantly different from today's conventional configurations. Amongst new aircraft design concepts is the use of electrical systems including electrical engines. During the design phase of new configurations, high-quality numerical design tools provide the necessary flexibility and thus more effective results in the conceptual design phase, compared to conventional aircraft design processes.

As part of the new aircraft configuration researches, an application called Structural Modeling Tool (SMT) was developed, which enables automated modeling of wing structures in short time periods. During this development, various sources were researched and a new concept was generated. A glance of previous works that compose the fundamentals of the idea behind SMT is given in Section 1.1. Section 1.2 explains the focus of SMT and gives a quick overview of following chapters.

1.1 Previous Works

For the development of a feasible structural modeling concept, a wide range of scientific works has been researched. The literature research concentrates the development of structural modeling concept on four aspects.

The first aspect indicates the theoretical background and fundamental principles of the wing structure design. An essential work about this aspect was performed by M. C. Niu in [5], where he not only clarified the necessary knowledge for the fundamental elements of a wing structure, but also detailed the applications of these elements on conventional transport aircraft detailed.

The second aspect is concentrated on the model generation methodology of wing structures. As the increasing tendency on futuristic aircraft configurations caused traditional aircraft design methodology to become inadequate, new design methodologies were developed in order to fulfill this gap. A practical approach was made by Gianfranco La Rocca in his dissertation [19], where he developed a new design tool using KBE methodology to generate aircraft models in an MDO environment. Within the scope of this new concept, he introduced knowledge-based rules and methods for generating wing structure geometry amongst other aircraft parts. Another KBE application in wing modeling was developed by Felix Dorbath in his dissertation [26] and also in further publications [20], [21], [22]. In this application, an extended wing mass estimation system was implicated by physical modeling of the major and minor structural elements of the wing. A significant feature of this system is the use of CPACS format, which enables integrity into a toolchain process. The knowledge-based wing modeling capabilities, as well as the main idea for fuel modeling of this system using CPACS data format also contributed to the current application development. Further references regarding the aerodynamic load modeling were obtained from a DLR publication [32].

The third aspect represents the structural optimization of the generated model with sizing and topology optimization methods. A comprehensive sizing method was described by Florian Hürlimann utilizing algorithms and sizing criteria in [16]. The significant contribution of his work is the introduction of FEA based buckling criterion in iterative sizing process. Hürlimann also unveiled that during the optimization process, the use of high fidelity nodal forces has more impacts on the wing mass estimation, compared to local shear-moment-torsion loads.

The application and validation of the developed concept form the final aspect of this work. For the purpose of a realistic and redundant validation scenario, an aircraft geometry and statistical methods were considered. In this regard, a validated digital reference aircraft model was published by Central Reference Aircraft data System (CeRAS) [30], which is an open platform that provides reference aircraft data and methods to be used on academic and industrial researches. Apart from that, various empirical methods for the preliminary aircraft design with respect to geometry parameters, as well as aircraft performance parameters were introduced by Egbert Torenbeek in [3].

1.2 The Scope of this Work

This work mainly focuses on the development of an SMT for a Multidisciplinary Design Optimization (MDO) toolchain as a KBE application to proceed future aircraft configurations. In this regard, the primary goals of SMT are set. According to this, the tool must be able to determine the quantity, positioning, and thickness of the structural elements of an aircraft which fulfills the definitions of CS-25 in an iterative process. Furthermore, the tool must be sustainable for successors for further development. As a result of previous works and under the consideration of

the mentioned goals the central concept of SMT is demonstrated in Figure 1.1.

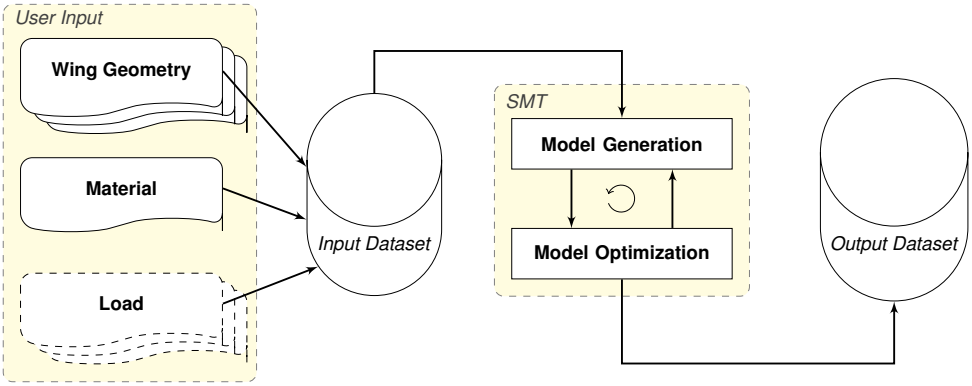

Figure 1.1 *Basic Concept of the Structural Modeling Tool*

Modeling of a wing structure basically takes place within the wing geometry, where this structure is optimized based on isotropic material and load conditions. In this regard, the user shall gather the data shown in "User Input" block in an input dataset. These elements shall be imported by SMT and processed iteratively in two segments: Model Generation and Model Optimization. In the model generation segment, a first topology of the wing structure shall be created and meshed afterward, where loads are to be distributed with respect to the meshed geometry. Model Optimization segment shall simulate the structure using Finite Element Analysis (FEA) results and optimize the structure, while the optimized structure is to be passed back to "Model Generation" segment in certain circumstances. This process shall be reiterated until a suitable structure is reached and exported in an output dataset. The implementation of this concept is structured in the following chapters:

Chapter 2 introduces fundamental elements in implementing SMT, such as used methodologies, data format and, used software, as well as the mathematical theory of FEA.

Chapter 3 is dedicated to Model Generation segment of SMT. In this chapter, procedures of model generation are described with flow charts, where requirements and capabilities are specified. Based on the literature study, structural elements to be used during the generation process are introduced, and preparation of the FEA geometry from the generated model is described.

Chapter 4 elaborates Model Optimization segment of SMT, where simulation and optimization processes of the generated models, as well as the evaluation of the best structural model, is detailed.

Chapter 5 presents a test application of SMT with two different aircraft models under same operating conditions. The goal of this chapter is to validate the reliability of SMT using application results in terms of optimization parameters such as structural weight and part thicknesses.

Chapter 6 summarizes the current work concerning goal achievements and results. Furthermore, possible enhancements in modeling and analysis capabilities are also mentioned in this chapter.

Chapter 2

Theoretical Background

The development of the SMT relies on various aspects and methods. The theory of the involved aspects and methods based on the literature studies are summarized in this chapter. An introduction to conventional wing structures with current applications in commercial aircraft is made in Section 2.1. The mathematical background of the structural analysis is presented in Section 2.2. In Section 2.3, the aircraft parametric data exchange format CPACS with its data structure and wing parametrization process is introduced. A general overview of Knowledge-Based Engineering, as well as its influences on developed SMT is given in Section 2.4. Lastly, a short glimpse of used tools and libraries during the development of SMT, is given in Section 2.5.

2.1 Conventional Wing Structures

The primary objective of a wing structure is to withstand the loads causing the wing to bend and twist during the take-off, flight and landing phases. In conventional wings of high-speed aircraft, the structure also carries engine and landing gear loads as well. Furthermore, the wing structure is used for housing the majority of the fuel. In order to fulfill these objectives with fewer compromises in terms of structural mass, wing structures are constructed with specific elements. Figure 2.1 shows the structural overview of a typical transport aircraft wing.

In theory, a conventional wing structure can be referred to a beam, gathering the set of loads and transferring to the fuselage through wing-fuselage attachment. For the purpose of transferring these gathered loads to the fuselage through the overall structure, wing covers stiffed with stringers, spars and ribs are used. The area, in which the wing structure is built up using these structural elements is called the wing-box area. Wing-box is bordered by spars in the chordwise direction, by ribs in spanwise directions and by wing covers on upper and lower side. Within the wing box area, secondary structural elements are placed, such as mount parts of engines, landing gears, high lift devices and wing-fuselage attachments. Regarding

the functionality, fuel tanks are also considered as secondary structural elements in this work. In the following, primary and secondary elements to be modeled in SMT are described in detail.

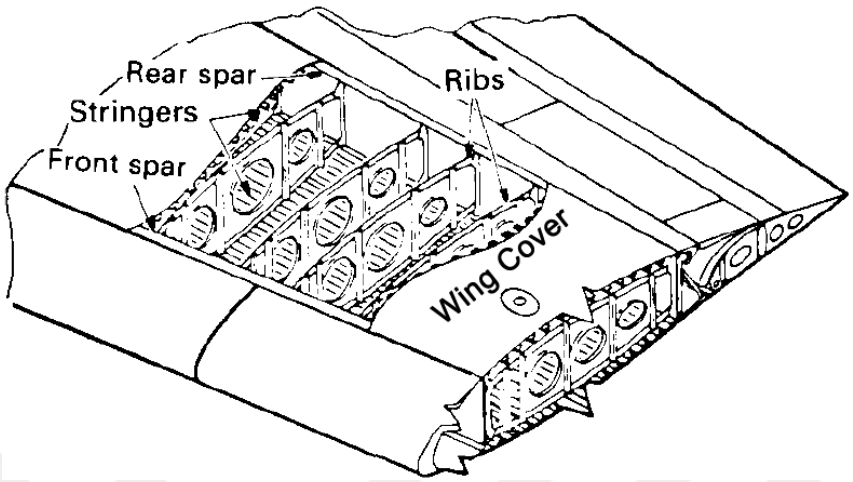

Figure 2.1 *Structural Overview of a Typical Commercial Transport Aircraft Wing [5]*

Wing Covers

Wing cover is basically the layer that encloses the parts of the wing, while the aerodynamic shape is maintained on the cover surface. As a structural element, wing covers typically represent fifty to seventy percent of the wing's structural weight [5]. Wing covers are responsible for taking the bending stresses throughout the wing structure. The upper cover is loaded primarily with compression, while the lower cover is loaded with tension. During the structural optimization, this variation of loading is taken into account in upper and lower covers. In commercial transport aircraft, wing covers are considered as main bending material, which are stiffened with stringers, integral stiffeners or sandwich panels [5] (see Figure 2.1).

Spars

Spar elements act as a cantilever beam structure. Air loads are transferred as shear loads from wing cover through ribs to spars. Despite the fact that increasing the number of spars may reduce the stress taken by the ribs in a wing structure, the structural design convention of commercial transport aircraft is concentrated mainly on two spar-configuration in high aspect ratio wings (typical commercial airplanes). The primary reason of this consequence the space requirements of housing the internal elements, such as fuel tanks, control devices and landing gear [5]. In two spar-configuration, the front spar is located close to leading edge, where high-lift slat devices are attached. Similarly, the rear spar is located in the area of flaps, control surfaces, and main landing gear. A general positioning of the front spar in

terms of relative chordwise coordinates is considered at $\xi = 0.15$ and of the rear spar at $\xi = 0.6$ [5].

Spar structures are grouped in two basic types as shear web and truss types. Shear web concept basically consists of upper and lower flanges attached to the main web (see Figure 2.2) that essentially carries shear loads, which finds a comprehensive application in commercial aircraft due to its efficiency. In truss concept, upper and lower flanges are mounted through diagonal or vertical trusses, which makes this concept suitable for aircraft in lighter categories.

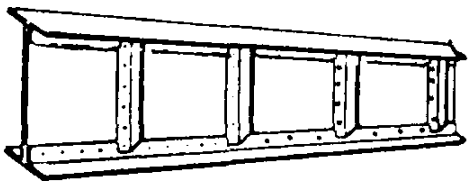

Figure 2.2 *Shear Web Spar [5]*

Ribs

Ribs take on multiple functionalities in wing structure. Primarily, ribs maintain the contour of the wing cover in chord direction, in order to prevent distortions in aerodynamic characteristics. Moreover, ribs contribute to the compressive strength of the wing cover and thus assures less stiffening elements to be integrated into wing structure. Another significant functionality of the ribs is to transfer and distribute air loads from wing cover to spars, as well as to support high-lift elements, engine pylons, and landing gears. Rib webs are also used as tank borders in wing box area. Similar to spars, ribs are constructed with the shear web (Figure 2.3) and truss concepts. In commercial transport aircraft, shear web ribs are preferred due to many features, such as inhibiting fuel from sloshing in the fuel tank or providing undistorted support against high internal tank pressures.

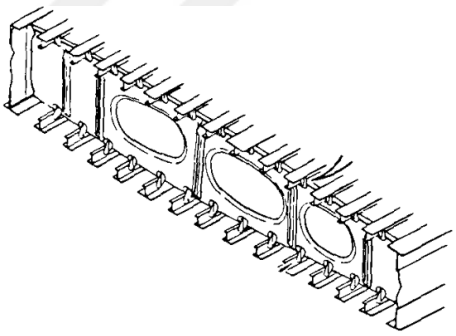

Figure 2.3 *Shear Web Rib [5]*

Parameters used for placing the ribs in the wing box area are rib spacings and rib arrangements. If the rib spacing is set too narrow, more ribs may lead to an increase in total rib weight, while decreasing the cover panel weight. In a converse scenario, larger rib spacing would keep the rib weight at a lower level, while increasing the weight of the cover panel. At this point, a variable rib spacing along the wingspan ensures a more optimal solution concerning structural weight. In swept wings, ribs are also arranged with respect to sweep angle around the vertical axis of the wing, which leads to further weight reduction in rib weight. These parameters cause a variation in rib numbers, depending on the wingspan, take-off weight and the number of engines mounted on the wing. Based on the study on [5], the number of ribs placed in a wing half of the commercial jet airplanes regarding their MTOW is gathered in Figure 2.4, where the black line shows the statistical trend.

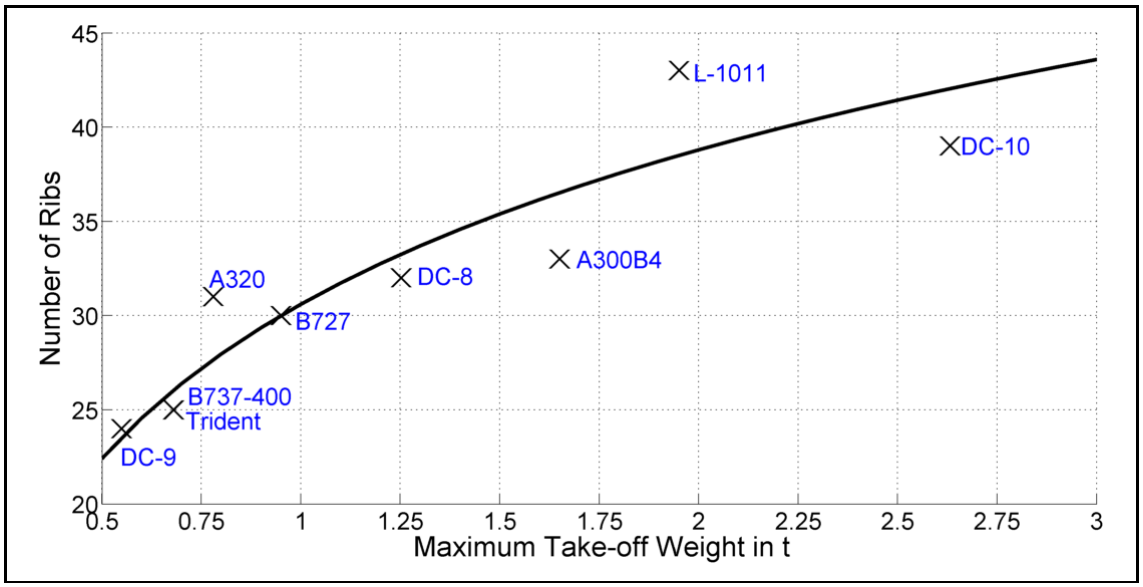

Figure 2.4 *Statistical MTOW - Rib Trend of Commercial Transport Aircraft [5]*

Wing-Fuselage Attachment

Wing-Fuselage attachment represents the definition of the center wing box area that is located inside the fuselage. In a typical design of commercial aircraft wings, one wing segment is dedicated to this area. As can be seen in Figure 2.5, this segment of the wing has no geometrical variety, such as sweep back or tapering, as well as no lifting surface outside of the CWB area.

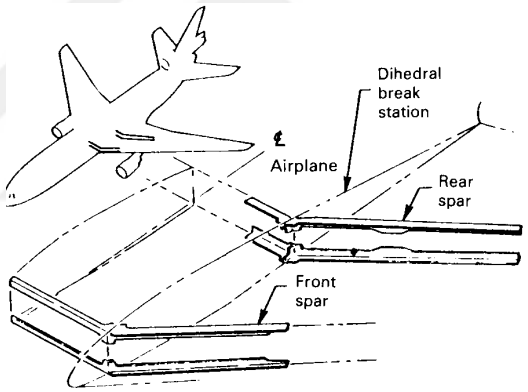

Figure 2.5 *Wing-Fuselage Attachment [5]*

Wings are attached to the fuselage at the wing root joint area (dihedral break station in Figure 2.5), where the main rib bulkhead is located. The wing structure is fitted to the fuselage using root fixed joint or wing root rotary joints, depending on the structural element through which the wing is attached.

Fuel Tanks

In commercial transport airplanes, a high proportion of the fuel is stowed in fuel tanks that are built in wing-box area, whereas fighter jets carry the fuel in the fuselage [5]. Stowing the fuel inside the wing is beneficial

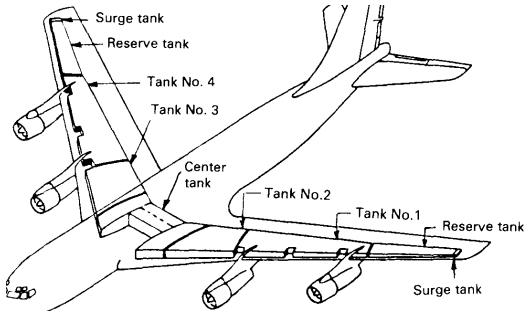

Figure 2.6 *Fuel Tank Segmentation [5]*

for high aspect ratio wings concerning structural relief and fuel management. The fuel counteracts to aerodynamic lifting force by its weight and reduces the maximum aerodynamic bending moment on the wing. Figure 2.6 shows a typical example of the fuel tank segmentation in a commercial transport airplane. In such case, the engine feeding starts at the center tank and passes on to outward tanks by turn. Hence a continuous counter load against aerodynamic lift is provided throughout the flight.

2.2 Mechanical Analysis

The mechanical analysis of the wing box takes place in Finite Element Analysis (FEA) environment using quadrilateral solid-shell elements in SMT, which also finds a broad application for lightweight structures as well. During FEA, the elastic deformations of the wing box model are obtained as a result of applied external loads. This section describes the theory behind this concept, starting with the basic theory of elasticity in Section 2.2.1. The extension of the basic elasticity in finite element approach including buckle analysis is elaborated in Section 2.2.2. Eventually, the solid shell element type is shortly introduced in Section 2.2.3.

2.2.1 Fundamentals of the Elasticity

The elastic deformation of a body in three-dimensional space is expressed with displacements $\overline{u}$, strains $\overline{\epsilon}$ and stresses $\overline{\sigma}$ [27] with

$$\overline{u} = \begin{bmatrix} u_1 & u_2 & u_3 \end{bmatrix}^T \tag{2.1}$$

$$\overline{\epsilon} = \begin{bmatrix} \epsilon_1 & \epsilon_2 & \epsilon_3 & \gamma_{12} & \gamma_{23} & \gamma_{31} \end{bmatrix}^T \tag{2.2}$$

$$\overline{\sigma} = \begin{bmatrix} \sigma_1 & \sigma_2 & \sigma_3 & \tau_{12} & \tau_{23} & \tau_{31} \end{bmatrix}^T \tag{2.3}$$

The relation between strains and displacements is given in the form of partial differentiation as follows

$$\overline{\epsilon} = \begin{bmatrix} \frac{\partial}{\partial x_1} & 0 & 0 \\ 0 & \frac{\partial}{\partial x_2} & 0 \\ 0 & 0 & \frac{\partial}{\partial x_3} \\ \frac{\partial}{\partial x_2} & \frac{\partial}{\partial x_1} & 0 \\ 0 & \frac{\partial}{\partial x_3} & \frac{\partial}{\partial x_2} \\ \frac{\partial}{\partial x_3} & 0 & \frac{\partial}{\partial x_1} \end{bmatrix} \begin{bmatrix} u_1 \\ u_2 \\ u_3 \end{bmatrix} \tag{2.4}$$

where the matrix on the right side of the equation is denoted as differential matrix $\overline{\overline{\mathbf{D}}}$. Furthermore, the linear relation between strains and stresses of a homogeneous isotropic material is

$$\overline{\sigma} = \begin{bmatrix} \frac{E}{1-\nu^2} & \frac{\nu E}{1-\nu^2} & \frac{\nu E}{1-\nu^2} & 0 & 0 & 0 \\ & \frac{\nu E}{1-\nu^2} & \frac{\nu E}{1-\nu^2} & 0 & 0 & 0 \\ & & \frac{\nu E}{1-\nu^2} & 0 & 0 & 0 \\ & sym. & & G & 0 & 0 \\ & & & & G & 0 \\ & & & & & G \end{bmatrix} \begin{bmatrix} \epsilon_1 \\ \epsilon_2 \\ \epsilon_3 \\ \gamma_{12} \\ \gamma_{23} \\ \gamma_{31} \end{bmatrix} \tag{2.5}$$

where the matrix $\overline{\overline{\mathbf{E}}}$ on the right side of the equation contains the linear elastic properties of the material with Young's Modulus E, Poisson's ratio ν, and shear modulus $G = \frac{E}{2 \cdot (1+\nu)}$. With the use of the differential matrix $\overline{\overline{\mathbf{D}}}$ from Equation (2.4), the force equilibrium on a solid body is expressed as

$$\begin{bmatrix} \frac{\partial}{\partial x_1} & 0 & 0 & \frac{\partial}{\partial x_2} & 0 & \frac{\partial}{\partial x_3} \\ 0 & \frac{\partial}{\partial x_2} & 0 & \frac{\partial}{\partial x_1} & \frac{\partial}{\partial x_3} & 0 \\ 0 & 0 & \frac{\partial}{\partial x_3} & 0 & \frac{\partial}{\partial x_2} & \frac{\partial}{\partial x_1} \end{bmatrix} \begin{bmatrix} \sigma_1 \\ \sigma_2 \\ \sigma_3 \\ \tau_{12} \\ \tau_{23} \\ \tau_{31} \end{bmatrix} = \begin{bmatrix} p_1 \\ p_2 \\ p_3 \end{bmatrix} \tag{2.6}$$

with the vector $\overline{p}$ on the right side of the equation containing the load components in three-dimensional space. The force equilibrium from Equation (2.6) can be declared in stiffness matrix form by plugging Equation (2.4) and Equation (2.5)

$$\overline{\overline{\mathbf{k}}}\, \overline{u} = \overline{p} \tag{2.7}$$

where the stiffness matrix $\overline{\overline{\mathbf{k}}} = \overline{\overline{\mathbf{D}}}^T\, \overline{\overline{\mathbf{E}}}\, \overline{\overline{\mathbf{D}}}$.

2.2.2 Finite Element Formulation

As $\overline{\overline{\mathbf{k}}}$ consists of differential equations, an analytical approach for solving the Equation (2.7) in complex geometries is not possible. Therefore, the analytical approach is discretized using variation principles based on an energy method, called Principal of the Virtual Work [35], [27]. According to this principle, the virtual external work is equal to the virtual internal work in a continuum

$$\delta W_{ext} = \delta W_{int} \tag{2.8}$$

The external virtual work is expressed as the work caused by body deformation as a result of concentrated forces, gravitational loads and surface loads

$$\delta W_{ext} = \delta \overline{u}^T\, \overline{F} + \int_V \delta \overline{u}^T\, \overline{p}\, dV + \int_A \delta \overline{u}^T\, \overline{q}\, dA \tag{2.9}$$

while the internal virtual work represents the work done by strains and stresses

$$\delta W_{int} = \int_V \delta\overline{\epsilon}^T \, \overline{\sigma} \, dV = \int_V \delta\overline{u}^T \, \overline{\overline{\mathbf{k}}} \, dV \, \overline{u} \tag{2.10}$$

This approach is approximated by expressing the body deformations with finite nodal displacements $\overline{d}$ and associated shape functions $\overline{\overline{\mathbf{G}}}$

$$\delta\overline{u}^T = \delta\overline{d}^T \, \overline{\overline{\mathbf{G}}}^T \tag{2.11}$$

With this approximation method, the virtual work equilibrium from Equation (2.8), Equation (2.9) and Equation (2.10) is written as

$$\int_V \left(\overline{\overline{\mathbf{D}}} \, \overline{\overline{\mathbf{G}}}\right)^T \, \overline{\overline{\mathbf{E}}} \, \left(\overline{\overline{\mathbf{D}}} \, \overline{\overline{\mathbf{G}}}\right) \, dV \, \overline{d} = \overline{\overline{\mathbf{G}}}^T \, \overline{F} + \int_V \overline{\overline{\mathbf{G}}}^T \, \overline{p} \, dV + \int_A \overline{\overline{\mathbf{G}}}^T \, q \, dA \tag{2.12}$$

where the notation $\delta\overline{d}$ is not written since this expression is valid for every variation [27]. The integral term on the left side of Equation (2.12) represents the element stiffness matrix $\overline{\overline{\mathbf{K}}}$, while the terms on the right side is called the nodal load vector $\overline{f}$. Therefore, this relation is denoted as

$$\overline{\overline{\mathbf{K}}} \, \overline{d} = \overline{f} \tag{2.13}$$

in the general convention of FEA.

Lightweight structures may tend to yield in structural instability when exposed to loads above a certain critical limit f_{crit}. This instability is called buckling. The buckling phenomenon is described as a sudden appearance of bending on the surface as a result of exceeding the critical load in form of compression, shear or combination of both [13]. A comprehensive analytical introduction of buckling instability can be found in [13], where the finite element approach of this problem is described.

In FEA, the buckling problem is solved using eigenvalue calculation [27], [35]

$$\left(\overline{\overline{\mathbf{K}}} - \lambda \, \overline{\overline{\mathbf{K}}}_G\right) \, \overline{d} = \overline{0} \tag{2.14}$$

where $\overline{\overline{\mathbf{K}}}_G$ is the geometrical stiffness matrix and λ is the eigenvalue that represents the ratio between critical load and the current load

$$\lambda = \frac{f_{crit}}{f} \tag{2.15}$$

At this point, the number of eigenvalues (also called as modes) to be computed is determined by the user. The nodal buckle displacements $d_{B,i}$ are obtained in form of eigenvectors on behalf of each requested eigenvalue λ_i

$$\left(\overline{\overline{\mathbf{K}}} - \lambda_i \, \overline{\overline{\mathbf{I}}}\right) \, \overline{d}_{B,i} = \overline{0} \tag{2.16}$$

where $\overline{\overline{\mathbf{I}}}$ is the unit matrix.

In the eigenvalue analysis, the requested eigenvalue of a particular eigenmode is bigger than the previous one. Hence the first eigenvalue indicates the lowest value and gives the sufficient information during stability inspection, whether the structure is buckle-prone.

2.2.3 Solid Shell Elements

The solid quadrilateral element (C3D8I) is an extruded form of S4 shell element from its middle plane in upward and downward directions along its thickness, as shown in Figure 2.7. This element type consists of eight nodes so that `A`, `B`, `C`, and `D` nodes create the top surface, while `E`, `F`, `G`, and `H` nodes create the bottom surface of the element. The solid shell element represents a combination of plane shell element and the Mindlin-Reissner plate element regarding following mechanical characteristics [35]:

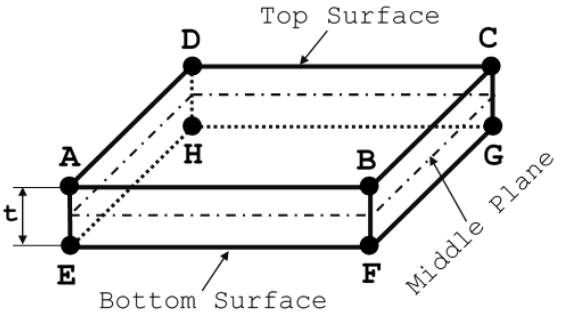

Figure 2.7 *A C3D8I Solid Shell Element*

- The thickness of a shell is much smaller than its two other lengths.
- The thickness remains constant on a shell element.
- Loads and boundaries are placed at the midplane.
- The strain is distributed linearly and symmetric along the thickness direction with respect to the midplane on a shell element.
- At pure bending, strain and stress magnitudes disappear on the midplane.

The solid shell element is formed with 6 DOFs in every node. Therefore the Equation (2.1), Equation (2.2), and Equation (2.3) are applied individually for each node. Furthermore, the shape function matrix $\overline{\overline{\mathbf{G}}}$ from Equation (2.11) are also applied node specific, where these functions are elaborated in [35] and [7]. The numerical integration of the stiffness matrix $\overline{\overline{\mathbf{K}}}$ from Equation (2.12) takes place with 2x2 integration points. A detailed in the integration process is given in [7].

2.3 Common Parametric Aircraft Configuration Schema

Common Parametric Aircraft Configuration Schema (CPACS) is an XML based data exchange format, which has been launched as part of Technology Integration for

the Virtual Aircraft (TIVA) project by German Aerospace Center (DLR). CPACS provides a common language between multidisciplinary analyze methods. Within this concept, a tool is not only able to read the data from different disciplines but also write its results into a single file. Hence, tools from various fields can process the data independently from other tools and share the data with each other, where no further interface is needed. This advantage leads to a faster multidisciplinary communication by reducing the number of necessary interfaces and thus work effort as illustrated in Figure 2.8. With the XML library TiXI and CAD library TiGL, CPACS supports a faster simulation process and geometry manipulations without being dependent to any CAD program, and provides a proper basis for a KBE implementation.

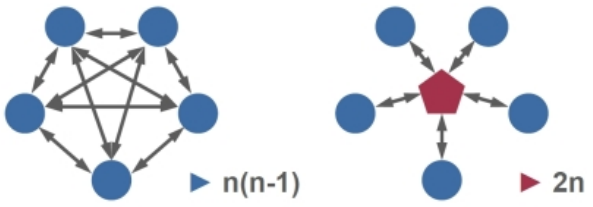

Figure 2.8 *Multidisciplinary Interface Schema of CPACS [40]*

2.3.1 Data Hierarchy

Since the initial release in 2010, CPACS has been developed continuously. An expected upcoming version is v3.0 [18]. Nevertheless, a more stable v2.0 was chosen for SMT development, which is already fully supported by libraries and other simulation tools. In Figure 2.9, a general overview of XML schema [45] is demonstrated in the form of nodes and attributes, in a level range of SMT input needs.

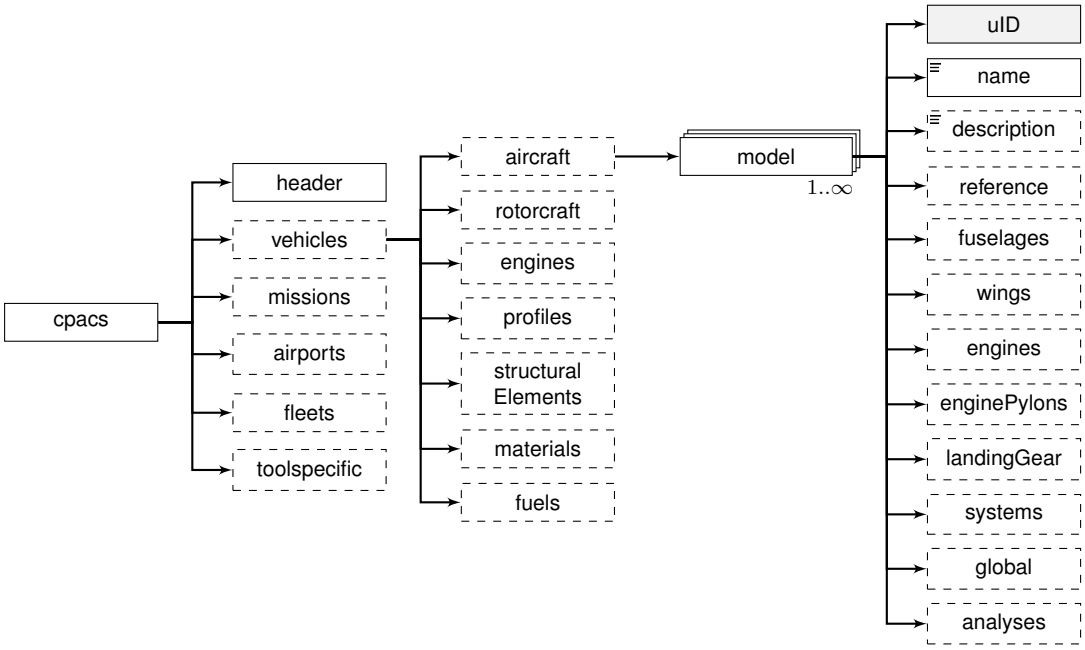

Figure 2.9 *XSD Overview of CPACS Top Level Data Hierarchy*

cpacs is the master node and placed in the first level. The second level contains six top-level nodes in regards to entire transport mechanism data, which are elaborated

in [21] [14]. The user input block from Figure 1.1 is stored entirely in vehicles. In this level, the entire data of the aircraft definition, as well as definitions of commonly used elements, such as profile coordinates, materials, and fuels are stored. Multiple aircraft models can be defined under separate model nodes of aircraft. Each part of the aircraft model is defined under separate nodes in this level. Furthermore, simulation results of an aircraft from different disciplines are stored commonly under analyses.

Navigating through the above-shown data hierarchy is realized using XPath expressions. An XPath expression is generated via combining parent and child elements via placing "/" sign between them. Depending on the desired data type, TiXI than executes the action through the desired function.

2.3.2 Parametric Modeling of the Wing Geometry

A wide range of knowledge-based wing definition is covered in CPACS, which is stored in wings under model in Figure 2.9. With this definition offering a comprehensive parametrization of the wing geometry, the steps of the parametrization process are illustrated in Figure 2.10.

The outer shape of a wing consists of combining the airfoil points consequently in 3D space. For placing the airfoils in the right positions, sections are used. Sections are positioned in translative direction with respect to geometrical properties of the wing, such as length, sweep and dihedral angles. There are two possibilities of section positioning, as they can be placed relative to the global origin (e.g., positioning 1 and positioning 3 in Figure 2.10a) or relative to afore placed sections (e.g., positioning 2 and positioning 4 in Figure 2.10a). A section can contain multiple airfoils in various arrangements. Therefore, each airfoil point cloud is placed on a plane called element that is linked to a section. As Figure 2.10b demonstrates, an element can be translated and rotated on a section plane. The extrusion of the wing surface takes place by linking the airfoils on elements of two sections (see Figure 2.10c). These extrusions are named segments. It is worthy to be noted that one element can be assigned to multiple segments.

Each wing contains internal components, such as structure, control surfaces, fuel tanks and attachments of the lifting surface to the fuselage body. The parametric data of these components are defined within a component segment. Similar to the segments, a component segment consists of the combination of two elements as illustrated in Figure 2.10d. However, the border elements of a component segment can be non-consecutive. Thus, multiple segments can be combined within a particular component segment. In conventional wings, one component segment usually covers all segments of the wing, which represents the entire wing body [26]. In a converse instance, each wing segment can be defined as a component segment. Further wing components, such as winglets, braced struts or other unconventional sub wings are also amongst separate component segments.

A useful localization of the aforementioned internal data of the wing is provided by

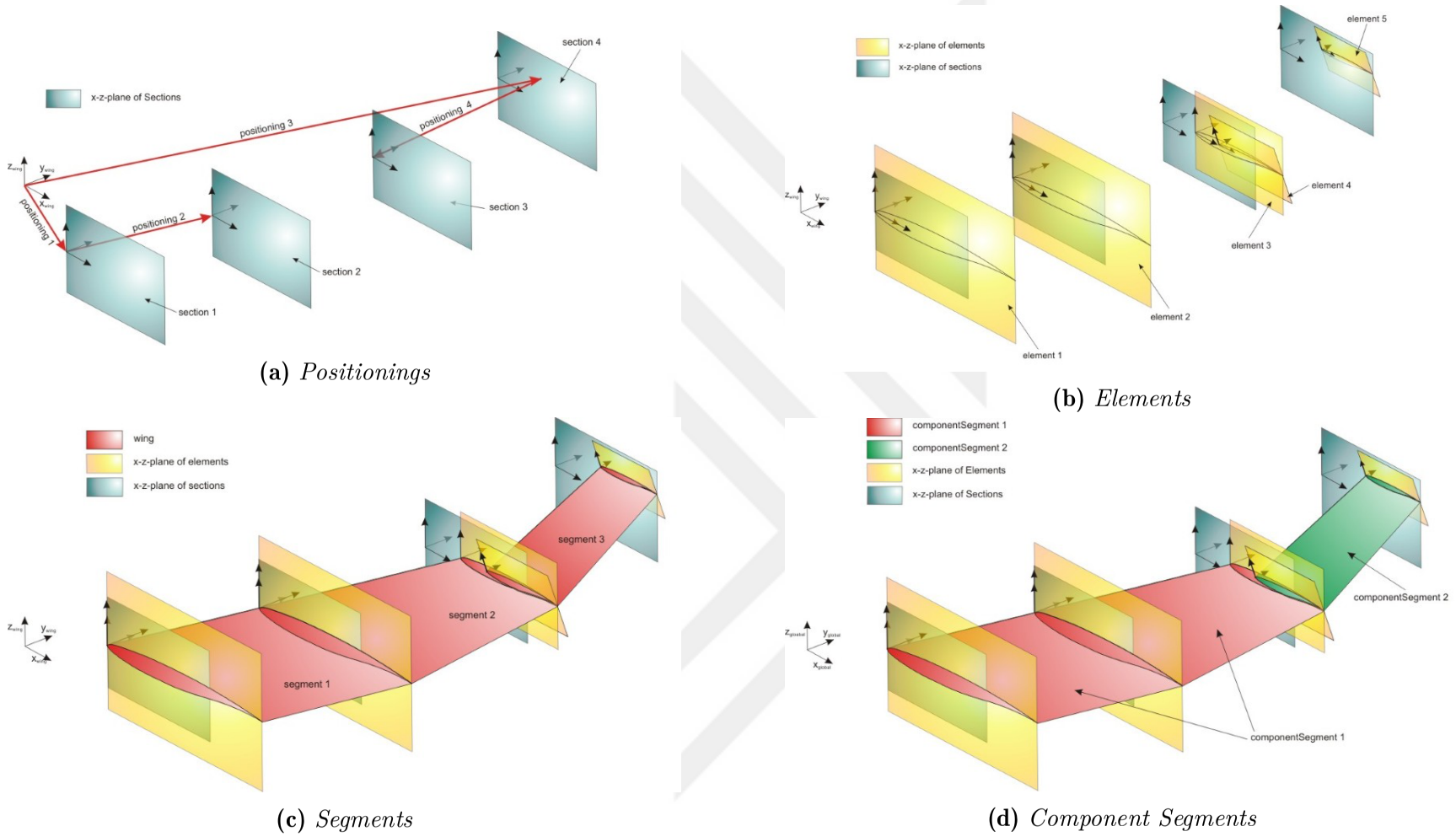

(a) *Positionings*

(b) *Elements*

(c) *Segments*

(d) *Component Segments*

Figure 2.10 *Wing Geometry Parametrization in CPACS [40]*

relative spanwise and relative chordwise coordinates. These coordinates represent the normalized positioning of the wing geometry, hence defined between 0 and 1. A relative spanwise coordinate gives a point the projection line of the wing leading edge on the y-z plane of the wing, while a relative chordwise coordinate refer to a point between wing leading edge and trailing edge at the desired relative spanwise coordinate. In CPACS, relative coordinates are defined for segment and component segments separately. Relative coordinates of a segment denoted as η_S and ξ_S, refer to a position within the segment. $\eta_s = 0$ indicates the root of the segment and $\eta_s = 1$ the tip of the segment, while $\xi_s = 0$ is the leading edge of the segment and $\xi_s = 1$ is the trailing edge of the segment. Relative coordinates of a component segment, denoted as η_{cs} and ξ_{cs}, refer to a position within the component segment with the same principles. If a component segment consists of a single segment, the relative coordinates of segments and component segments lay on another.

2.4 Knowledge-Based Engineering

In a traditional engineering design cycle, most of the development duration is used for repetitive work. Throughout the years, this fact has become a braking element in research and development of the new products. Therefore, a new automated engineering method, named Knowledge-Based Engineering (KBE), has been developed to overcome this problem. KBE is a software-based concept, which enables a product development in a shorter time period compared to classical methods by processing the product and engineering knowledge [19]. The critical aspects of KBE in reducing the time are automation of the repetitive and non-creative tasks, as well as MDO throughout the design process [19]. In the following sections, the methodology of KBE (Section 2.4.1) based on the work of Gianfranco La Rocca [19] and influences of KBE on SMT (Section 2.4.2) are detailed.

2.4.1 An Overview of KBE

In today's technology, knowledge-based solutions take place in computer applications called Knowledge-Based System (KBS) [19]. The development of KBS has roots in Artificial Intelligence (AI) back in the 1970's [19]. The objective of a KBS is to solve problems using primarily stored knowledge of a specific field [19], [10], [6]. KBS is considered in two forms of systems in terms of storing the knowledge: Rule-Based Systems and Frame-Based Systems.

Rule-Based Systems

A rule-based system processes the problem with antecedent-consequent (if-then statement) relation. In the antecedent part, the value of linguistic parameters is controlled by operators. Depending on the boolean result of the control, the appro-

priate procedure is fired in the consequent part. In rule-based systems, the problem is solved with two types of inferences: Forward chaining and backward chaining.

In forward chaining, all rules in the knowledge base are searched and fired, in order to obtain the solution. Forward chaining is fired in the case of rule modifications or adding new facts on to KBS workspace. The search and fire sequence takes place in cycles, where a cycle represents the set of matching rules in the knowledge base. The sequence stops, once all rules are fired. This process can be referred to as the evaluation of an entire scenario in searching for the solution. Therefore, in a KBS with thousands of rules, forward chaining offers an inefficient process in terms of processing time.

In contrast to forward chaining, backward chaining seeks and evaluates the appropriate rule to obtain the solution. In this sequence, rules are evaluated by their consequents ("then" statements), where the data of the corresponding antecedent ("if" statements) is available in the works space. This type of process represents the way of solving the problem through assuming of possible solutions by confirming a hypothesis or suggesting an alternative answer. Since not every rule is to be fired, this process can be considered as more time saving, when compared with forward chaining.

Frame-Based Systems

Frame-based systems provide an environment, where the knowledge, as well as the data, is stored in so-called frame slots, which was initially introduced by Minsky [2], [19]. In today's computational technology, this concept is widely applied through object-oriented programming, where the data is stored in objects by means of classes and methods [19]. An object class is the frame of a domain that holds the parameters and methods, where methods indicate the functions which provides parameter computations that are not directly stored in the class. Object classes can be specified as classes and superclasses [19]. For instance, when an aircraft is considered as a superclass, significant components of the aircraft, such as fuselage, wings, landing gear can form the classes of the aircraft, which hold their parameters and methods.

Object methods are considered in two categories: "When-Needed" and "When-Changed" [19]. "When-Needed" methods return the computed value of in the very moment of the certain value request that is not stored. In "When-Changed" case, methods are executed as soon as the value of a monitored parameter is changed. For instance, changing the thickness of a spar would lead to a change in structural mass and thus the total weight of the wing. In such case, methods would be executed, which computes the new mass of the wing, in order to update the wing volume as a result of the change in thickness. It is worthy to note that both of the mentioned method types are suitable for forward and backward chaining [19].

Frame-based systems also preserve rule-based approaches for solving problems, as the set of rules can be stored in methods. However, it must be taken into account that the entire hierarchical structure of the frame-based system is implicated, in

case of a rule modification in the knowledge base [19].

2.4.2 SMT as a Knowledge-Based Application

Since a structural modeling process takes place in a multidisciplinary conceptual design phase, it is crucial to obtain a useful approximation of a real structure with less effort and time. With these goals, it is striven to eliminate the repetitive and non-creative work done by multiple specialists (aircraft design engineer, structure engineer, FEA specialist, CFD specialist) in the newly developed structural modeling process, where it is given over to an automated KBE concept. Therefore, SMT has been developed as a knowledge-based application.

The KBE concept of this tool focuses on wing as the structural product. Therefore, SMT represents a frame-based system, where wing modeling knowledge is stored in the form of global data structures and functions. In SMT, functions, in which the rules are stored, are grouped according to their types that are classified by La Rocca [19]. These rule groups are logic rules, math rules, geometry handling rules, configuration selection rules and communication rules. The hierarchy of the primary data structure is similar to the wing definition of CPACS. Furthermore, the parametric modeling of the wing geometry in CPACS (see Section 2.3.2), as well as the geometric access capability of the TiGL library (see Section 2.5) offers a good KBS infrastructure for the development of SMT.

SMT was developed on a fixed sequence of processes, in which the involvement of some modeling capabilities are left up to the choice of the user (e.g., including/excluding the fuel loads and aerodynamic loads, see Section 3.3.1). This means that not all functions or rules must be fired during each SMT run. Therefore, the rule implementation on SMT relies on backward chaining, in order to maintain the computational efficiency, by firing only requested rules.

2.5 Softwares

SMT was developed in a multiple software environment. The main code development took place in MATLAB. During model generation, TiXI and TiGL libraries were used for access in CPACS data, while CalculiX was used for FEA during model optimization. This section gives a general overview of these softwares and libraries.

TiXI

TIVA XML Interface (TiXI) is a C library, developed by DLR, which provides effortless access to the aircraft data in CPACS, by enabling tools to read contents from files, as well as to write data into files. Based on libxml2 [36], this Application

Programming Interface (API) is supported by programming languages and analytics platforms such as C, C++, Python, Java and, MATLAB. A comprehensive API documentation for TiXI functions can be found in [44].

TiGL

TIVA Geometry Library (TiGL) is an OpenCASCADE [42] CAD library, developed by DLR using C++ and generates the geometry of CPACS based aircraft model. TiGL offers high flexibility in geometry access such as scanning the wing and fuselage surface in 3D coordinates, computing the areas and volumes, and converting the geometry into diverse CAD formats [14]. Functions and capabilities of this API are documented in [43].

Another feature offered by TiGL is the visualization of aircraft models defined in CPACS format in a 3D environment with TiGLViewer [39]. TiGLViewer not only provides users an instant preview of changes in the model but also enables them to view complex geometries of the wing structure.

CalculiX

CalculiX is an open source module, developed by a team of employees at MTU Aero Engines, which solves field problems using finite element method. CalculiX enables finite element models to be built, calculated and post-processed and runs own solver CrunchiX in linear and non-linear solutions of static, dynamic and thermal problems, where both modules can also be used independently [25]. CrunchiX is able to use input decks that are very identical to Abaqus input format, which makes also use of commercial pre-processors possible. This feature contributes to a dense interaction between SMT and CalculiX during the optimization process.

Although CalculiX was initially designed for Unix platforms, with the bConverged Open Engineering Suite [29], a compatibility of the entire CalculiX content is enabled with MS-Windows platform. Furthermore, additional pre-processing capabilities, a graphical launcher for CalculiX and CAE data translators are also integrated to this concept, where a more user-friendly environment is provided.

LIFTING_LINE

LIFTING_LINE is an aerodynamic tool, developed by Prof. Dr. Karl Heinz Horstmann in 1987, which computes the aerodynamic properties of arbitrary lifting surfaces, such as force coefficients and moment coefficients [4]. The calculation of aerodynamic coefficients take place based on potential theory, where friction and rotation of the fluid are neglected. In LIFTING_LINE, the air flow is considered on profile camber line (Camber Line Theory), which is an idealized form of thin airfoils [4]. The camber line theory is expanded to three-dimensional space, by segmenting

the chord plane into panels in spanwise and chordwise direction, thus keeping the spanwise circulation remained. The computed aerodynamic coefficients are returned with respect to wing reference area and Mean Aerodynamic Chord (MAC), as well as reference area and MAC of the spanwise segmented panels called strips. Furthermore, the computed aerodynamic properties of the strips are delivered on $\frac{1}{4}$ of the wing chord, which is the known as the pressure point of the lifting vortex [4].

Through a tool wrapper, LIFTING_LINE can be used in aerodynamic simulations based on CPACS input files, while simulation results can also be obtained in CPACS format. Hence the aerodynamic loads can be defined in the same input file, where other necessary user input is stored. This feature offers advantages in terms of time-saving.

MATLAB

Matrix Laboratory (MATLAB) is a numerical computing environment that is developed by MathWorks [38] initially for optimizing matrix manipulations. Over the decades, MATLAB became popular simulation tool for many institutes and companies. With its own scripting language, users can implement algorithms, visualize calculations in three dimensions, as well as create GUI's in MATLAB. A wide range of predefined functions and toolboxes offer users a comfortable and efficient developing platform in terms of effort and time. In MATLAB, object-oriented programming is also supported.

SMT development took place in MATLAB mainly by the reasons of the features as mentioned above. Support of TiXI and TiGL libraries for MATLAB has also been vitally beneficial during the development process. Additionally, the feature of MATLAB to control external programs enables SMT to start simulations in CalculiX without any user interaction.

Chapter 3

Model Generation

Model generation is the first of SMT's two process blocks. In this block, a parametric and a finite element model of the wing box is generated based on the input data. The model generation block is involved into structural modeling process in two different phases. First; during initial execution of SMT and second; following to model optimization (more details in Chapter 4). In this regard, the sequence of model generation block consists of four stages, as demonstrated in Figure 3.1. In the first stage, the parametric data of the initial wing structure is generated, regarding introduced wing box elements in the previous chapter. Once the parametric data is created, the finite element geometry of the wing box is modeled in the next stage. This is also the first stage of model generation sequence for the aforementioned modified topology and represents a "When-Changed" method in the KBE frame of SMT. In the third stage, input loads are adapted to the finite element geometry concerning fuel pressure and aerodynamic loads. Based on the finite element geometry of each wing box and the input material, the structural mass is computed in the final stage. Structural mass computation is also executed once the thickness is adjusted in model optimization as a result of "When-Changed" method. It is worthy to note that SMT computes the structural mass for internal mass estimation process, rather than including in FEA as gravitational loads, since CalculiX already computes the structural weight. Following sub-chapters are dedicated to detail the knowledge base of the model generation steps with their rules and capabilities.

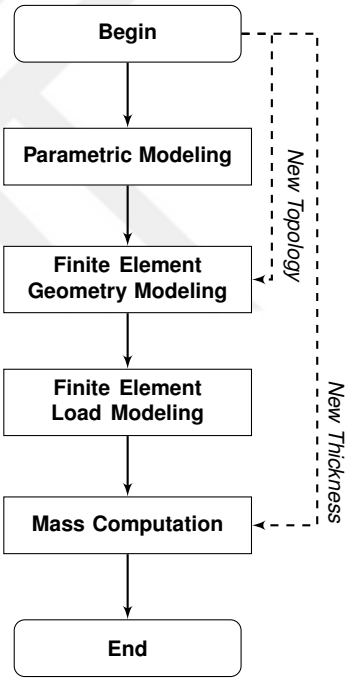

Figure 3.1 *SMT Model Generation Sequence*

3.1 Parametric Modeling of the Wing Box Elements

The parametrization takes place with reference to CPACS' component segment child definitions structure, wingFuselageAttachments, and wingFuelTanks (see Figure A.5 in Appendix). During the modeling process, the wing layout is split into three areas: leading edge, trailing edge, and wing-box area. For a simplified approach, following conditions are considered in the generative process of all wing box elements:

- Wings must consist of segments with linear edges.
- Each wing must contain one component segment.
- No wings must be attached to each other.
- Parametric modeling is concentrated only in wing box area.
- Structural elements with a higher level of detail, such as stringer, stiffeners, rivets, and flanges are not included.
- Surfaces of the structural elements are considered as solid planes, where no hole is not included.
- Connection elements such as wing joints or bolts are also not be modeled.
- The input material must be homogeneous and isotropic.

Under the scope of these requirements, the modeling process takes place through five separate KBE capabilities, which refer to the modeling of spars (Section 3.1.1), ribs (Section 3.1.2), wing covers (Section 3.1.3), wing-fuselage attachment (Section 3.1.4) and fuel tanks (Section 3.1.5) respectively.

3.1.1 Spars

The parametric definition of the spars initially takes place on wing middle plane. The main idea of generating the spar layout relies on drawing lines between consecutive guide points along the wingspan. An example of this idea is illustrated as CPACS concept in Figure 3.2. Spar guiding points are defined as spar positions, where the connecting elements between spar positions are spar segments. Spar positions can be placed at any η_{cs} or ξ_{cs} of the wing, which enables a flexible spar design in wing structure. In this regard, spar segments start or end, likewise cross through wing elements. A detailed definition of spars in CPACS can be found in Figure A.7 in Appendix.

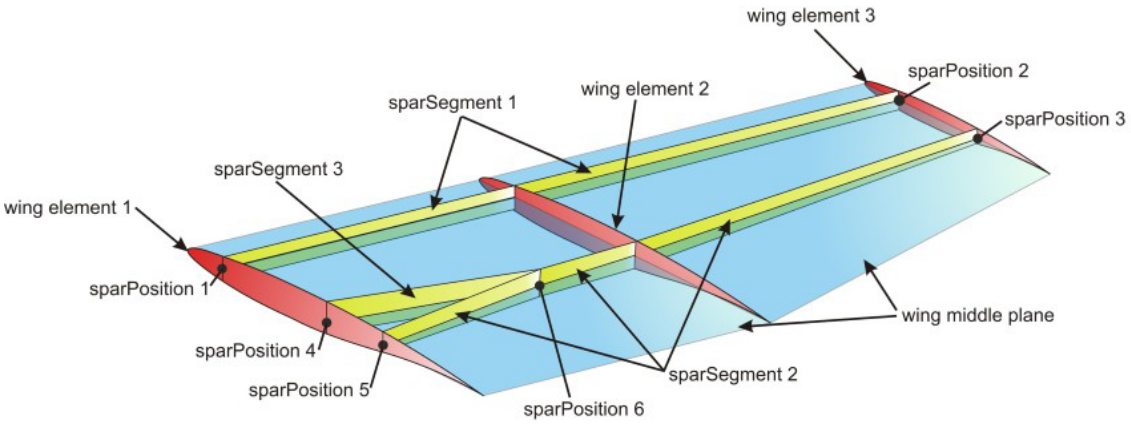

Figure 3.2 *Spar Geometry Parametrization in CPACS [40]*

SMT approaches to the spar modeling process with a simplified method, where the main aim of spars is concentrated on shear stress strength. Therefore, a complex definition throughout the shear web spar concept is avoided, without disrupting the shear strength. In this regard, following KBE rules are considered:

- Front and rear spars are to be generated, as the spar number is held constant at two.
- Spars are stretched from wing root ($\eta_{cs} = 0$) to wing tip ($\eta_{cs} = 1$).
- Spar webs are tailored to the upper and lower skin without spar caps.
- Spars are generated linear through guide points, while no curved spars are included.

In SMT, properties of the spar segments are generated in first place. A UID and a name for each spar segment are assigned, related to parent component segment and spar placement order. As next, imported material from the input file is assigned to spar segment with an initial sizing thickness. During spar segment generation, spar position at the wing root ($\eta_{cs} = 0$) is generated and assigned by its UID.

After the parametric definition of spar segments, spar positions are generated subsequently. For each spar position, a UID is automatically assigned in relation with its component segment, spar segment, and placement order. SMT considers distributing the spar guiding positions on wing segment borders along the spanwise direction. Therefore, $\eta_s = 1$ is converted to η_{cs} for each segment. In typical commercial aircraft, mounting of the landing gear in wing's root segment causes extreme variations on ξ_{cs} of rear spar along the spanwise direction. This issue is not taken into account by SMT so that each spar position is placed at constant ξ_{cs} by the user's preference throughout the whole spar. Once the generation of relative coordinates is completed, the spar position is assigned to corresponding spar segment as well.

3.1.2 Ribs

The parametric modeling of the ribs takes place in sets of one or more ribs, rather than defining each rib individually. Therefore, they are named as rib definitions in CPACS with a broad spectrum of parameterizing options, as they are demonstrated in Figure 3.3. Furthermore, the rib definition parameters, which are generated during this process are shown in Figure A.8 in Appendix.

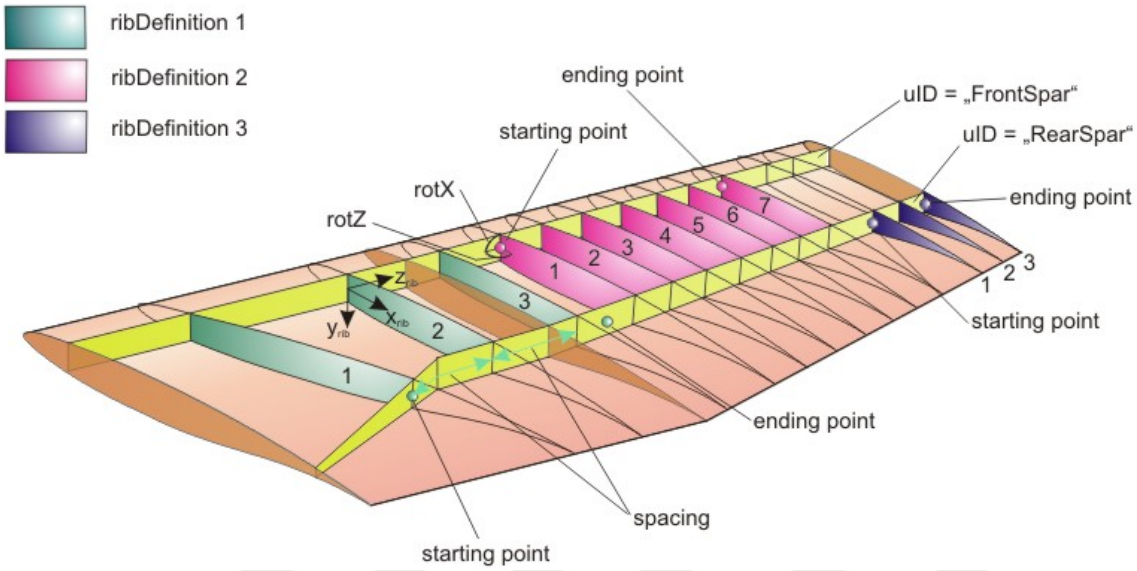

Figure 3.3 *Rib Geometry Parametrization in CPACS [40]*

The range of a rib definition in the spanwise direction is determined using η_{cs}. In this range, ribs can be placed either by a constant spacing length or by the number of ribs, as shown respectively in "ribDefinition 1" and "ribDefinition 2". The ribs can be located inside or outside of the wing-box area. Depending on the reference spar, ribs can be rotated about x or z-axis. Similar to spar modeling, SMT parametrizes ribs on a simple level and adequate conditions to evaluate the structural behavior. In that purpose, it is aimed to have ribs act as buckle stability increasing elements, where a smoother and equal distribution of the air loads between wing covers and spars is enabled. SMT has following KBE rules:

- Ribs are defined as sets, separately in each wing segment.
- Ribs are generated between the front and rear spar.
- Ribs are arranged parallel to the flight path.
- Web of the ribs is tailored to the upper and lower skin without rib caps.

- The spacing between ribs is determined by the number in rib definition, as there's no limitation on the rib number.

During the rib modeling process, SMT defines UID, name, positioning and cross-section properties of rib definitions by order. In purpose of generating rib definitions within each wing segment, the UID and name of the rib definition are generated with relation to wing segment. SMT considers front spar as the reference element for the positioning of the rib. To place a rib definition in a wing segment, spanwise borders of the rib definitions have to be identical with the spanwise positions of the wing sections as well as with the corresponding spar points. Therefore, η_{cs} coordinates of the front spar are directly copied for the determining the rib range. The user determines the initial number of ribs for each rib definition regarding the ratio between the segment width and the half wingspan. During distribution of the ribs, it is striven to set the last rib on the outer border, in order to act as bulkhead due to geometry change. Ribs are aligned parallel to the flight direction, by 90° clockwise rotation around z-axis based on the y-z plane. The cross-section properties are applied to every rib within a rib definition by assigning the standard input material with an initial thickness.

3.1.3 Wing Covers

SMT approaches to parametric modeling of the shells at a fundamental level. In that manner, as an extension of the initial requirements mentioned at the beginning of Section 3.1, one specific KBE rule is considered for the modeling of wing covers:

- Cover skins are modeled as homogeneous surfaces along the wingspan

The modeling process is executed on the parametric base of CPACS shell definition (see Figure A.6 in Appendix). For each part, a UID is generated by SMT, regardless to the component segment, since upper cover and lower cover have no multiple definitions in a component segment. As wing covers do not have specific parameters in terms of giving a geometrical shape to the wing box, the cross-section of each cover is parameterized only by material and thickness.

3.1.4 Wing - Fuselage Attachment

Despite not being a further physical part, the wing-fuselage attachment plays a vital role in wing box model, as this area is to be considered as clamped in FEA. The parametric modeling of the wing-fuselage attachment is made in regards to CPACS definition, of which the hierarchical data structure is demonstrated in Figure A.9

in Appendix. Following KBE rules are considered for the modeling of wing-fuselage attachment:

- Only one wing-fuselage attachment is defined for each lifting surface.
- Attachment borders consist of one rib and the symmetrical plane of the wing.

Compared to the other modeling processes, wing-fuselage attachment is modeled quite simple. Wing-fuselage attachment zone is considered between wing symmetry plane and the last rib of the first rib definition. In this manner, SMT defines the outer rib of the first rib definition as the single border element of the wing-fuselage attachment area.

3.1.5 Fuel Tanks

As the last step of the parametric modeling process, fuel tanks are defined for fuel mass calculations. For this purpose, CPACS offers an adequate hierarchic fuel tank definition for the wings (see Figure A.10 in Appendix). In SMT, fuel tank modeling takes place with following KBE rules:

- Fuel tanks are defined only on first lifting surface in CPACS input
- Fuel tanks are defined in wing box area
- Each rib definition is to be considered as a fuel tank
- Leading and trailing borders are front and rear spar

Similar to previous modeling processes, the UID and name of the fuel tank are defined primarily in relation to component segment and rib definition order. During geometry definition, two spar borders and two rib borders are defined. For the definition of spar border, spar segment UID's of the front and rear spar are automatically copied. Except for the first fuel tank, rib borders of all fuel tanks consist of two rib definitions. The outer rib of each rib definition is considered as an outer fuel tank border, while outer rib of the prior rib definition is considered as inner tank border. Since the fuel tank of the first segment does not share any inner border with a neighbor rib definition, the first rib of the current rib definition is considered as the inner border.

With this parametrization, a more straightforward and user-friendlier approach is realized, rather than a more complex definition with relative spanwise and chordwise coordinates. Furthermore, in case of a change in spar or rib positions, fuel tanks remain defined, so that no further changes are needed.

3.2 Finite Element Modeling of the Wing Box

The structural mesh is the first physical step of preparing the wing box model for FEA. In this step, the geometry that is to be simulated gets separated into segments and meshed as elements afterward. This task is usually taken by an FEA personal. However, during optimization phases, segmentation work in changed topology may cause not only time losses but also improper segmentation. As can be seen in Figure 3.4a, improper segmentations can occur in case of non-continuous edge lines through neighboring segments. It must be ensured that segments up to four edges have one edge with adjacent segments in share (see Figure 3.4b).

(a) *Improper Segmentation* **(b)** *Well Connected Segmentation*

Figure 3.4 *A Comparison Between Correct and Incorrect Segmentations [11]*

An automated concept for mesh segmentation is developed in SMT using KBE techniques. This concept builds up the mesh geometry that consists of spars, ribs and wing covers, in a way that no connectivity errors between mesh segments occur. In order to maintain a proper segmentation, generated spars and ribs are defined as mesh parts (Section 3.2.1), which consist of guide points. Second, mesh segments are created by connecting the adjacent lines in the spanwise and chordwise direction (Section 3.2.2). After this step the topology of wing structure takes shape. Depending on the mesh size, the geometry of ribs, spars, and wing covers is generated separately with nodes and elements (Section 3.2.3). In the final process, adjacent nodes of the mesh parts are connected with each other, and thus the wing structure mesh becomes fully defined (Section 3.2.4).

3.2.1 Parts

Spars and ribs are essential parts in creating the mesh geometry. Therefore, their placement in correct order plays a vital role in the segmentation process. In this phase, borders of each spar segment and rib definition are placed for the preparation of generating mesh segments. SMT first arranges the spar points and derives the rib definition points using η_{cs} and ξ_{cs} coordinates consequently. Based on [19] and [26], following definitions are used during placement of spars and ribs as mesh parts:

Real spars are spars that are generated by SMT with respect to the CPACS definition (see Section 3.1.1).

Virtual spars are not physical spars. They are defined along the leading and trailing edges of the wing, in order to determine a mesh segment border outside the wing box area.

Real ribs are rib definitions that are generated by SMT with respect to the CPACS definition (see Section 3.1.2).

Virtual ribs are ribs, which occur due to the extension of the layout lines from real ribs to leading edge and trailing edge of the wing.

In the phase of placing spar points, SMT first generates the virtual spars as additional mesh parts. Guide points of the virtual spars are placed on the same η_{cs} alignment with segment borders of the wing. As the guide points of spar segments also lay on the segment borders, the number of guide points of a single virtual spar equals to the number of guide points of the spar segments. In the following phase, spar segments are assigned as mesh parts with their spar points in a mesh part array list. Due to a mixed listing in mesh part data, all spars are sorted regarding the ξ_{cs} parameter. According to this, virtual spar on the leading edge ($\xi_{cs} = 0$) takes first place, and virtual spar on the trailing edge ($\xi_{cs} = 1$) takes the last place in the mesh part array list. With sorting the ξ_{cs} coordinates of the spars, each segmented spar border owns a spar guide point in a sorted chordwise order. The placement of sorted spar points is demonstrated in Figure 3.5.

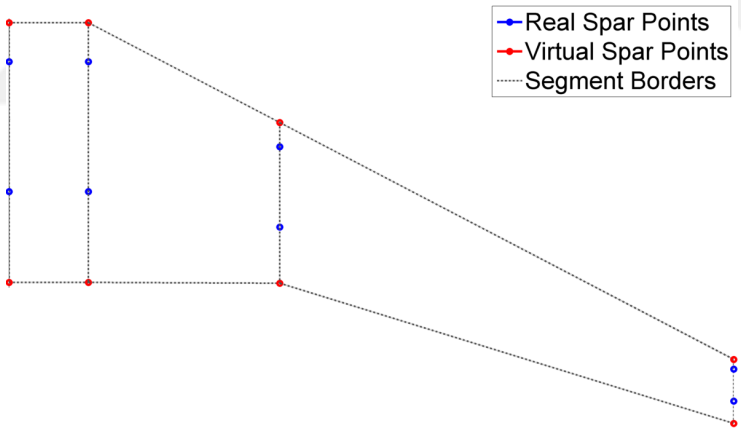

Figure 3.5 *Placed Spar Points for Guiding the Mesh Parts*

Rib points are placed in a similar concept to that of spars, by transferring the ribs directly as mesh parts. At this point, no sorting is needed. SMT places the ribs within the borders of the corresponding rib definition, where the spacing remains constant between all ribs in the same rib definition. Since these borders are derived from spar segment points, they occur between two spar guide points of a spar segment. Although no real ribs are defined in leading or trailing edge area, the borders of real ribs are extended along the chordwise direction up to leading and trailing edge in the purpose of a segmentation as shown in Figure 3.6. After placing both spar and rib points, a grid of mesh points can be obtained. It can be noted that the number of points on each spar and rib alignment is equal. Based on the placed mesh points, the mesh layout is ready to be generated.

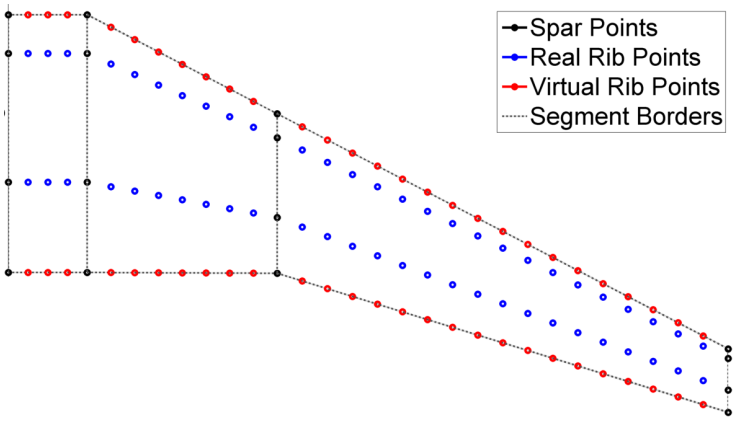

Figure 3.6 *Placed Rib Points for Guiding the Mesh Parts*

3.2.2 Mesh Layout

A mesh layout represents a grid on wing mid-surface area, on the base of which the finite element geometry is generated. The preparation of the mesh layout takes place by merging the points of spar and rib mesh parts that are introduced in Figure 3.5 and Figure 3.6. The merge is made by gathering the relative coordinates on a so-called $\eta - \xi$ table, which contains the relative spanwise and chordwise coordinates of mesh parts in array form. After merging the mentioned coordinates, the layout is generated by drawing straight lines between points of the $\eta - \xi$ table in the spanwise and chordwise directions. During this process, no diagonal lines are generated, in order to prevent a triangular shape occurrence. Figure 3.7 illustrates the mesh layout, where blue points represent the merged points of spar and rib mesh parts. Each quadrant in the layout represents a mesh segment for further mesh geometry. Since each mesh segment consists of four edges, each edge is shared with an adjacent mesh segment, enabling of a well-formed segmentation.

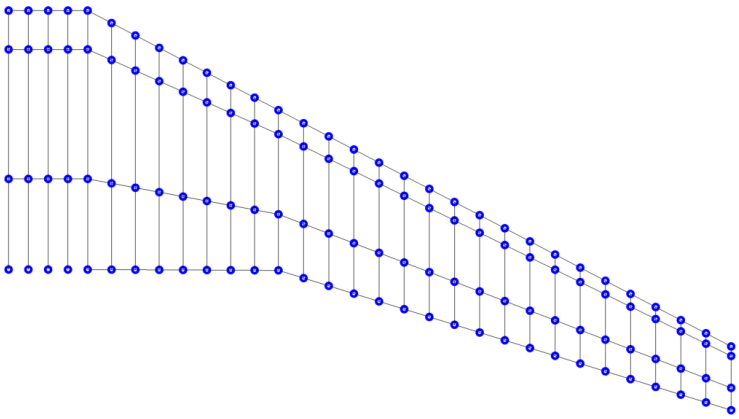

Figure 3.7 *Generation of the Mesh Layout Using Rib and Spar Points*

3.2.3 Geometry

Generating the mesh geometry is the penultimate step of the meshing process. In this step, the geometry of the wing structure is generated utilizing TiGL library. Creating the geometry takes place based on segmented $\eta - \xi$ table from the previous section. This process considers the generation of structure parts separately in following steps:

1. Generate a grid by meshing each mesh segment in further detail on the mesh slayout (see Figure 3.8a),
2. Generate upper and lower skin geometry based on the mesh grid (see Figure 3.8b),
3. Derive spar geometry between upper and lower skin (see Figure 3.8c),
4. Derive rib geometry in wing box area between skins and spars (see Figure 3.8d).

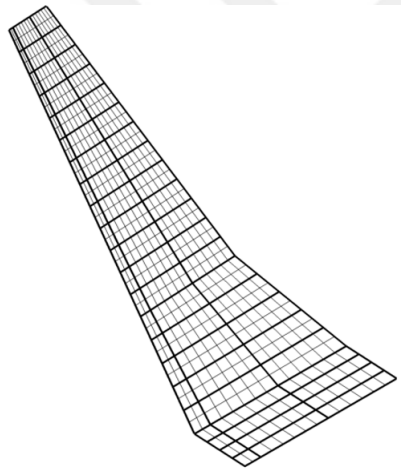

(a) *Mesh Grid*

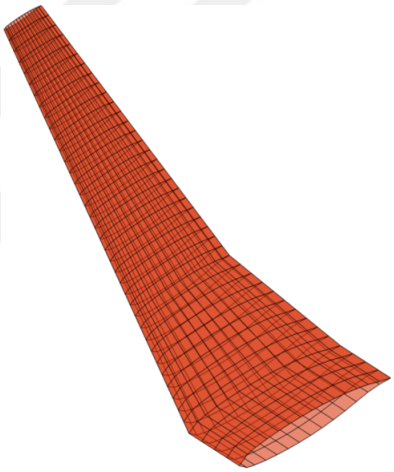

(b) *Skin Meshing*

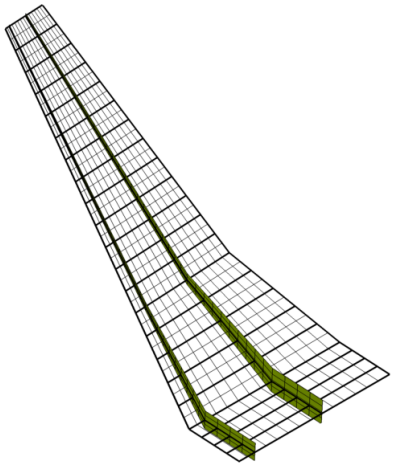

(c) *Spar Meshing*

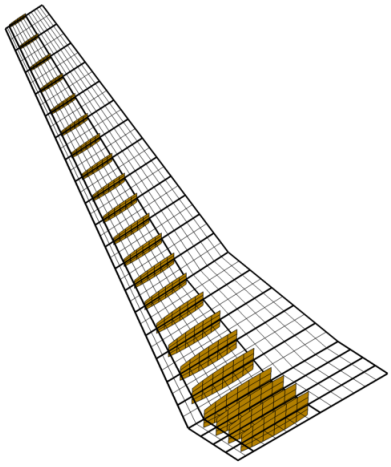

(d) *Rib Meshing*

Figure 3.8 *SMT Mesh Geometry Generation Steps*

Throughout these steps, the geometry data is generated in so-called mesh segments. A mesh segment consists of the upper skin, lower skin, front spar, rear spar, inner rib and outer rib, as illustrated in Figure 3.9. In wing box area, each mesh segment constitutes a closed box with these elements. Mesh segments in the leading edge and trailing edge are bordered with virtual ribs. Therefore they do not represent a closed box.

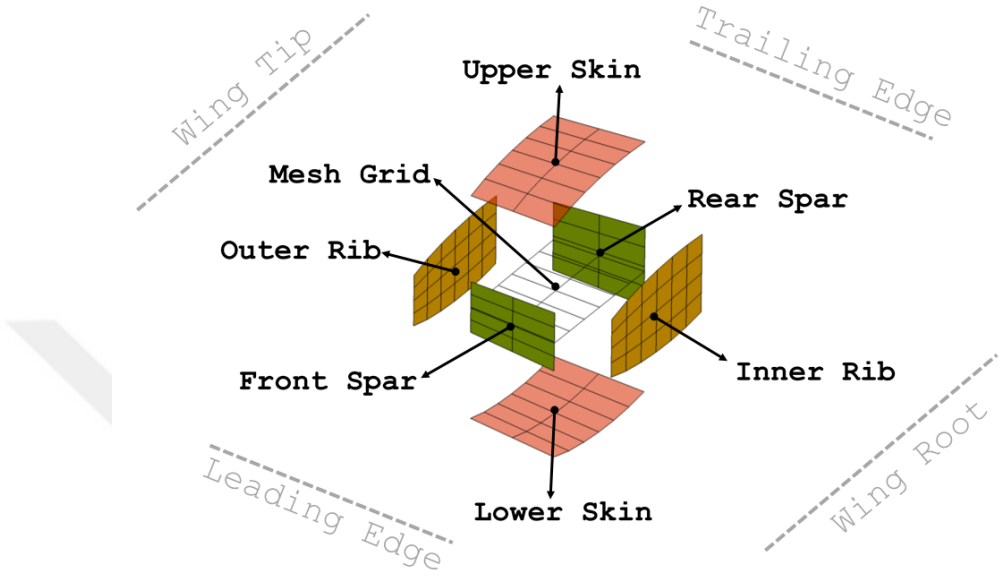

Figure 3.9 *Cutaway View of A Typical Mesh Segment*

SMT processes the mesh segments from leading edge to trailing edge in the chordwise direction. Hence, the rear spar geometry in a mesh segment is taken as front spar geometry by the neighboring segment in the chordwise direction. Since the wing leading edge does not contain any real spars, mesh segments with borders to leading edge do not need a further front spar geometry. This situation also counts for the wing trailing edge. In the spanwise direction, ribs are processed from root to tip, so that the outer rib geometry of a cell counts as inner rib geometry of the next spanwise neighbor.

The geometrical parts of a mesh segment are formed with quadrilateral S4 element type, which is a linear element type with four sides and consists of four nodes. An overview of the required data for nodes and elements is shown in Figure 3.10. Each node is defined with global `X`, `Y`, `Z` coordinates, as well as with a unique `Index`. Similarly, an element has also identified with an `Index`. The corner of each element is indexed with `A`, `B`, `C` and `D`, which contain the `Index` of the corresponding node. Depending on the mesh part, the element nodes are assigned in different order and direction. The reason of this variety is to provide a less complicated assembly sequence which is elaborated in Section 3.2.4.

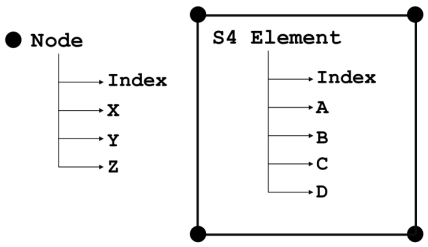

Figure 3.10 *Node and Element Data Structure*

Mesh Grid

The mesh grid is generated through linearly spaced guide points (apart from nodes) with respect to η_{cs} and ξ_{cs} coordinates. The point number is the measure of the element size and are explicitly calculated for each mesh segment. Apart from how long the edges of the mesh segment are, the number of points is controlled by a parameter that describes the desired element length. In this regard, SMT calculates the length of the mesh segment's leading edge. In order to obtain the element number, this length is divided into desired element length. Against a possible decimal result, the resulting number is rolled up to next integer. Adding one to the element number delivers the number of guide points in the spanwise direction. A similar procedure is used for obtaining the number of guide points in the chordwise direction, yet with the mesh segment's inner rib length and desired element length in the chordwise direction. A typical example of a mesh grid is illustrated in Figure 3.8a with thick lines representing the mesh layout, while thin lines represent chordwise and spanwise grid edges. It can be seen that a continuous and proper element distribution throughout the mesh segments in both directions is provided, which is the consequence of a proper segmentation.

Skin Meshing

Skin meshing is the phase of generating upper and lower skin geometry with elements and nodes. During this phase, node clouds of the upper and lower wing geometry are generated separately on the basis of the projected mesh grid. Node clouds are generated using TiGL functions, more precisely tiglWingGetUpperPoint and tiglWingGetLowerPoint [43]. These functions deliver the `X`, `Y` and `Z` coordinates located on the upper or lower surface of the wing at a given η_s and ξ_s. Despite that the mesh grid coordinates are defined in component segment coordinates, TiGL can convert the relative coordinates between segment and component segment as well.

Node assignment on a skin element takes place in the counter-clockwise sense, beginning with the corner close to wing root and leading edge, as shown in Figure 3.11. In this regard, `B` and `C` corners of skin element share the same nodes with `A` and `D` corners of the neighbor element in the chordwise direction. Similarly, `D` and `C` corners of a skin element share the same nodes with `A` and `B` corners of the neighbor element in the spanwise direction.

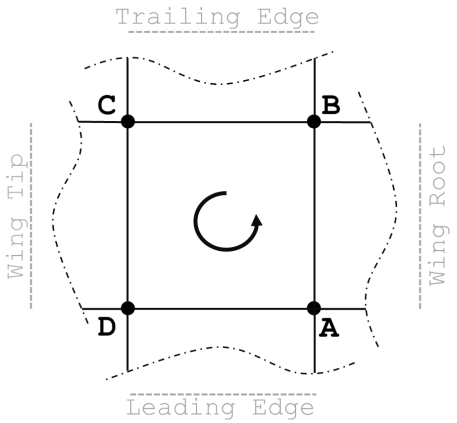

Figure 3.11 *Node Assignment in Skin Element*

Spar Meshing

The nodes of spars are generated with linearly spaced points between the nodes of upper skin and lower skin. In conventional passenger aircraft wings, the thickness of the wing profile drops along the spanwise direction, as the chord length gets shorter due to the taper ratio. This consequence has a direct effect on the distance between the upper and lower point in a particular relative coordinate. Therefore determining the element size by a constant desired element length may cause differences on number of spar web points along the spanwise direction. To prevent this error from happening, SMT sets the number of nodes constant throughout the entire wing structure, without considering the element length. In this manner, generating a rib mesh with quadrilateral elements would also be enabled.

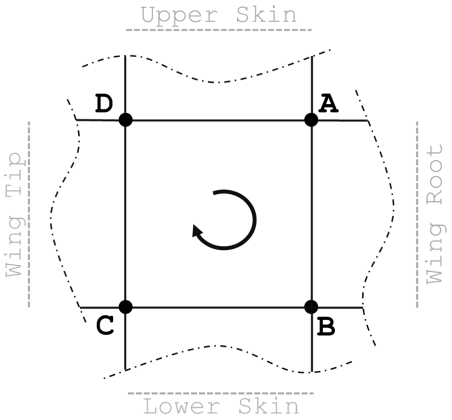

Figure 3.12 *Node Assignment in Spar Element*

Spar elements are generated from upper skin to lower skin in the vertical direction and from root to tip in the spanwise direction. As shown in Figure 3.12, nodes are assigned on a spar element in the clockwise sense, starting from the corner close to upper skin and wing root. According to this assignment, `B` and `C` corners of a spar element share the same nodes with `A` and `D` corners of vertical neighbors. In the spanwise direction, `D` and `C` corners are assigned to the same nodes that are cornering as `A` and `B` nodes of neighbor elements.

Rib Meshing

Since ribs are placed in the wing box area, borders of the mesh nodes are implicitly defined during previous processes. Ribs share their borders with front and rear spar in the chordwise direction, as well as with upper and lower skin along the vertical axis. Therefore rib nodes are generated linearly between these borders. Furthermore, an element size adjustment is also not necessary for this process, since the rib nodes are derived from spar and skin nodes, which are preliminary adjusted.

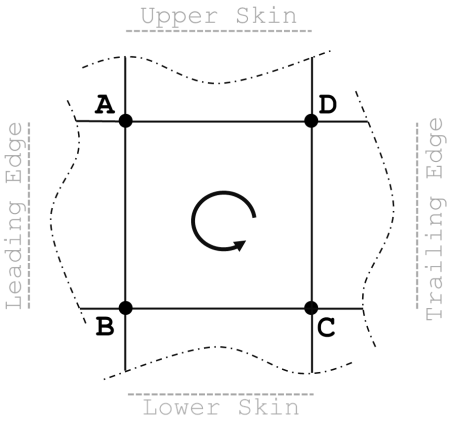

Figure 3.13 *Node Assignment in Rib Element*

Rib elements are defined from leading edge towards trailing edge in the chordwise direction and from upper skin towards lower skin in the vertical direction. Node assignment of a rib element takes place in counter-clockwise starting from the corner on the side of the leading edge and upper skin as shown in Figure 3.13. As a

result of this formation, A and B corners of an element share the same nodes with D and C corners of the neighbor elements in the chordwise direction, while A and D corners share common nodes with B and C corners of neighbor elements in the vertical direction.

3.2.4 Assembly

In the previous section, proper meshing methods for automated finite element geometry generation of the wing box elements were introduced. However, during the geometry generation process, each part was generated partially in mesh segments

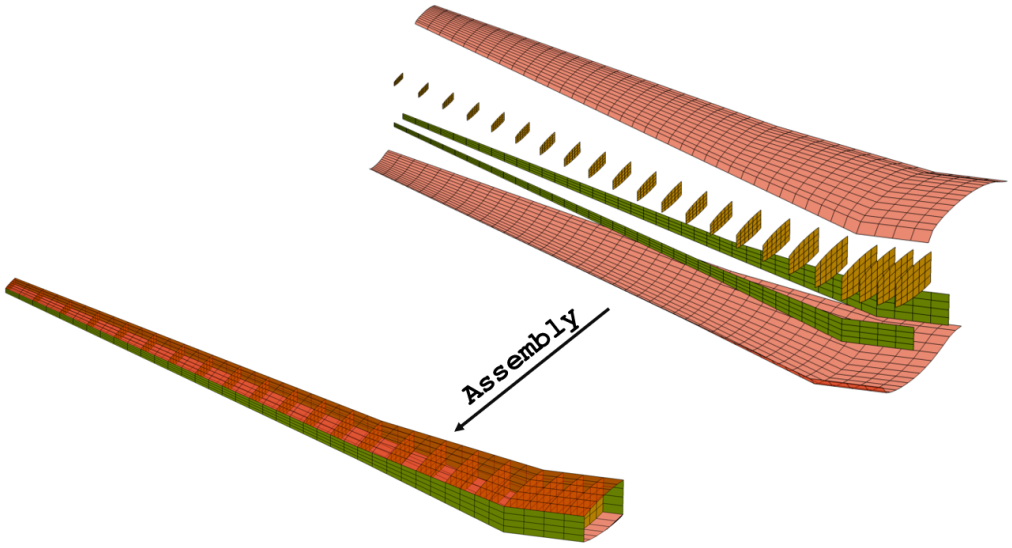

Figure 3.14 *Preparation of the Wing Box Mesh Geometry*

with individual nodes so that each part is independent. In order to have the wing box geometry fully defined, assembly processes for part segments, between parts with common borders are to be executed. Furthermore, as the upper and lower skin in mesh segments outside the wing box area do not represent the structural geometry of the wing box, these parts need to be trimmed as well. The mesh geometry of the wing box model illustrated in Figure 3.14 both in the form of cut-away and assembled. In SMT, the automated assembly process for each mesh geometry takes place by order in skins, spars, and ribs, as they are detailed in following subchapters.

Skin Assembly

The mesh assembly of the upper and lower skin is done with by steps:

1. Trim skin parts of mesh segments located out of wing box zone
2. Attach chordwise elements with elements from previous mesh segments

Trimming the skin takes place in all elements, which belong to mesh segments in front of the front spar and behind the rear spar. In this manner, SMT goes through all mesh segments and identifies, whether the mesh segment is inside the wing box or not. This identification is done by purposely developed KBE rules, which refers to UID of each spar geometry of the current mesh segment. If the front or rear spar UID of a mesh segment preserves a virtual spar set for wing leading edge or trailing edge, that mesh segment is considered as not located within the wing box area. In such case, SMT trims the upper and lower skin of that mesh segment by deleting the corresponding nodes and elements.

In the second step, the inner border of the first skin element in current mesh segment is merged with the outer border of the last element in previous mesh segment along the chordwise direction. This step is applied starting from second mesh segment in the spanwise direction, as both skins in the first mesh segment do not share an inner border with any neighbor mesh segment. To do this, SMT copies `D` and `C` nodes from previous mesh segment into `A` and `B` nodes of the current mesh segment. Corresponding nodes, which are no longer assigned to `D` and `C` are not included in the FEA input file. Therefore their index is set to 0 for being indicated as unused during the writing of the FEA input file.

Spar Assembly

The meshes of the spars are assembled in the following sequence:

1. Attach spar elements to skin nodes
2. Attach adjacent spar elements between mesh segments

Spar elements are attached to the skin surfaces through their borders. Since no spar caps are considered, elements with borders to upper and lower edges of the spar are set in connection with element nodes at the edges of upper and lower skin. On upper edge, `A` and `D` nodes of upper skin elements are copied into `A` and `D` nodes of spar elements along the spanwise direction. On lower edge, `A` and `D` nodes of lower skin elements are copied into `B` and `C` nodes of spar elements along the spanwise direction.

Even though a spar segment is defined from root to tip, its geometry is generated separately along the spanwise mesh segments. In the second step, they are assembled with each other. Due to the same reasons in skin assembly, this step is applied from second the mesh segment in the spanwise direction. During this step, `C` and `D` nodes of outer spar element from previous mesh segment are copied into `A` and `B` nodes of inner spar elements along the vertical axis.

Rib Assembly

Ribs are assembled with the wing box structures in following steps:

1. Attach rib elements to skin nodes

2. Attach edge rib elements to bordering spars nodes

Border elements of ribs share their edges with those of spars and skins. Same in spar connections, attaching rib edges to skins is the first step. As consequence of placing rib geometry to the outer border in mesh segment, last elements of upper and lower skin in the spanwise direction are taken into account. On upper edge, `D` and `C` nodes of upper skin elements are copied into `A` and `D` nodes of bordering rib elements along the chordwise direction, while same nodes on the lower skin are copied into `B` and `C` nodes of bordering rib elements on the lower side.

The second step of rib assemble operation takes place between front and rear spar. Similar in the first step, this operation is realized at the outer spar elements in the spanwise direction. Attachment process on front spar is done with previous mesh segment in the chordwise direction. `D` and `C` nodes of outer elements along the vertical axis are copied respectively to `A` and `B` nodes of the leading elements of the rib. During rear spar attachment, `C` and `D` of the outer spar elements are copied into `D` and `C` nodes of the trailing rib elements.

3.3 Finite Element Modeling of External Loads

SMT processes the structural optimization individually for each load case. During FEA, the number of load items to be analyzed plays a vital role regarding wing structural optimization. Including more physical item to analysis process ensures a higher accuracy in structural strength and more efficiency in structural mass determination. Therefore, SMT considers not only aerodynamic loads but also fuel loads and structural loads in FEA. As structural loads are computed during externally in CalculiX (see Section 4.1), the finite element modeling sequence of aerodynamic loads and fuel loads is shown in Figure 3.15.

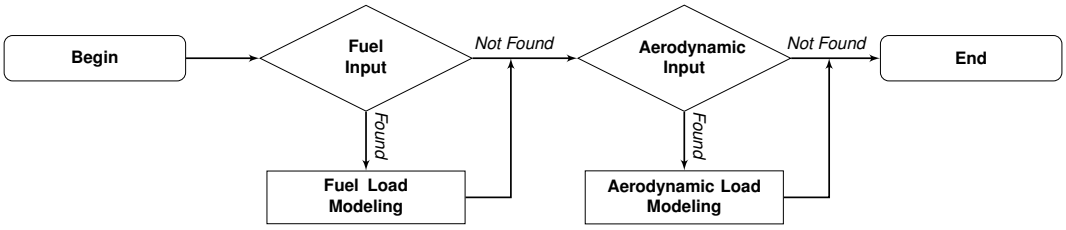

Figure 3.15 *SMT Load Generation Sequence*

In this sequence, fuel load generation process takes the first place, where aerodynamic generation process follows afterward. It must be noted that both processes can be skipped if they are not defined in the internal data set. Thus only structural loads would be involved to FEA. Following sections describe the generation process of fuel and aerodynamic loads in more detail.

3.3.1 Fuel Loads

In structural optimization, the use of fuel mass provides more accurate results. SMT can take this fact into account and models the fuel load in the form of hydrostatic pressure. For the fuel modeling process, the following requirements are considered:

- Depending on the load factor sign, fuel loads are to be applied only on the upper skin or lower skin
- Ribs and spars are not implicated from fuel loads
- All fuel tanks are filled 100%
- The thickness of the structural parts are neglected in the calculation of fuel volume (= optimal volume)
- Elastic deformations on the wing do not affect the distribution of the fuel load

Fuel pressure is calculated separately in each fuel tank within its structural borders. As these borders are already defined during fuel tank generation process (see Section 3.1.5), they have to be identified on mesh segments of the wing. In order to do this, SMT goes through each mesh segment of the wing and compares the mesh segment border UID's with fuel tank border UID's. Mesh segments that are within the borders of a particular fuel tank are considered in the calculation of fuel tank optimal volume. To calculate the optimal volume of the mesh segment, SMT derives column blocks from the mesh geometry between the upper skin and lower skin elements. As shown in Figure 3.16, column blocks contain a quadrilateral cross-section. Nevertheless, they do not represent a quadrilateral rectangular prism due to the sloped orientation of the elements on upper and lower skin. Therefore, the element column volume V_{col} of the corresponding mesh segment is calculated in a separate function with mathematical KBE rules.

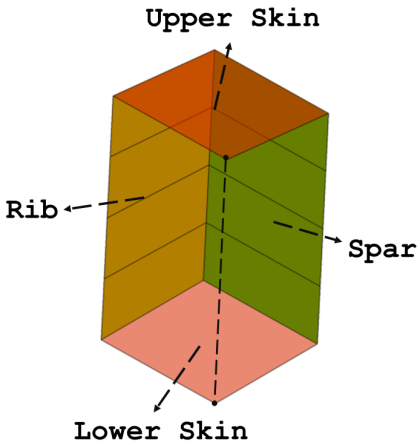

Figure 3.16 *A Fuel Column Block In Mesh Segment*

In the next phase, SMT begins to identify elements to be loaded with fuel pressure by going through all skin elements in the mesh segment. Throughout this action, the index of the elements is registered for FEA input file. Later on, based on the fuel density the mass of the fuel column is derived as follows

$$m_{col} = V_{col} \cdot \rho_{fuel} \tag{3.1}$$

The weight of the fuel acting on the upper or lower surface of the column, based on

m_{col} and load factor n_{LC} of the current load case is calculated as

$$F_{col} = m_{col} \cdot g \cdot n_{LC} \tag{3.2}$$

where the gravitational acceleration is $g = 9,806 m/s^2$. During calculation of the fuel load force in Equation (3.2), the load vector is set in a perpendicular orientation to the earth's surface, since the sloppy normals of the skin elements are assumed as the same. The fuel pressure is derived from the acting load force as follows

$$P_{elem} = \frac{F_{col}}{A_{elem}} \tag{3.3}$$

Depending on the load case, the A_e is derived from the surface area of the upper or lower skin. For $n_{LC} \geq 0$, elements of the lower skin are considered for areal calculation, while upper skin elements are taken into account in case of $n_{LC} < 0$.

3.3.2 Aerodynamic Loads

Throughout the modeling process, aerodynamic loads are not only computed but also distributed on a set of nodes to be prepared for FEA input file correspondingly. As SMT approaches to the generation aerodynamic loads in low level of detail, following requirements and capabilities are considered:

- Aerodynamic loads are computed as static loads
- Aerodynamic loads are calculated on the original wing half
- Only symmetric load cases are computed (no crab angle)
- Due to nodal boundary problems in CalculiX, moment loads are neglected
- Loads applied on the strip reference points are distributed to upper and lower skin surface, that are within the projected strip borders from wing midplane
- Load distribution takes places within the wing box area
- Strip loads that remain within the wing-fuselage attachment zone are distributed to nodes outside of this zone equally

In SMT, aerodynamic loads are generated with respect to the structural hierarchy in CPACS definition that is shown in Figure A.4, where strips are computed within segments under a wing. At this point, the strip numbers are counted independently from the belonging segment, so that the last strip number has the number of total strips assigned to the wing.

Aerodynamic loads are derived as a vector of concentrated forces from aerodynamic

coefficients and reference values individually for each strip, where reference values consist of the strip area and aerodynamic pressure. In this regard, aerodynamic forces applied on the strips are calculated with

$$
\begin{aligned}
F_{strip,1} &= \frac{\rho_{air}}{2} \cdot \left(\frac{Ma}{a_{air}}\right)^2 \cdot A_{strip} \cdot c_{strip,1} \\
F_{strip,2} &= \frac{\rho_{air}}{2} \cdot \left(\frac{Ma}{a_{air}}\right)^2 \cdot A_{strip} \cdot c_{strip,2} \\
F_{strip,3} &= \frac{\rho_{air}}{2} \cdot \left(\frac{Ma}{a_{air}}\right)^2 \cdot A_{strip} \cdot c_{strip,3}
\end{aligned}
\tag{3.4}
$$

In the simulation environment, these load components act on the reference point of the strip, which is located on 1/4 chordwise length and 1/2 spanwise length of the strip. A typical example is shown on single segmented HTP in Figure 3.17a, where red arrows represent the aerodynamic load components placed in red circled reference points within the dashed strip borders. In physical modeling, aerodynamic forces act on the cover of the wing box. For that reason, SMT distributes aerodynamic nodal forces equally to upper and lower skin nodes that are related to the particular strip within the wing box area. Strip borders are concrete measures for defining the nodes on which aerodynamic loads are to be distributed. Since no strip borders are defined in CPACS, they are localized through the strip reference position in η_{cs} coordinates. After localizing the strip borders, SMT detects corresponding mesh segments, which is inside of the wing box area and strip borders on one hand, and outside of wing-fuselage attachment zone on the other hand.In correspondent mesh segments, whole upper skin and lower skin nodes are assigned for the particular strip. Figure 3.17b demonstrates a distribution of concentrated aerodynamic forces on to upper and lower skin nodes, where nodes located in a strip are indicated with the same color.

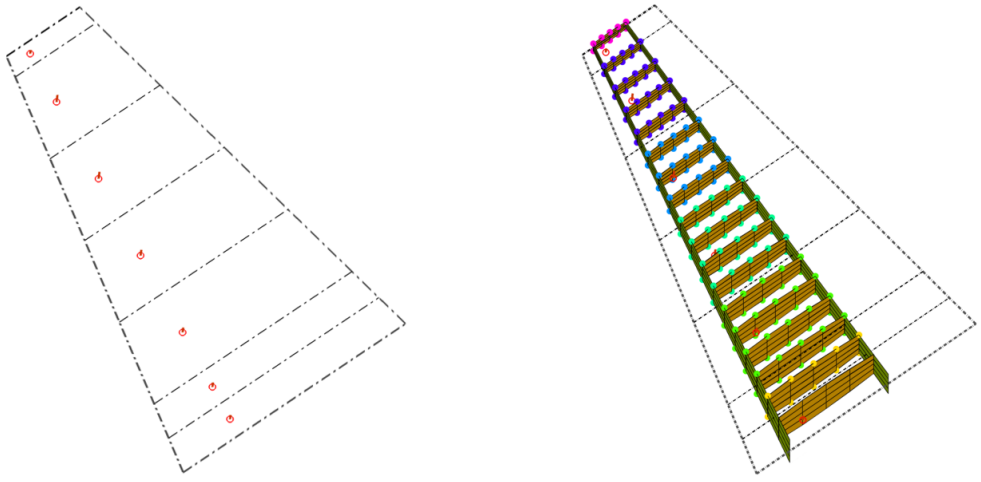

(a) *Aerodynamic Strip Reference Points With Borders*

(b) *Distribution of the Aerodynamic Strip Forces on to Corresponding Nodes*

Figure 3.17 *Modeling of Aerodynamic Loads On a HTP*

Throughout the distribution of aerodynamic loads, three cases occur in terms of assigning the nodes. These cases are demonstrated on a multi-segmented wing in Figure 3.18 and thoroughly described afterward.

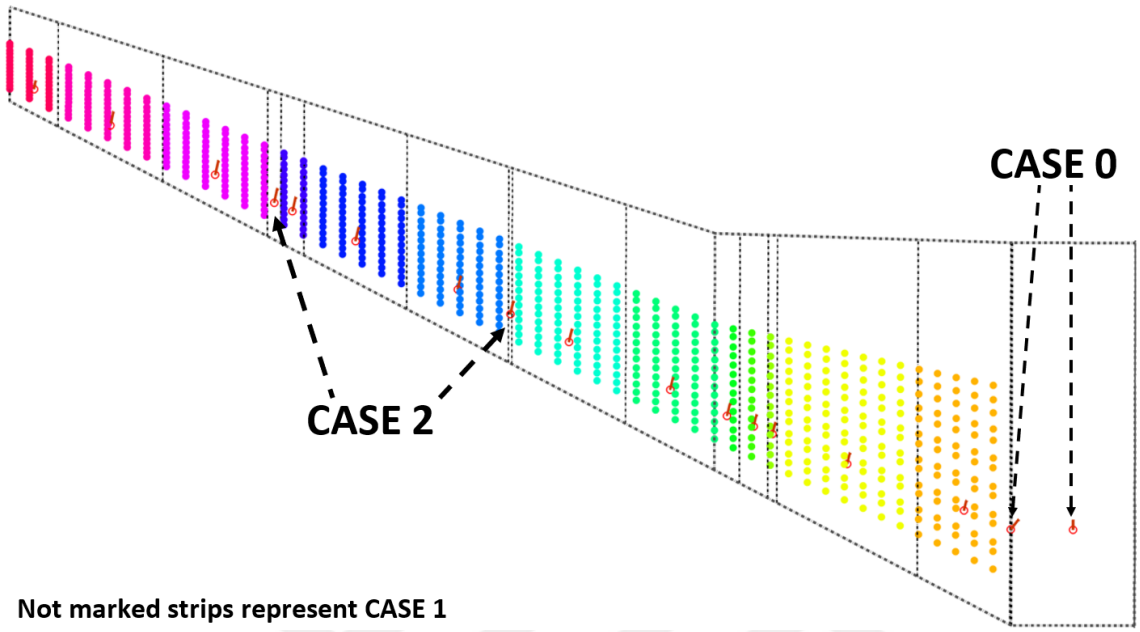

Figure 3.18 *Aerodynamic Load Distribution Cases on a Typical Commercial Aircraft Wing*

CASE 0 occurs in strip borders which are located within the wing-fuselage attachment area. The reason for indicating this case with 0 lies in the fact that only in this case no node is assigned. Instead, corresponding concentrated aerodynamic force vectors are distributed equally to nodes outside of wing-fuselage attachment zone during the preparation of FEA input file.

CASE 1 refers to the standard distribution of aerodynamic loads to corresponding nodes that are located between strip borders, as described above. In Figure 3.18, nodes from these cases are marked in individual colors.

CASE 2 counts for strips that are unable to cover nodes due to their narrowness. In this case, nodes from the spanwise adjacent row are assigned, such that aerodynamic loads from the corresponding strip act outside of the strip borders. Considering that the element sizes are determined in centimeters, postponing of a node row in this small amount of distances can still be accepted, compared to the absolute negligence of the entire load vector of the narrow strip.

3.4 Computation of the Structural Mass

SMT computes the structural mass prior to execution of FEA in model generation. The computation process is executed as a "When-Changed" method, since the struc-

tural mass changes in case of any topology or thickness adjustment. For this process, the following rules are taken into account:

- In symmetric wings, only the wing half is involved in the structural mass computation
- The mass of upper and lower cover is calculated separately
- Rib mass is calculated within their rib definitions, rather than individual

During the computation process, the mass of a structural part is obtained by calculating the mass of generated finite elements in mesh segments. In each mesh segment, the presence of the particular structural part is controlled by its UID. Within the matched structural part, SMT goes through all elements and calculates their elements with

$$m_{elem} = A_{elem} \cdot t_{elem} \cdot \rho_{mat} \tag{3.5}$$

After each calculation, m_{elem} is added to the total mass of the structural part, which is initialized as $0kg$

$$m_{part} = \sum_{i=1}^{N_{elem}} m_{elem,i} \tag{3.6}$$

Furthermore, each structural part mass is added to the mass of the wing structure, which is also initially set to $0kg$

$$m_{struc} = \sum_{i=1}^{N_{part}} m_{part,i} \tag{3.7}$$

Thus the change of mass in each structural part, as well as the entire wing structure can be tracked throughout the optimization processes.

Chapter 4

Model Optimization

The model optimization is executed in a set of stages, regarding the number of load cases. The stages of the model optimization consist of FEA (Section 4.1), structural optimization of the wing box model (Section 4.2) and evaluation of the optimized parts (Section 4.3). The sequence of model optimization with the above-mentioned stages is shown in Figure 4.1.

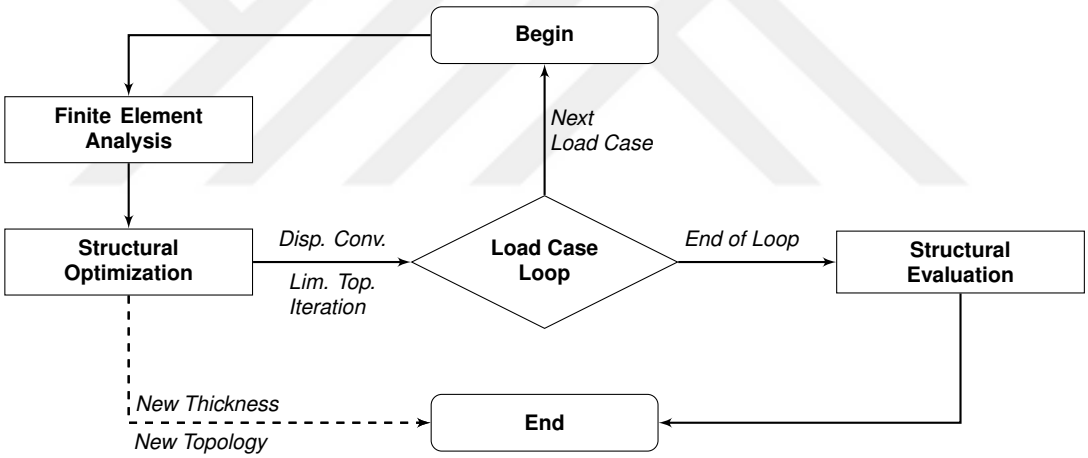

Figure 4.1 *SMT Model Optimization Sequence*

During FEA, the generated wing box model is put through structural simulation externally, and the results are imported back to SMT afterward. Under the scope of keeping the resulting parameters within the limits of stress and stability criteria, the wing box model is optimized through the thickness of the member parts and structural topology. The course of the model optimization sequence is separated into four consequences after the structural optimization, as they are indicated as arrow labels in Figure 4.1. The dashed arrows indicate the flow after an optimization process. *New Thickness* stands for a thickness change on current topology, immediately after which the finite element analysis is executed without changing the finite element geometry. *New Topology* indicates a change in wing box topology within the iterative limits. In case of applying the structural optimization, the sequence of model optimization is partially left, while modeling of the optimized wing box takes

place in model generation block (see Figure 3.1). Once the new adjusted model is computed, model optimization is executed from the beginning. On the other hand, *Displacement Convergence* indicates the ending of the structural optimization by fulfilling the convergence criterion, while *Limit Topology Iteration* is a consequence of reaching the topology iteration limit N_{topol}. After optimizing the wing box model under each load case, an evaluation takes place in wing box elements in order to generate the optimal sized part configuration that fulfills the structural criteria for each load case. The evaluated model represents the output of SMT.

4.1 Finite Element Analysis

A typical FEA consists of pre-processing, processing and post-processing. Regarding this, SMT generates input files for pre-processing based on the generated model and reads back the files resulted from post-processing, while the entire FEA takes place in the chosen tool CalculiX. In the following sections, these processes are shortly described from the aspect of SMT.

Input

Generated geometry and loads are transferred to CalculiX in the form of text files called input deck [24]. For a less complicated input deck, SMT writes the input data in a master input file with four subfiles regarding their functionalities. These functionalities are categorized as mesh geometry, boundary conditions, concentrated loads and distributed loads.

The master input file is the main file that is linked to CalculiX during the execution of FEA. The entire generated input data, such as material properties, section definitions, and output requests are directly written in this file. The input data, which are categorized in subfiles are also linked to this file. In the mesh file, the geometry is written as a group of nodes and elements, as they are generated in SMT. Other than the geometrical data, nodes that are assigned to distributed aerodynamic surface loads are also defined as nodal groups in this file. Boundary conditions file contains prescribed nodes that are considered as clamped in the wing-fuselage attachment zone. All 6 Degree of Freedom (DOF)s of these nodes are blocked by applying single point constraints [24], as they are detected according to rules from Section 3.1.4. In the concentrated loads file, modeled aerodynamic loads are stored as concentrated force vectors. As per rules stated in Section 3.3.2, aerodynamic loads are defined in three translational directions. The distributed loads file contains the fuel pressure loads and structural gravity loads. In this file, fuel loads are explicitly defined as they are modeled by SMT, whereas the computation of structural loads are only stated, such that CalculiX computes them during pre-processing.

Process

Once all input files are generated, SMT executes CalculiX. CalculiX expands all imported two-dimensional S4 elements in three-dimensional C3D8I (see Figure 2.7) elements by adding extra nodes . For each element node, two new extra nodes are defined. These nodes are placed in reference to the element normal with an offset of half element thickness on both sides. Thus the distance between both ends of the new eight-node brick element remains on the value of thickness, that is assigned to the corresponding element set in the input deck. In correspondence with the generated nodes, two new surfaces are generated between offset nodes. These surfaces build up the three-dimensional solid plate element.

Once the structural geometry was rebuilt with solid-shell elements, CalculiX computes the stiffness matrix $\overline{\overline{\mathbf{K}}}$ and vector of static loads $\overline{f}$, which are introduced in Section 2.2.2. Throughout this process, CrunchiX derives the structural load from element mass, based on the acceleration magnitude and vector [24], and applies this load on the element nodes. Then the solver computes the displacement vector $\overline{d}$ of the generated expansion nodes by solving Equation (2.13). Based on the results of the static step, buckling step is executed as an Eigenvalue problem. In this step, initially generated stiffness matrix from the static step is modified into geometric stiffness matrix $\overline{\overline{\mathbf{K}}}_G$ and the nodal buckle displacement vector $\overline{d_B}$ for the first eigenvalue is calculated by solving Equation (2.14) and Equation (2.16).

Output

CalculiX exports result data in '.frd' and '.dat' files. These files contain displacement and stress data from expanded nodes, as well as buckle factor of the structure.

During the optimization process, displacements are used for determining the optimization convergence, and for determining whether the structure is buckle-prone. With consideration of node amount to be processed, importing the displacement in the form of magnitudes, rather than directions would ensure substantial memory savings during the optimization process. Therefore SMT obtains nodal displacement magnitudes for both steps by the following calculation

$$d = \sqrt{d_1 + d_2 + d_3} \tag{4.1}$$

where d_1, d_2, and d_3 are the nodal displacements in respective directions. Stress values are processed regarding the stress criterion developed by Richard von Mises[1], which is widely used for isotropic materials. This criterion enables to analyze the stress tensor as a scalar value as follows

$$\sigma_M = \sqrt{\frac{(\sigma_1 - \sigma_2)^2 + (\sigma_2 - \sigma_3)^2 + (\sigma_3 - \sigma_1)^2 + 6(\tau_{23}^2 + \tau_{31}^2 + \tau_{12}^2)}{2}} \tag{4.2}$$

while σ_1, σ_2 and σ_3 represent the normal stress, and τ_{12}, τ_{23} and τ_{31} represent the shear stress in respective directions.

4.2 Structural Optimization

During model optimization, a wing structure with maximum efficiency is aimed. This can be reached by fulfilling various design constraints at a minimum structural weight. In order to fulfill design constraints, the structure is put to an optimization process. Optimization process consists of three methods: Sizing Optimization, Topology Optimization and Shape Optimization. A good introduction to these methods has been made in [16]. Optimization process offers the most effective results when all three methods are combined. [12] can be referred to as a good example to this.

Since the wing geometry must be kept unchanged, SMT uses sizing and topology optimization in combination. As the sequence of events regarding sizing and topology optimization is demonstrated in the corresponding block of Figure 4.2, these processes are separately described in Section 4.2.1 and Section 4.2.2. This iterative process is inspected by convergence criteria concerning both optimization methods, which are illustrated as decision boxes in Figure 4.2.

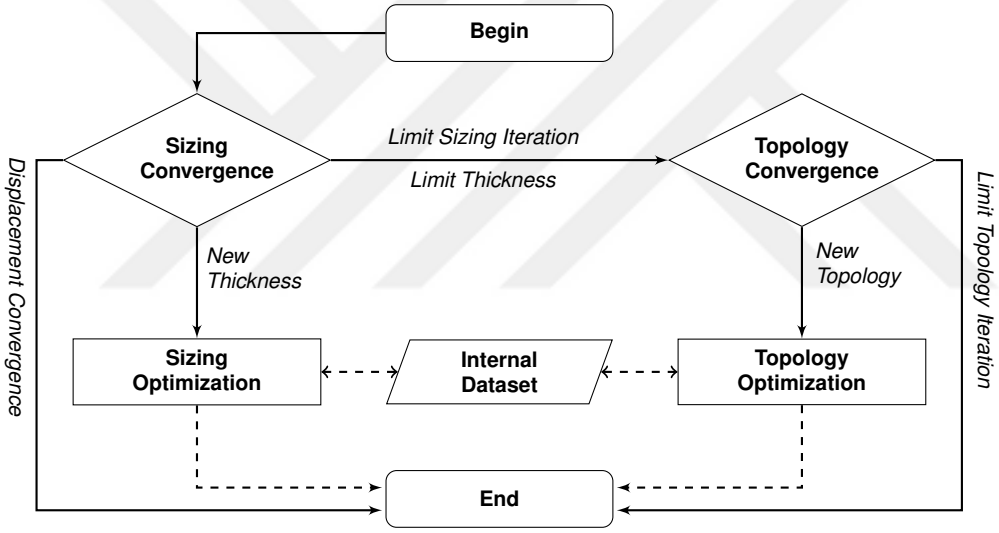

Figure 4.2 *SMT Structural Optimization Sequence*

In this regard, the difference of maximum displacement between two consecutive sizing iterations is compared with a tolerance displacement difference

$$\Delta d_{max} = d_{max,i-1} - d_{max,i} \tag{4.3}$$

where index i represents the sizing iteration number. $\Delta d_{max} > \Delta d_{tol}$ leads to execution of sizing optimization with *New Thickness* result, while $\Delta d_{max} \leq \Delta d_{tol}$ terminates the optimization process with *Displacement Convergence*, where a wing structure is suitable for defined load cases. During sizing optimization, some parts may exceed the upper thickness limit, especially in early iteration steps, for the purpose of meeting the optimization criteria. This case is represented by *Limit Thickness* that leads structural model to a topology optimization. Furthermore, the sizing optimization can be controlled by a maximum allowable number of iterations, in order to prevent

time losses due to slow converging or even diverging simulation results. In case of exceeding this maximum iteration number, sizing optimization is terminated with *Limit Sizing Iteration*, where the structural topology is optimized afterward.

Topology optimization is also inspected against convergence in terms allowed iteration number. If the allowed iteration number is not reached, topology optimization is executed with *New Topology*. In case of reaching the allowed number of iterations, if a displacement convergence in sizing optimization is not the case, the function returns *Limit Topology Iteration* and goes to evaluation process with current structural topology. It must be noted that an approximated structure is evaluated in the latter process, rather than a suitable structure.

4.2.1 Sizing Optimization

The sizing optimization is an iterative optimization method to obtain high efficiency in wing structure, where sheet thickness of the structural part is adjusted iteratively, in order to fulfill sizing criteria. Two types of sizing methods were introduced in [16], which play the major role in sizing optimization process of wing structures. Based on these sizing types, an overview of automated sizing process for the complete aircraft structure was demonstrated in [32].

Sizing optimization is applied through the following equation

$$t_{part,new} = k_{part} \cdot t_{part} \tag{4.4}$$

where t_{part} is the part thickness prior to the adjustment, k_{part} is the optimization factor, and $t_{part,new}$ is the sized part thickness. As can be taken from Equation (4.4), SMT applies sizing optimization on the entire part, rather than applying on critical fields. This method ensures a very safe approach for initial structural optimization process, despite possible weight overestimations.

Throughout the sizing process, SMT inspects each part against stress and stability criteria respectively. During these inspections, further optimization factors $k_{part,\sigma}$, and $k_{part,\lambda}$ are computed regarding stress and stability sizing. The one with the bigger value is assigned as k_{part} afterward. The calculation of stress and stability factors are detailedly described in the following subsections.

Stress Sizing

The stress sizing optimization strives to prevent the structural part from a plastic deformation attitude under a particular loading condition. The stress sizing factor $k_{part,\sigma}$ is calculated as follows

$$k_{part,\sigma} = \frac{\sigma_{M,max}}{\sigma_{yield}} \cdot k_{safe} \tag{4.5}$$

where $\sigma_{M,max}$ is the maximum Mises stress on the part, $\sigma_{mat,yield}$ is the yield strength of the isotropic material, and k_{safe} is the safety factor. At the beginning of the optimization process, $k_{part,\sigma}$ is set to 1, and calculated again during each sizing optimization. Furthermore, the safety factor with $k_{safe} \geq 1$ is set by the user, which relates to the desired safety margin of the adjustment.

Stability Sizing

The stability sizing optimization supports structural strength against buckling occurrence by adjusting the sheet thickness of the critical part. Due to the limitations of analytical stability approach in complex structural geometries, it is suggested in [16] to perform stability sizing process with FEA. For low computational costs and enough satisfactory in analysis accuracy, SMT runs stability sizing optimization based on eigenvalue buckling analysis. Eigenvalue buckling analysis is executed in CalculiX, on the basis of input files generated by SMT (see Section 4.1).

Stability sizing is arranged in two steps. First, the critical eigenvalue λ_{crit} and the corresponding eigenvector are determined in FEA. Then, the thickness of structural parts is adjusted based on the condition of the eigenvalue. The critical eigenvalue is represented by the lowest eigenvalue, while eigenvectors are represented by nodal displacements from the buckle step. Eigenvectors are used for identifying the occurrence of possible buckle-prone elements (also known as buckle fields). As $\lambda_{crit} > 1$ is the mathematical expression of revealing the buckle occurrence in structure model, an element in this structure is considered as buckle-prone, when the displacement magnitude of any member node is equal or greater than an arbitrary minimum threshold displacement $d \geq d_{thr}$. The threshold displacement is a normalized maximum nodal displacement of the structure. The calculation of threshold displacement is

$$d_{thr} = d_{max} \cdot k_{thr} \tag{4.6}$$

where threshold factor k_{thr} is set by the user in $0 < k_{thr} < 1$ interval. At this point, the sensitivity of identifying critical buckle elements can be increased by decreasing k_{thr}.

Similar in stress sizing, the stability sizing factor $k_{part,\lambda}$ makes thickness adjustments of buckle-prone elements. During these adjustments, SMT intends to approximate a target eigenvalue λ_{targ} in the next sizing iteration. Adjustment methods regarding the critical eigenvalue are derived from the analytical approach in [16]. In this regard, sizing factors for each structural part are calculated under three separate conditions for undersized, well-sized and oversized elements. The critical eigenvalue of an undersized structure is located between $0 < \lambda_{crit} < 1$, thus have buckle-prone elements. Those elements are optimized by adjusting their thickness with the following equation

$$k_{part,\lambda} = 1 + \left(\sqrt{\frac{\lambda_{targ}}{\lambda_{crit}}} - 1 \right) \cdot \frac{d_{elem,max}}{d_{max}} \cdot k_{rel} \tag{4.7}$$

This adjustment is impacted by the ratio of maximum nodal displacement of the element to the maximum structural displacement, as well as the relaxation factor, where $0 < k_{rel} \leq 1$. A well sized structure against buckling has its critical eigenvalue between $1 \leq \lambda_{crit} \leq 1.02$ and does not require any further optimization. Therefore, $k_{part,\lambda}$ remains 1 for the entire structure. For an oversized structure against buckling possesses a critical eigenvalue with $1.02 < \lambda_{crit}$. Although this structure would not be questioned about buckling occurrence, the excess amount of part thickness may increase the structural mass. Therefore, a downsizing adjustment is applied with the following equation

$$k_{part,\lambda} = 1 + \left(\sqrt{\frac{\lambda_{targ}}{\lambda_{crit}}} - 1 \right) \cdot k_{rel} \tag{4.8}$$

4.2.2 Topology Optimization

Throughout the sizing optimization process of a particular wing model, convergence limits may be reached before the displacement convergence is ensured due to insufficient structural strength. In a perceptible modeling process, this issue occurs when current structure topology does not fulfill the structural stability requirement despite iteratively increased part thicknesses. In order to overcome this problem, topology optimization is applied.

Topology optimization method contributes to the wing box's structural strength by adding or removing, as well as changing the shape of the structural parts, where the outer shape of the wing box is retained. A typical structural modeling approach based on topology optimization is presented in [28].

SMT applies topology optimization in case of not meeting the absolute displacement convergence during sizing optimization. The objective of topology optimization is to identify buckle-prone elements on the skin surface and modify the corresponding field by increasing the intensity of rib distribution. At this point, ribs act as supporting members against compression on structural surfaces. Thus possible structural instabilities can be prevented from occurring or can be postponed to a higher amount of load. In this regard, topology optimization takes place in SMT with the following requirements:

- Buckle-prone fields are identified only on upper and lower skins
- Structural topology is optimized by changing rib number in critical rib definitions
- Spar topology is retained

In each rib definition with buckle-prone elements, the number of ribs is increased by 1. Hence, the number of added ribs is depended on the number of critical rib

definitions within a topology iteration. A typical iteration sequence of topology optimization is demonstrated in Figure 4.3. As mentioned in Section 3.1.2, each rib definition is equipped with an intended minimum number of ribs in the first topology. Assuming that sizing optimization sequence does not provide a stable structure within limits, topology optimization is applied, based on the finite element buckling analysis. This process is iterated until a displacement convergence, or an iteration limit is reached.

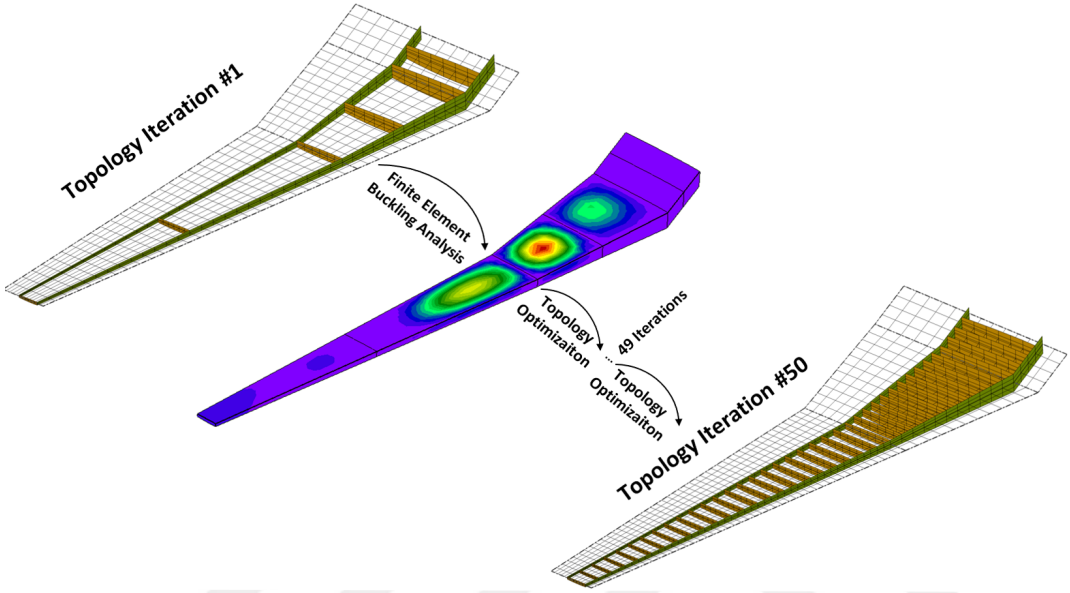

Figure 4.3 *Iterative Process of the Topology Optimization Regarding Buckle Fields*

Topology optimization has effects on the rib positioning and spacing, due to change of rib number in a particular rib definition, which leads to change in mesh size and the total number of elements in finite element model. This situation can be observed at the outer wing segment of "Topology Iteration #50" in Figure 4.3, as the segment topology is meshed more densely in comparison to that of "Topology Iteration #1". It must be noted that the increase of elements related to rib number may cause more extended computational periods in FEA.

4.3 Evaluation of Optimal Structure

Once the structure topology was adapted in each load case, multiple structural models are obtained, which fulfill the criteria under belonging load cases. Despite having the same topology, these structures may vary in terms of thicknesses of the same part between structural models. Therefore, in order to obtain a single structural model satisfying the modeling criteria for each load case, generated topologies are evaluated. During the evaluation process, SMT goes through the structure by its parts. In each part, thicknesses as result of load simulations are compared. For this purpose, the thickness, as well as the structural mass are initially set to $0mm$. At

the end of the comparison, the biggest value is considered as the satisfying thickness. Since the part mass is already determined, the mass of the part is also copied with the thickness and thus a new calculation of the part mass is not necessary. Once the biggest thickness of the part was established, the corresponding data in the internal dataset are updated, and the new structural mass is recalculated by adding the part masses. At this point, the new mass of the wing box structure may result in a higher amount than load case specifically generated structures.

Chapter 5

Application

SMT capabilities were tested by performing a structural topology modeling process. This process was tested on the wing geometry of CSR-01, which is introduced in Section 5.1. Section 5.2 describes the set-up of the modeling process with all kinds of parametric aspects. The results of the application are discussed in Section 5.3.

5.1 Reference Aircraft: CSR-01

CSR-01 is a conceptual short-range aircraft model with two engined conventional wing configuration and denoted as the first aircraft model developed under the scope of CeRAS program [30]. The aircraft is designed to carry 150 PAX in two class configuration to a range of 2500 NM. General specifications of CSR-01 are listed in Table 5.1, while a 3D view is shown in Figure 5.1.

Parameter	**Value**	**Unit**
Range	2500	NM
Passenger Capacity	150	PAX
Payload	$17,0$	t
Cruise Mach Number	$0,78$	$-$
MTOW	$77,0$	t
Wing Area	122.4	m^2
Wing Span	34.1	m
MAC	34.1	m

Table 5.1 *CSR-01 Specifications [30]*

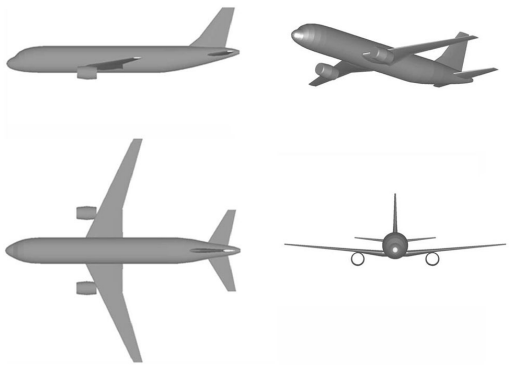

Figure 5.1 *3D View of CSR-01 [30]*

Design characteristics of CSR-01 such as engine performance, aerodynamics, mass breakdowns, aircraft systems and cost aerodynamics are presented in [30]. Furthermore, the entire dataset of CSR-01, as well as used methodologies, definitions and

explanations are serviced to the research community on CeRAS homepage [46].

5.2 Set-Up

The set-up sequence took place in three parameter groups. In the first place, structural parameters were determined in terms of spar and rib positionings, as well as material type and thickness. Second, an identical flight condition with regards to design mission was selected, and the input loads were calculated. Third, control parameters of the modeling process were set. These steps are elaborately described in the following subsections.

5.2.1 Structural Parameters

Spars were generated closely to those of CSR-01. Table 5.2 shows the positions of generated spar segments, while Figure 5.2 demonstrates a comparison between the reference spar layout and generated spar layout.

	Position 1		**Position 2**		**Position 3**		**Position 4**	
Spar Segment	η_{cs}	ξ_{cs}	η_{cs}	ξ_{cs}	η_{cs}	ξ_{cs}	η_{cs}	ξ_{cs}
Spar 1	0,0	0,105	0,117	0,105	0,374	0,105	1,0	0,105
Spar 2	0,0	0,550	0,117	0,550	0,374	0,550	1,0	0,550

Table 5.2 *Spar Positioning Parameters of the CSR-01 Wing In Relative Coordinates*

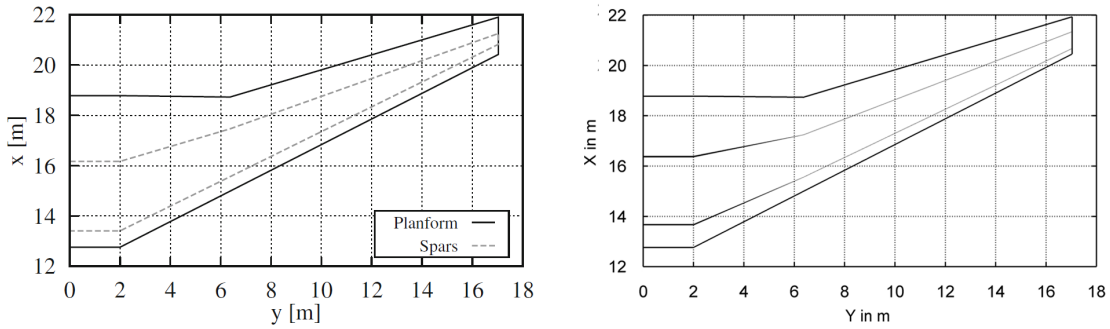

(a) *Reference Spar Layout [30]* **(b)** *Generated Spar Layout*

Figure 5.2 *Spar Positioning Comparison Between the CSR-01 Reference Planform and the Generated Planform*

In the root segment, both wing planforms have identical spar topology. In the kink segment of the reference model, front spar ξ shifts linearly from 0.105 to 0.25 in order to keep the distance between leading edge and front spar constant along the wingspan, whereas rear spar ξ shifts from 0.55 to 0.4 along the wingspan. This

condition leads to a slight deviation between both layouts, which was neglectable.

Since no data for the rib placement from the reference aircraft was accessible, first rib definitions were generated accordingly to Section 3.1.2. During this process, a very low geometrical stability strength was aimed. In this regard, the significant parameters of the initial rib structure are listed in Table 5.3.

	η_{cs}		
Rib Definition	**Start**	**End**	**Rib Quantity**
Rib Def. 1	0,0	0,117	4
Rib Def. 2	0,117	0,374	2
Rib Def. 3	0,374	1,0	2

Table 5.3 *Rib Positioning Parameters of the CSR-01 Wing*

It can be noticed that the borders of each rib definition share the same η coordinates of the corresponding wing segment. Each rib definition was modeled with minimum allowable rib number for the broadest optimization range except "Rib Def. 1". This rib definition is located in the wing-fuselage attachment area, thus defined as clamped in the finite element model, where no structural stress would be expected. In order to maintain a feasible mass estimation, four ribs were assigned in this area based on the examples of wing topologies shown in [5].

During the initial modeling, the thickness of each part was set to $1mm$ with Aluminum 2024 alloy, which is a well-established metal alloy with high usability in the aerospace industry and provides a good compromise between elasticity and strength. The mechanical material features to be involved in structural modeling process are listed in Table 5.4.

Parameter	**Value**	**Unit**
ρ_{mat}	2780	kg/m^3
E	$73,1 \cdot 10^9$	Pa
G	$28 \cdot 10^9$	Pa
σ_{yield}	$324 \cdot 10^6$	Pa

Table 5.4 *Used Material Properties of Aluminum-2024 [47]*

5.2.2 Load Parameters

The load condition is applied on the wing box, based on the design mission of CSR-01[30], which refers to a 2500 NM flight at an initial altitude of 33000 ft, climbing to 35000ft afterward, and with a constant speed of $Ma = 0,78$. The aircraft shall depart from sea level with MTOW, where ISA conditions count throughout the mission.

The wing box model is tested with regards to airworthiness code of EASA CS-25 [7], to validate the structural strength of the wing box model within the airworthiness

limits. CS 25.301 states that the strength requirements of the aircraft structure are described concerning maximum loads, expected to occur during service [9]. In CS 25.255, maximum loads are specified in terms of load factors for maneuvering stability and controllability in the nose up and nose down directions [9]. The aircraft must ensure the structural satisfactory during a pitch maneuver in a vertical acceleration range between -1g to 2,5g [9].

Fuel Loads

In design mission, CSR-01 is loaded with a block fuel amount of 18183 kg and burns respectively 276 kg for taxi and 1932.8 kg for reaching Initial Cruising Altitude (ICA) [30], [46]. Considering the wing box of the entire wing as a fuel tank, the fuel amount to be carried in a wing half at ICA is calculated as follows

$$m_{fuel,ica} = \frac{m_{bf} - m_{txf} - m_{climb}}{2} = 7987,1kg \tag{5.1}$$

At this point, a discussion to fuel tank capacity of the wing must be dedicated. Since the volume of the ribs and spars are not considered during the computation of tank volume, computed volume capacity may seem beyond realistic. An overview of fuel tank capacity generated by SMT is given in Table 5.5, with the fuel mass was calculated using JET A[1], where $\rho_{fuel} = 775\frac{kg}{m^3}$ [47].

Fuel Tank	**Volume in l**	**Fuel Mass in kg**	**Adj. Fuel Mass in kg**
Seg. 1 Fuel Tank	7034	5909	2998.7
Seg. 2 Fuel Tank	7470	6275	3184.5
Seg. 3 Fuel Tank	4231	3554	1803.7
Total	18736	15739	7987.1

Table 5.5 *Generated Wing Fuel Tank Capacity of CSR-01*

With a tank volume of 18736 l in a wing half, the capacity of generated fuel tank is not only larger than the reference CSR-01 fuel tank capacity, but also larger than aircraft with more extended ranges like A321LR[2]. Since all fuel tanks were modeled as fully loaded in FEA, a possible overestimated sized thickness during optimization process poses a structural problem regarding the fuel weight. This problem was solved by manipulating the fuel density in the input file so that the total fuel mass was adjusted to m_{fuel} in Equation (5.1). The manipulation of the fuel density was calculated as follows

$$k_{fuel} = \frac{m_{fuel,ica}}{m_{fuel}} = 0,5075 \tag{5.2}$$

[1] Conditions at 15°C

[2] Range: $4000nm$, Total Fuel Capacity: $32940l$ [41]

$$\rho_{Fuel,new} = k_{fuel} \cdot \rho_{fuel} = 426,28 \frac{kg}{m^3} \tag{5.3}$$

Adjusted fuel masses as result of Equation (5.2) and Equation (5.3) are listed in Table 5.5 both in individual tanks and in total, where the total adjusted mass equals to m_{fuel} from Equation (5.1).

Aerodynamic Loads

Aerodynamic load coefficients were generated using DLR's LIFTING_LINE [4] based on the target lift coefficients of the aircraft and imported to SMT afterward. The imported load coefficients were converted into aerodynamic forces with air data listed in Table 5.6. Target lift coefficients were derived from 1g flight condition to -1g and 2,5g limits.

Parameter	Value	Unit
T_{air}	$222,8$	K
a_{air}	$299,2$	m/s
P_{air}	$2,62 \cdot 10^4$	Pa
ρ_{air}	$0,41$	kg/m^3

Table 5.6 *Air Data at ICA*

In order to obtain the lift coefficient at 1g, the total mass of the aircraft at ICA was recalculated as follows

$$m_{ica} = MTOW - m_{climb} = 75100kg \tag{5.4}$$

With the recalculated mass, the 1g lift coefficient is

$$c_L = \frac{2 \cdot m_{ICA} \cdot 9,806\,[m/s^2] \cdot a_{air}^2}{\rho_{air} \cdot Ma^2 \cdot A_{wing}} = 0,54 \tag{5.5}$$

Deriving the target lift coefficients took place by multiplication of c_L with the limit factors as follows

$$c_{L,1} = -1 \cdot c_L = -0,54 \tag{5.6}$$

$$c_{L,2} = 2,5 \cdot c_L = 1,35 \tag{5.7}$$

5.2.3 Control Parameters

Control parameters are parameters, used for designating the course of the optimization process. These parameters are structured as iteration parameters and optimization parameters. Depending on the aircraft, load case and optimization type, the user can adjust these parameters. In this regard, the control parameters of the current example are listed in Table 5.7.

Optimization parameters contain the factors that are used in the sizing process. The selection of k_{safe} and k_{rel} are based on previous applications, while k_{thr} and λ_{targ} are referred to [16]. Iteration parameters contain the limit values, according to which the iteration process is executed. Previous simulations proved that the lowest

Parameter	Value	Unit
k_{safe}	$1,3$	–
k_{rel}	$0,9$	–
k_{thr}	$0,1$	–
λ_{targ}	$1,01$	–

(a) *Optimization Parameters*

Parameter	Value	Unit
Δd_{max}	5	mm
N_{size}	10	–
N_{topol}	30	–
$t_{part,max}$	15	mm

(b) *Iteration Parameters*

Table 5.7 *Control Parameters of SMT During Application*

eigenvalue sufficiently converges to λ_{targ}, below a maximum displacement difference of $\Delta d_{max} < 5mm$. Furthermore, the displacement convergence was expected to be reached within ten sizing iterations [22]. Since the maximum allowed topology iteration limit correlates with the number of ribs to be added in total, the selected limit covers the entire rib range of aircraft similar MTOW. The maximum allowable part thickness was set slightly lower than similar cases, due to lack of some secondary loads in the generated finite element model. Nevertheless, this limit can be taken as plausible up to $25mm$ with fully modeling geometry [32].

5.3 Discussion of Results

Structural modeling process converged in 12 topology iterations by reaching a displacement convergence in every topology iteration with all parts sized below $15mm$.

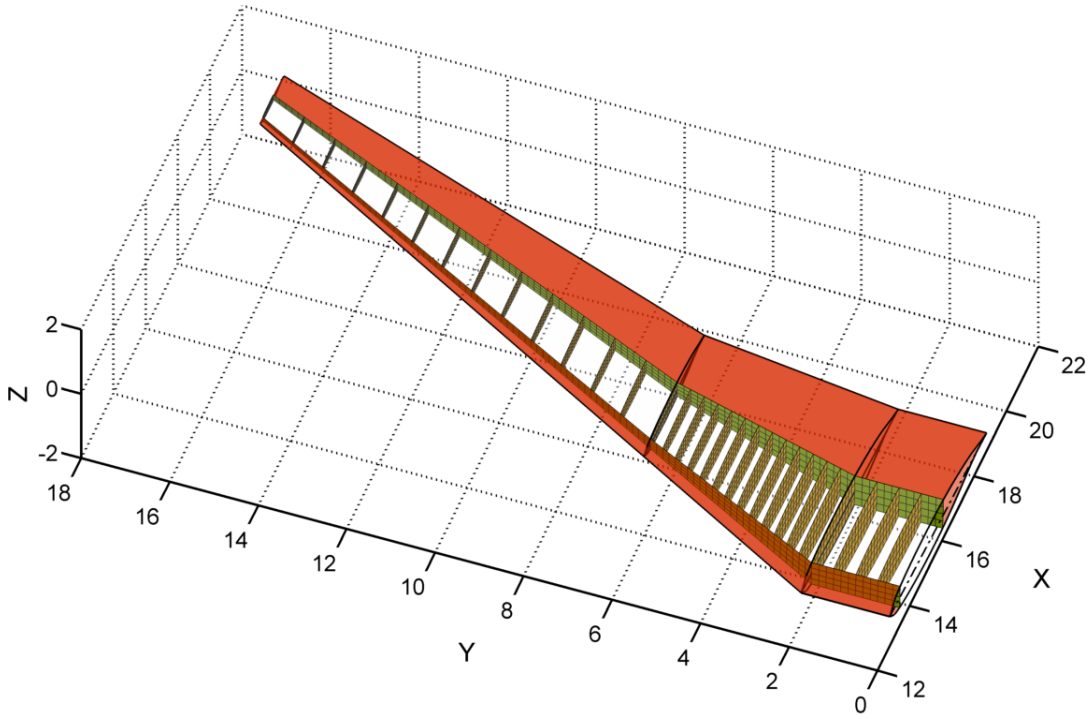

Figure 5.3 *A 3D View of the Generated and Optimized Wing Box Model*

The final structural model also fulfilled both of the considered sizing criteria. A 3D view of the structural model is demonstrated in Figure 5.3, while converged thicknesses of the structural parts with their masses and rib quantities are listed in Table 5.8.

Parts	**Thickness in mm**	**Mass in kg**	**Mass in %**	**Rib Quantity**
Upper Shell	14,8	1121,7	38	-
Lower Shell	13,9	1061,0	36	-
Spar 1	9,4	157,8	5	-
Spar 2	14,8	320,2	10	-
Rib Def. 1	2,0	51,13	2	4
Rib Def. 2	4,7	225,2	8	13
Rib Def. 3	3,2	38,2	1	13
Total	-	2975,3	100	30

Table 5.8 *Structural Modeling Results of the Wing Box Model*

During every topology optimization, the number of ribs in rib definition 2 and rib definition 3 was increased by 1, causing to unequal rib spacing between wing segments. Thus a total rib quantity of 30 was reached at the end of the modeling sequence. In final iteration, the structure of the half wing reached a structural mass of $2975,3kg$. Although the reference mass breakdown analysis from [30] gives an overall half wing structure of approximately $4000kg$, a good comparison is not possible. Because this value includes apart from structure data, other utilities of the wing, which are not taken into account in SMT. Therefore, an empirical wing mass estimation method for aluminum structures of Torenbeek [3] was chosen for the validation. According to this method, an estimated half wing structure mass of $m_{struc} = 2126kg$ with the corresponding parameters of CSR-01 was obtained, which deviates from the generated structure model by about 40%. The leading cause of this deviation relies on applying the sizing optimizations regarding critical stress on the entire structure. As a consequence, most fields of the wing box were oversized that led to a significant increase in wing structure. With the absence of a third spar in the possible landing gear area and secondary structures, such as undercarriage support and the engine support, impacts of oversizing on structural mass can be expected with a deviation less than 40%. According to Figure 2.4, an aircraft with the MTOW of CSR-01 has 28 ribs, which is only two ribs less than modeled structure. The significant cause of this event relies on uneven spacings between rib definitions, which caused to minor excess in the rib number. In the following sections, the results are discussed in detail for the validity of executed optimization processes. Section 5.3.1 shows the general behavior of sizing optimization depending on the load factor, while Section 5.3.2 reveals the behaviors of topology optimization under load factor dependence. In Section 5.3.3, comments about the duration of the simulation process are made. Furthermore, the results of the model optimization process are given in Appendix B in terms of sizing coefficients k_{part} for each part, and the converged FEA output of each iteration .

5.3.1 Sizing Results

The sizing optimization process reveals similar characteristics in both load cases. The first comparison to this conclusion is demonstrated in Figure 5.4, regarding maximum structural displacement and the lowest eigenvalue, with the linear trends between sizing iterations representing the optimization process. More detailed sizing results corresponding to every part and iteration are listed in Appendix B.

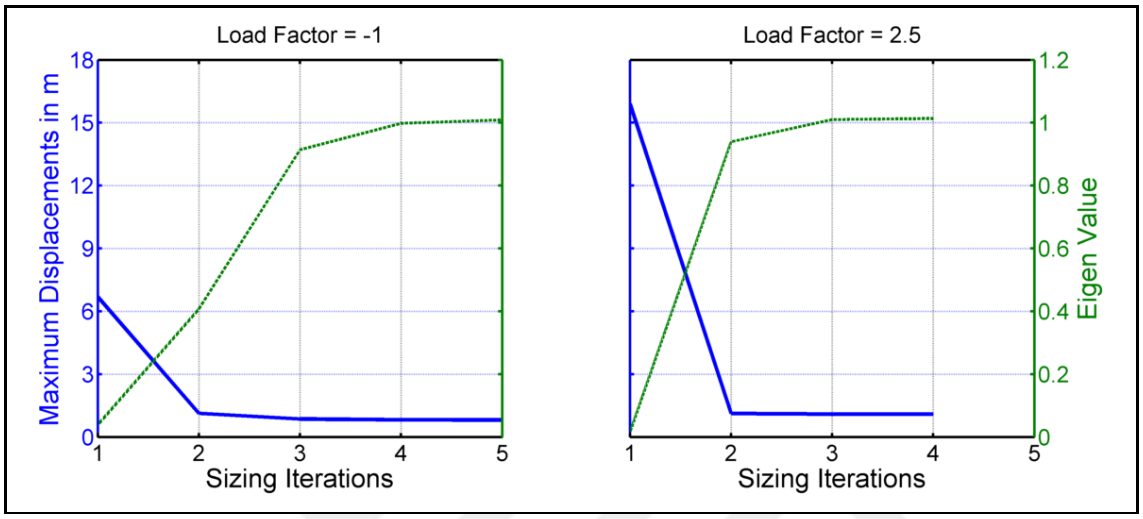

Figure 5.4 *Maximum Displacement and Eigenvalue Results of the Final Topology*

In -1g load case, the maximum displacement dropped rapidly about $5,5m$ in the second iteration, followed by slight changes in later iterations. The eigenvalue of the structure was scaled up with increasing gradient during first two optimizations and brought to λ_{targ} with slighter gradients afterward. The optimization process of 2,5g load case took fewer iterations compared to -1g. In this case, a drop of $14m$ occurred after the first optimization, followed by changes in a matter of millimeters. The scaling of eigenvalue to λ_{targ} took place with a monotonously decreasing slope.

In both cases, the rapid drop in the second iteration is a result of the thickness increase in parts from the first sizing optimization, which was dominated by stress optimization factors $k_{part,\sigma}$. It must also be noted that the maximum displacement dropped to the same level in both load cases. This event results from the linear correlation between strain-stress in Equation (2.5) and Equation (4.5). Slight changes in maximum displacement in the following iterations are a sign of thickness adjustments in order to reach the target eigenvalue λ_{targ}, with $k_{part,\lambda}$ dominating the optimization factors. The increasing slope on eigenvalue line in -1g case reveals that the stress sizing was not sufficient for the stability of the structure so that stability factors took over the sizing during second optimization. Conversely, in -2,5g case, highly scaled stress optimization had an impact on structural stability improvements, by approximating the eigenvalue to λ_{targ} already during the first optimization. Despite not remarkably effecting the maximum displacement and thus σ_{max}, latter sizing optimizations are necessary in the terms of structural stability. For this reason, the user must take this aspect into account during determining the

allowable Δd_{max} as a convergence measure.

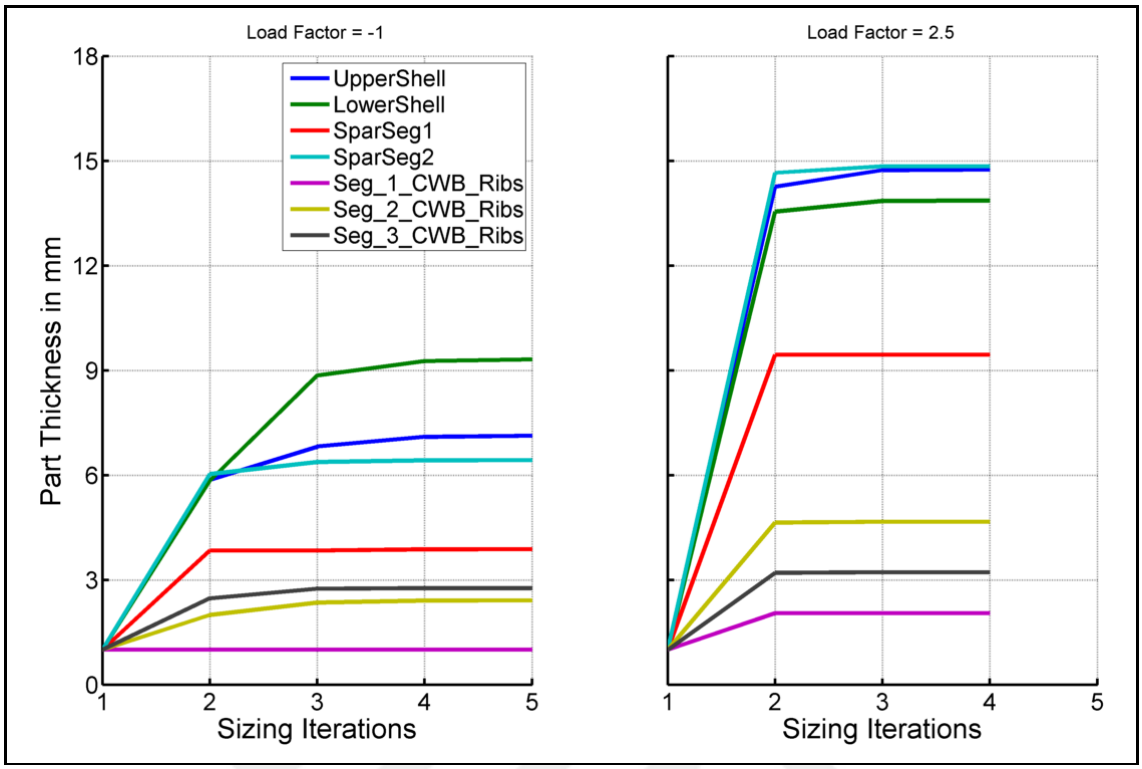

Figure 5.5 *Part Thickness Adjustments of the Final Topology*

Due to opposite acting directions of load cases, structural parts were sized diversely. A comparison for this diversity is shown in Figure 5.5. In -1g case, the lower shell, the upper shell and the second spar segment were sized closely, due to the common occurrence of maximum stress in these parts at the kinked area. Front spar, rib definition 1 and rib definition 2 needed less stress sizing optimizations compared the mentioned three critical parts. It is worthy to note that rib definition 1 wasn't sized throughout all iterations. As per definition, blocking all DOF's of corresponding node set in the finite element geometry prevented rib definition 1 from experiencing any critical stress under current load condition, thus didn't lead to any further optimization. Lower shell was sized against stability in last three optimizations to fulfill the buckle criterion resulted from compression. Another remarkable event is the stability sizing of upper skin in latter optimizations. Although no compression took place in this part, the high amount of shear distribution, especially close to the kink point of the wing structure, caused to shear buckling in some fields of the upper skin, hence led to further stability optimizations. For the same purpose, rear spar segment was also sized against stability in latter optimizations.

In 2,5g case, the impact of the increase in load amount on to the sizing process can be revealed. Also, the unequal three largest sizings show that the critical stresses mostly occurred in rear spar, than in upper shell and lower shell respectively. The vast scale of stress sizing during the first optimization provided in all rib definitions, as well as in front spar a satisfying buckle strength, so that neither stress nor stability optimization was needed any further in these parts. The most critical parts, on

the other hand, needed only a second stability sizing in order to meet the buckle criterion. In consequence of shear stresses, the segments of the lower shell and rear spar were also involved into stability sizing during second optimization.

The iterative optimization process of 2,5g enriched every structural part with a higher amount of thickness than of -1g. This shows that the amount of load factor is the decisive parameter for the sizing of the wing structure, rather than the direction of the load factor. A change in load factor direction may lead to a difference in arrangement of parts regarding the thickness. However, this could be only decisive under equal load factor amounts.

The final sizing iteration is executed to confirm that the structure reached its target eigenvalue, although no major changes in thickness took place. It is worthy to note in this regard that underestimated or overestimated optimization and iteration parameters may lead to more iterations, likewise to an oversized structure. Apart from these aspects, the sizing process also revealed a geometrical problem: A kink in rear spar causes a local stress increase, wherefore both shells and rear spar had to be sized with a remarkable bigger scale than other parts.

5.3.2 Topology Results

The results of topology optimization process are demonstrated in terms of maximum displacement and eigenvalue in Figure 5.6, where every value represents the converged result of the related sizing process. The results show that SMT could

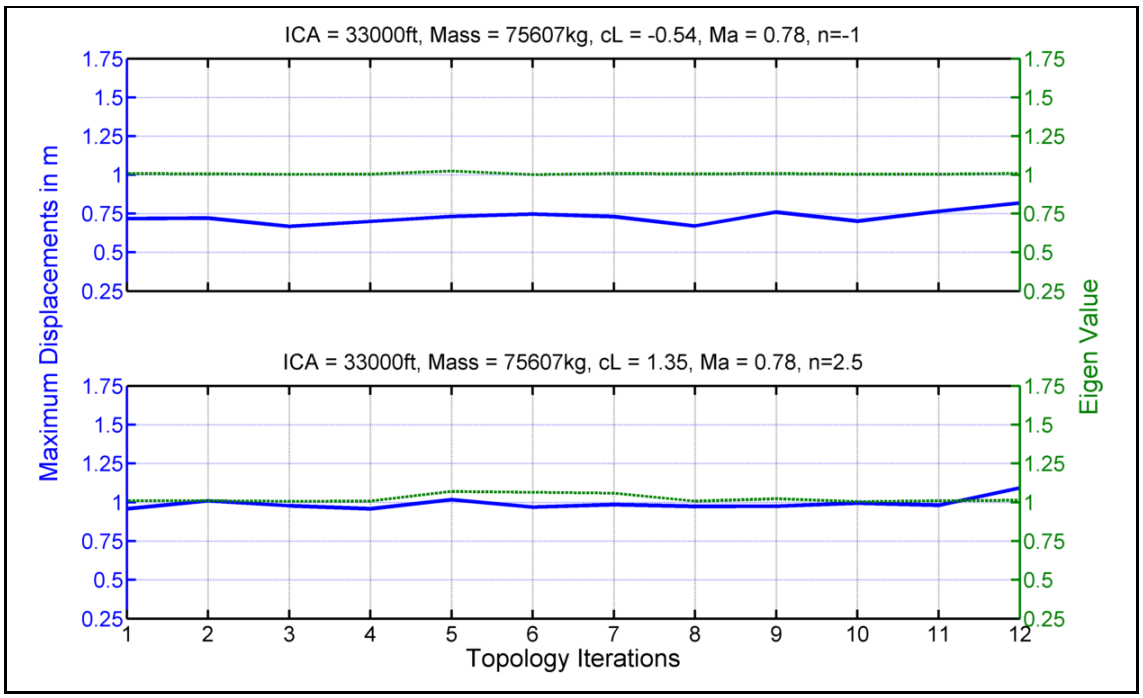

Figure 5.6 *Maximum Displacement and Eigenvalue Diagram of the Modeling Process*

exactly build up a structural model with $\lambda = \lambda_{targ}$ throughout the modeling process in both load cases. With the knowledge of the stability limit being above of stress limit from Section 5.3.1, every iterated structure fulfilled both optimization criteria. Apart from neglectable deviations, the wing structure converged with an absolute maximum displacement of $d_{max} = 0,75m$ in -1g case and $d_{max} = 1m$ in 2,5g case. This progress reveals the linear elastic relation of dominating stress sizing from the first optimization resulted with similar d_{max} in every structural topology of both load cases. Since the magnitude of applied aerodynamic and fuel loads remained same throughout the sizing and topology iterations, the deviation in maximum displacements is a result of changing structural loads based on added ribs and stability sizings. With this result, it can be concluded that the change of structural mass has minor effects on the elastic characteristics of the wing structure under the consideration of static aerodynamics.

A dedication to the relation between the maximum used thickness and the structural mass during structural modeling is also worthy. This aspect is illustrated in Figure 5.7 with maximum reached thickness and the structural mass. In -1g case, a rippled trend on the maximum thickness, as well as on the structural mass can be seen. This rippling exposes an alteration of buckling fields on shells resulting from added ribs during topology optimization. Since the nominal amount of applied loads in this load case does not require a stress sizing dominating the stability strength in the first optimization, latter required stability sizings can significantly lead to a further increase on the shell thicknesses (see Lower Shell on Figure 5.5). As a consequence of rib increment, the aspect ratio of the buckling fields vary during each topology

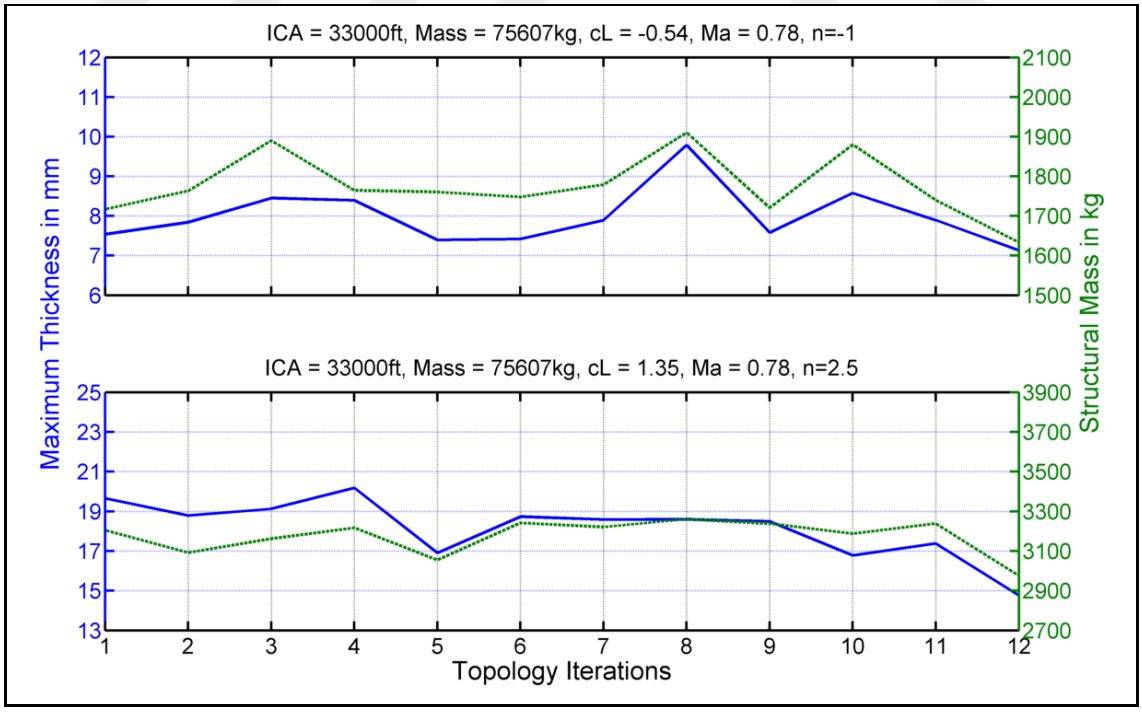

Figure 5.7 *Maximum Thickness and Structural Mass Diagram of the Modeling Process*

optimization, thus causing to buckle occurrences in different forms from topology to topology (refer figures in Appendix B for buckling fields). With both shells having the most significant share concerning structural mass by percentage (see Table 5.8), changes in thickness of these parts due to the alteration of buckling fields also lead to a correlated rippling in total structural mass. The effects of formal changes can also be observed on the trend lines from 2,5g load case. However, the weak effects of stability sizing on the part thickness cause to less rippling in maximum thickness, compared to -1g results.

In either cases, changes in structural mass has direct effects on the maximum displacement. These effects can be observed in topology iterations, where significant peaks in structural mass from Figure 5.7 lead to relative slight peaks in the opposite direction on trend lines of maximum displacement in Figure 5.6. Also a tendency of decreasing structural mass throughout the structural iteration barely observable. Leading causes of this occurrence rely on unequal rib spacing between rib definitions, as well as global part sizings rather than local with current KBE capabilities. Furthermore, striving to balance the structural stability only using ribs cause an unstable change in structural thickness between topologies, whereas additional use of stringers would be helpful to minimize this consequence.

5.3.3 Duration of the Iterative Process

The application was executed on Intel Core i7-4710HQ with features listed in Table 5.9. During the application, only one core of the processor was used. Under these conditions, the entire modeling process took exactly 2 hours and 22 minutes. During the modeling process, it was observed that the import of FEA results from output files into SMT took the majority of the duration. All other sequences, including FEA in CalculiX, took a certain amount of time to be considered with less than 90 seconds. In this regard, the distribution of sizing iterations, the duration for each topology optimization, as well as the total number of the generated elements are given in Figure 5.8.

Parameter	**Value**	**Unit**
CPU Clock Speed	3,30	GHz
CPU Base	64	bit
RAM Capacity	16,0	GB

Table 5.9 *Features of the Used CPU*

An increase in duration along the topology optimization can be noted. Regarding this increase, two aspects are to be detailed:

- The increase in element numbers
- Change in the number of required sizing iterations

The total element number of the structure grew throughout the topology optimization, due to newly added ribs. For example, topology iterations 8 and 11 needed 11 sizing iterations, whereas topology iteration 2 took about 200 seconds longer

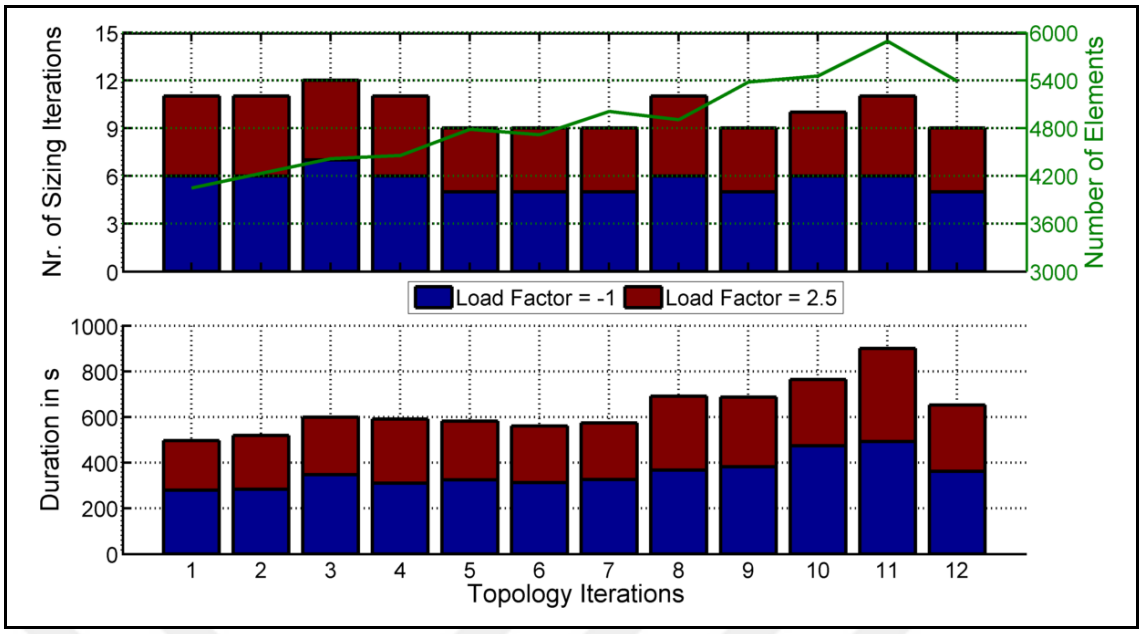

Figure 5.8 *Duration, Sizing and Element Distribution of the Modeling Process*

due to adding 984 elements. However, as the green trend line reveals, the number of elements is not a monotone increasing parameter throughout the entire process. It can also drop despite increasing number of ribs. This event takes place due to the changes in element sizes on the upper and lower shells, resulting from affected element partitioning when new ribs are added. The decrease of total duration in topology iteration 6 can be shown as an example to that.

In connection with the stability sizing, the needed amount of sizing iterations may also vary throughout the topology iteration. This situation can be observed on the upper diagram of Figure 5.8, as the height of blue bars varies in correlation with the maximum sized thickness of the first load case from Figure 5.7. Compared to the increase of element numbers, change of required sizing iterations impacts the total duration dominantly. An example of this occurrence can be seen between iterations 7 and 8 in Figure 5.8, where both load cases from iteration 8 took one more sizing iteration than those from iteration 7. Despite decreasing element number, the increase in the total number of required sizing iterations caused topology iteration 8 to last 118 seconds longer than topology iteration 7. This reveals another significant consequence of altering buckle fields on the total modeling duration with changing topology.

Chapter 6

Conclusions

A frame-based tool SMT was developed for structural modeling of high aspect ratio lifting surfaces. The development of SMT took place using KBE techniques and object-oriented programming philosophy based on a multidisciplinary data exchange format CPACS. In this chapter, the summary of the SMT development, as well as possible improvements in SMT's modular capabilities based on author's recommendations are delineated.

6.1 Summary of the Work

The scope of the work concentrated on four aspects: theoretical background, model generation, model optimization and validation of the tool, where the first two aspects represent the modular capabilities of the SMT.

The theoretical background of SMT was elaborated in Chapter 2. Within this scope, the basic wing box geometry was introduced with its functionalities and placements of structure elements in aircraft. Since the parametric backbone of SMT relied on CPACS data structures, a general definition, as well as the wing parametrization in CPACS was presented. Furthermore, the mechanical background of FEA with shell elements and the central concept of KBE were introduced.

Model generation capabilities were entirely described in Chapter 3. Parametric definitions, requirements, and generation process' of wing box elements considering the input material within SMT were detailed. The process of creating the finite element geometry out of generated wing box elements was described in 4 steps. The structural mass was computed through the volume of generated geometry and imported material properties.After that, load computation methods for aerodynamic and fuel loads were introduced. Depending on the load factor, fuel loads were applied either on the upper skin or the lower skin of the wing box as fuel loads. Aerodynamic loads were derived from stripwise imported coefficients and reference values, and distributed equally to nodes within the covering strip area.

In Chapter 4, the capabilities of SMT in adaptive structural optimizing were detailed, considering the load cases and concepts of lightweight design. The generated structure was analyzed with computed loads using FEA tool CalculiX. Based on the resulting displacements and stresses,two types of optimization methods were applied: sizing and topology optimization. In sizing optimization, the thickness of critical parts was adjusted regarding stress and stability criteria. If the current structural layout did not meet these criteria within the defined limits, topology optimization was applied by changing the rib quantity and thus rib spacing. This process was repeated until a displacement convergence was reached in the FEA simulation. After the displacement convergence in every load case, optimization results were evaluated concerning of part thickness in the purpose of obtaining the structure with sufficient strength against every defined load case.

The modular capabilities of SMT were tested in Chapter 5. During the test, the structure of CSR-01 wing was modeled, with relevant load cases from European Aviation Safety Agency (EASA) Certifications and Specifications (CS)-25. Furthermore, a typical interaction of between the user and the modeling process was shown with the introduction of control parameters. The test application revealed an adequate structural model in regard of optimization criteria and structural mass. Apart from this, it was discovered that stress sizing optimizations in load cases with high load factors dominated the need for stability sizing optimizations, such that less amount of stability iterations were required in 2,5g load case compared to -1g load case.

The test also revealed some possible modeling and optimization deficits of SMT. A consistent sizing procedure on the entire part resulted with an increase in structural mass, whereas a sizing procedure in local fields with critical stress could be more effective. It was also discovered that maximum structural stress tends to increase further in kink spots of structural parts (e.g., rear spar). Avoiding kinked structures could reduce the maximum stress, thus part thickness. The use of single material also led to thickness increase in wing covers and rear spar, due to low material strength. A modeling environment with multiple materials could be a practical solution. Furthermore, an even distribution of buckle fields could result in a more stable stability optimization process.

The user must take the fact of duration into account while defining the control parameters. Setting the thickness limit, as well as iteration limits unrealistically high could cause an enormous amount of modeling time and yet no adequate results. Furthermore, a choice of rough mesh size could be a matter of unsatisfactory results, especially in terms of stress distribution, whereas an exquisitely chosen mesh size could lead to unnecessary extensions in duration.

6.2 Recommendations

The initial structural modeling concept was developed with a high amount of requirements and simplifications, due to limited time. Despite still ensuring satisfactory

modeling on wing structure, these simplifications lead to a low level of detail in generated structure. The KBE capabilities can be expanded under the aspects of user interaction with the software, material, modeling and structural optimization.

User Interaction

Increasing the interaction of the user with the software during the MDO process leads to better modeling and analysis capabilities. Since this fact has been less taken into account during the development of the SMT, the user faces with restrictions during the input of modeling parameters of the wing structure. These restrictions may undermine the advantages of KBE in some parts of modeling. Instances of expanding the authority of the user can be seen in the Multi-Model Generator of TU Delft [19]. Similar expansions could also be applied in SMT. As CPACS offers individual parameter block for external tools, further integration of SMT into CPACS could also help to expand the user authority.

Material Capabilities

In the industrial aircraft development, structures are modeled with multiple materials. Despite the increasing trend from isotropic materials to Carbon Fiber Reinforced Plastics (CFRP) [33], isotropic alloys still take a remarkable percentage in aircraft structures. In this regard, wing structural optimization processes with multiple isotropic materials are demonstrated in [32] and [16], whereas another optimization process using an eight-layer CFRP and aluminum alloy can be found in [12]. For the purpose of contributing to the modeling of more realistic structures in terms of mass estimations, improving material capabilities in use of multiple material combinations, as well as composite materials with own optimization criteria are highly recommended.

Wing Modeling Capabilities

Current wing modeling capabilities enable SMT to handle a very variety of aircraft models. In order to analyze a broader scope of aircraft configurations, these capabilities must be enhanced. In conventional models, secondary wing components such as winglets and strut braces could be modeled as component segments in the next enhancement step. Attachment of various wings with each other would enable unconventional aircraft configurations such as wing box models to be modeled within SMT. Demonstrations to such possible fields can be found in [26].

Structural Modeling Capabilities

During the evaluation process, SMT balances the buckling stability by increasing the material thickness, which leads to oversized and thus heavier structural parts. With the help of well designed CPACS definitions for wing cover structure, stringers and stiffeners that are used in real aircraft structures for the same reason could be modeled as beam elements. Hence, improvements on both structural stability and structural mass can be achieved effectively.

In current development of the SMT, limited capabilities for determining the spar positions, as well as the spar quantity keeps the level of structural detail at a certain point that can be improved. Preferential capability improvements lay on modeling of triple spars, modeling spars with variable ξ along the spanwise direction, as well as enabling real spars end before the wing tip and cross each other. These geometrical improvements require further virtual spar definitions.

With the current rib arrangements of SMT, good estimations can be obtained in terms of mass within the optimization criteria. However, in airplanes with swept wings ribs are arranged perpendicular to the rear spar, where an essential drop in total rib length likewise in the total mass of wing structure can be enabled. Other than rotated ribs around the wing's vertical axis, ribs can also be rotated around the chordwise axis in wings with dihedral angles. In some rib arrangements, member ribs may also intersect each other. Same in spar modeling capabilities, these improvements can be achieved by defining more virtual rib types in mesh segmentation, as well as applying triangular elements in the modeling of the finite element geometry.

Another improvement on spar and rib webs concerning structural stability is to add caps and stiffeners on the spar web. These parts can be implemented as beam structures and would have vital contributions to the optimization process.

Load Modeling Capabilities

SMT is able to generate aerodynamic loads using coefficients generated by an aerodynamic tool based on the rigid model. Therefore, changes of aerodynamic characteristics as the result of elastic deformations on the wing, as it happens in reality, are neglected. Implementation of an aeroelastic equilibrium environment during modeling and optimizing of wing structures can provide accuracy in the structural modeling process. Since SMT already imports the aerodynamic data using CPACS format, an aeroelastic coupling can be created with less effort. In the previous work of the author [31], a concept for such an environment was implemented.

The application of fuel loads only on upper or lower skin, depending on the load factor sign, lets ribs and spars not affected by fuel distribution. This situation leads to a slight underestimate on thicknesses of these parts. An improvement on fuel load computation capability is highly recommended for overcoming this deficit. A

similar fuel load computation method using generated finite element geometry was introduced in [26].

Additional Modeling Capabilities

Current SMT capabilities generate a wing box model with primary structural members. Despite delivering good results, this model concept could be improved with additional modeling capabilities in order to achieve more precisely mass estimation and also create a more realistic environment during FEA. The presence of landing gears and engines attached to the wing structures have not only effects on the structural topology design, but also on the thickness distribution of the structural parts. It is recommended to implement these capabilities as individual objects and rules in SMT, because of their independent parametrization apart from wing modeling.

Another addition to the modeling capabilities could be achieved through modeling the control surfaces of the wing. The positioning of ailerons, spoilers, flaps, and slats provide an essential aspect in additional rib and spar distributions, especially outside of the wing box area, thus providing more accurate mass estimations. Various KBE rules for above mentioned modeling capabilities are detailed in [20], [22], [21] and [26].

Appendix A

CPACS Data Structures

In this appendix, an overview of SMT's data exchange is given. The data exchange is elaborated in terms of input parameters (Appendix A.1) and output parameters (Appendix A.2) in a schematic overview of with regards to the data structure of CPACS v2.0.

A.1 Input Parameters

Input parameters represent the basic needs of SMT from the user in order to sustain the modeling process, which illustrates the content "Input Dataset" from Figure 1.1. These parameters are imported from the elements that are introduced as the top level of the CPACS hierarchy in Figure 2.9. The needed input is grouped with regards to fuel in Figure A.1, to material in Figure A.2, to wing data in Figure A.3 and to aerodynamic loads in Figure A.4.

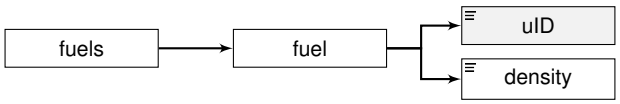

Figure A.1 *Fuel Schema*

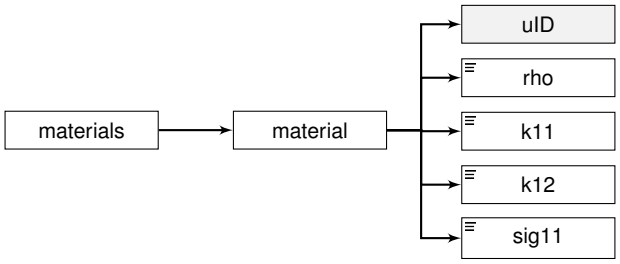

Figure A.2 *Material Schema*

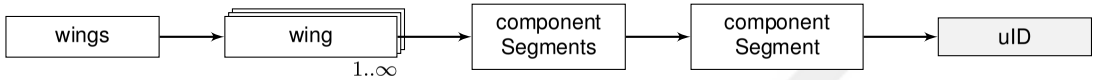

Figure A.3 *Wing Input Schema*

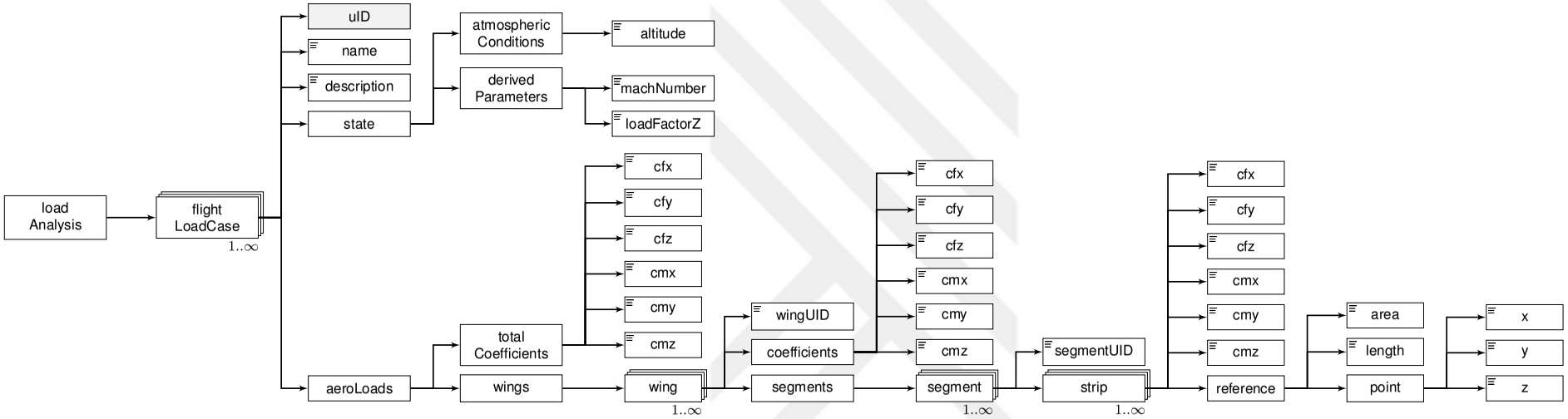

Figure A.4 *Aerodynamic Load Schema*

A.2 Output Parameters

Output parameters represent the content of "Output Dataset" from Figure 1.1. The output data of SMT consists of the structural modeling parameters, which are described in Section 3.1. As these parameters are related to the component segment data of the wing, the main output schema of SMT regarding to the wings is given in Figure A.5. The five output elements of this schema are further described as upperShell & lowerShell in Figure A.6, ribsDefinitions in Figure A.8, spars in Figure A.7, wingFuselageAttachments in Figure A.9 and wingFuelTanks in Figure A.10.

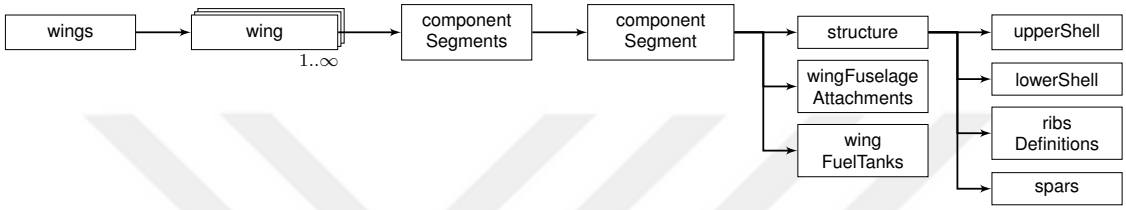

Figure A.5 *Wing Output Schema*

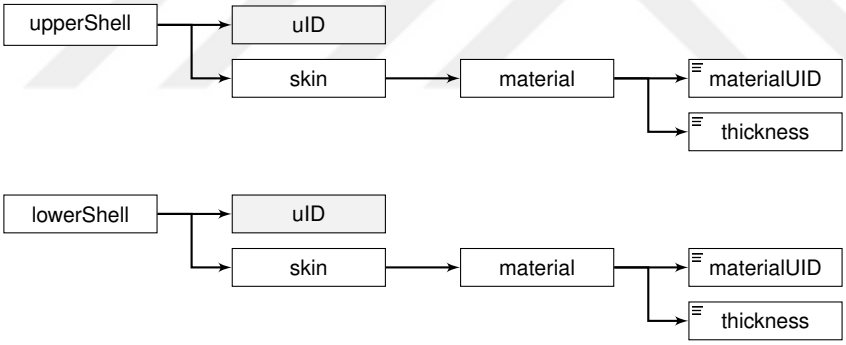

Figure A.6 *Shell Schema*

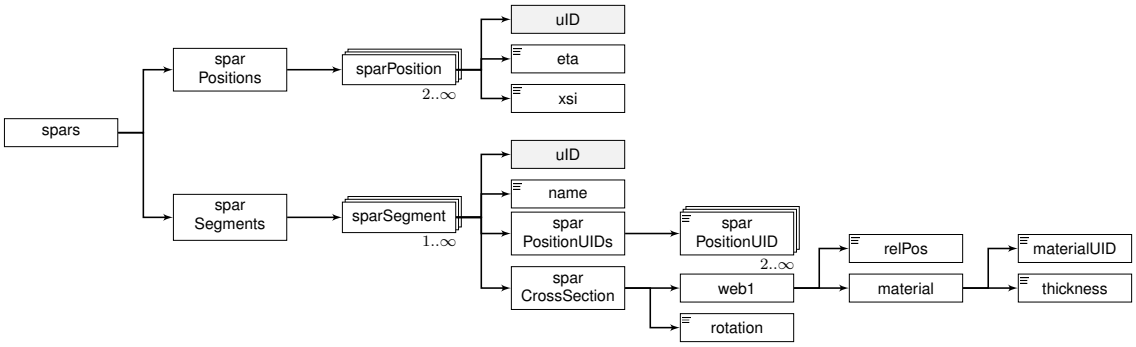

Figure A.7 *Spar Schema*

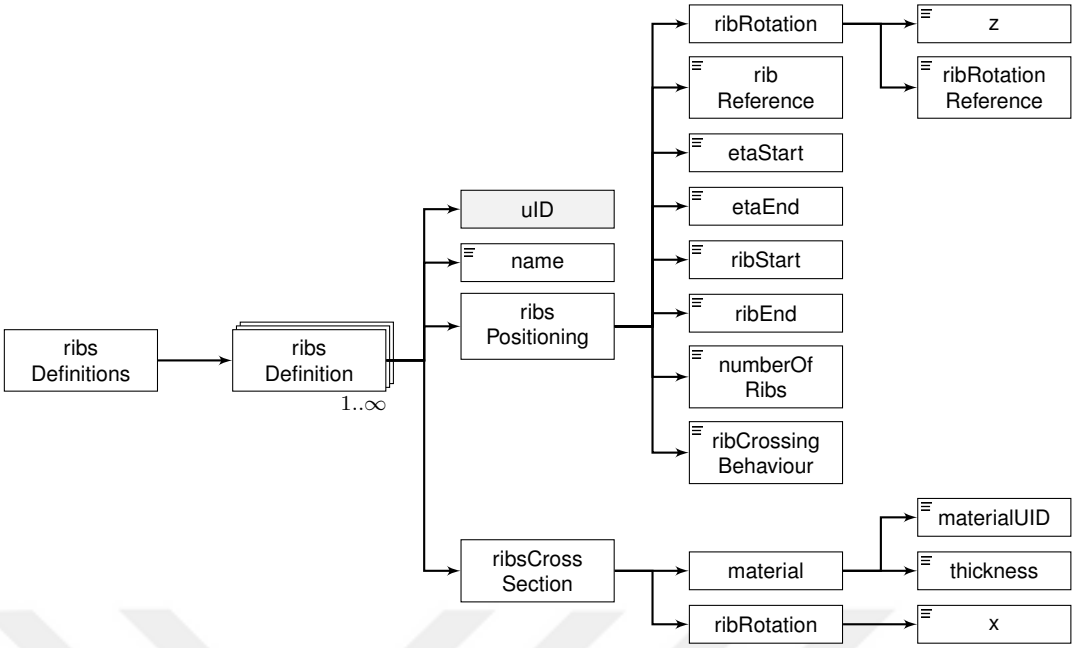

Figure A.8 *Rib Schema*

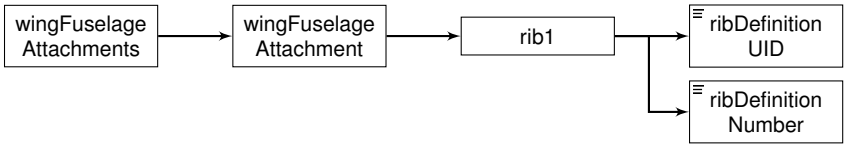

Figure A.9 *Wing-Fuselage Attachment Schema*

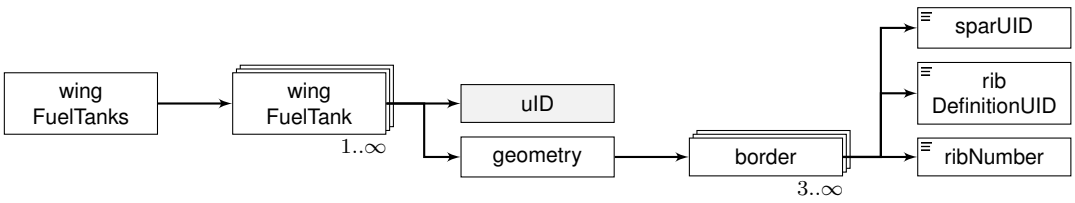

Figure A.10 *Fuel Tank Schema*

Appendix B

FEA Results of the Application

Parts	Iteration 1	Iteration 2	Iteration 3	Iteration 4	Iteration 5	Iteration 6
Upper Shell	1.00	4.97	0.95	0.73	0.66	0.65
Lower Shell	1.00	5.94	0.88	0.58	0.52	0.51
Spar 1	1.00	6.06	0.76	0.59	0.54	0.53
Spar 2	1.00	6.13	0.96	0.74	0.67	0.66
Rib Def. 1	1.00	0.69	0.16	0.12	0.11	0.11
Rib Def. 2	1.00	3.52	0.43	0.32	0.31	0.30
Rib Def. 3	1.00	3.26	0.16	0.13	0.11	0.11

(a) *Stress Sizing Coefficients of Load Case 1*

Parts	Iteration 1	Iteration 2	Iteration 3	Iteration 4	Iteration 5
Upper Shell	1.00	15.09	0.83	0.67	0.66
Lower Shell	1.00	12.15	0.92	0.85	0.84
Spar 1	1.00	15.92	0.76	0.71	0.70
Spar 2	1.00	16.04	0.91	0.85	0.84
Rib Def. 1	1.00	1.40	0.14	0.13	0.13
Rib Def. 2	1.00	6.75	0.41	0.37	0.37
Rib Def. 3	1.00	9.01	0.16	0.15	0.15

(b) *Stress Sizing Coefficients of Load Case 2*

Parts	Iteration 1	Iteration 2	Iteration 3	Iteration 4	Iteration 5	Iteration 6
Upper Shell	1.00	1.00	1.33	1.11	1.02	1.00
Lower Shell	1.00	5.20	1.63	1.11	1.02	1.00
Spar 1	1.00	1.00	1.00	1.01	1.00	1.00
Spar 2	1.00	1.44	1.07	1.02	1.00	1.00
Rib Def. 1	1.00	1.00	1.00	1.00	1.00	1.00
Rib Def. 2	1.00	1.46	1.09	1.02	1.00	1.00
Rib Def. 3	1.00	1.00	1.00	1.00	1.00	1.00

(c) *Stability Sizing Coefficients of Load Case 1*

Parts	Iteration 1	Iteration 2	Iteration 3	Iteration 4	Iteration 5
Upper Shell	1.00	8.42	1.28	1.02	1.00
Lower Shell	1.00	1.00	1.07	1.01	1.00
Spar 1	1.00	1.00	1.00	1.00	1.00
Spar 2	1.00	1.00	1.03	1.00	1.00
Rib Def. 1	1.00	1.00	1.00	1.00	1.00
Rib Def. 2	1.00	1.00	1.06	1.00	1.00
Rib Def. 3	1.00	1.00	1.00	1.00	1.00

(d) *Stability Sizing Coefficients of Load Case 2*

Table B.1 *Optimization Results of Topology 1*

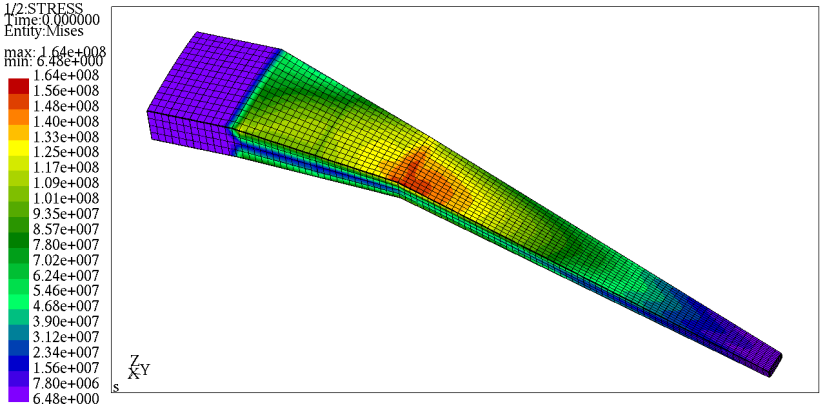

(a) *Stress Distribution of Load Case 1*

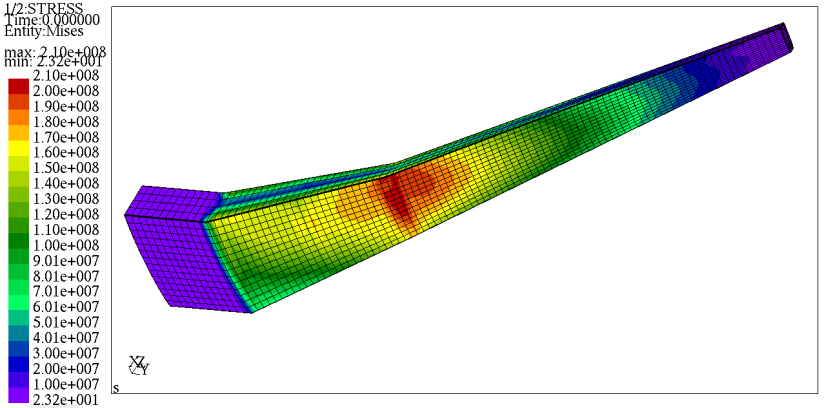

(b) *Stress Distribution of Load Case 2*

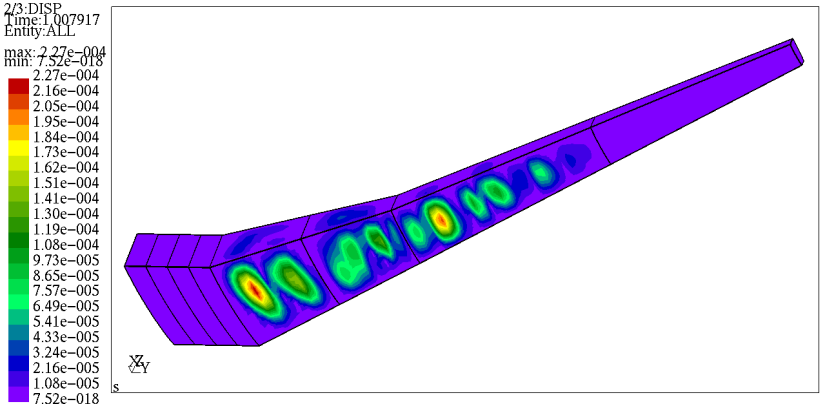

(c) *Buckle Displacements of Load Case 1*

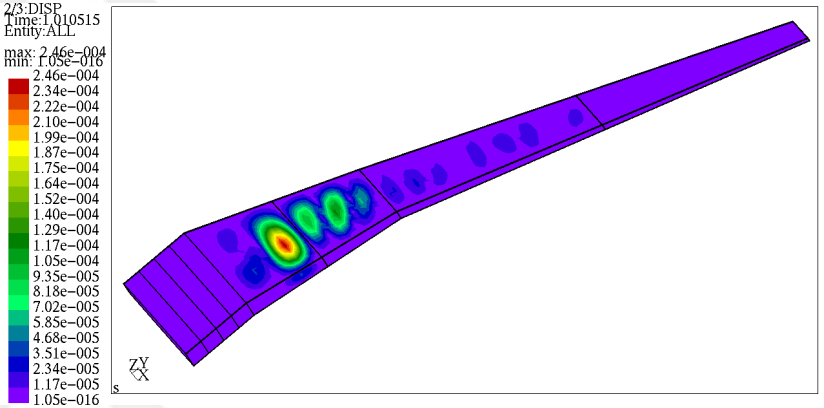

(d) *Buckle Displacements of Load Case 2*

Figure B.1 *Converged FEA Results of Topology 1*

Parts	Iteration 1	Iteration 2	Iteration 3	Iteration 4	Iteration 5	Iteration 6
Upper Shell	1.00	5.54	0.97	0.78	0.71	0.69
Lower Shell	1.00	5.63	0.95	0.61	0.52	0.51
Spar 1	1.00	4.50	0.73	0.59	0.54	0.52
Spar 2	1.00	5.65	1.00	0.81	0.74	0.72
Rib Def. 1	1.00	0.71	0.16	0.12	0.11	0.11
Rib Def. 2	1.00	2.92	0.49	0.37	0.35	0.34
Rib Def. 3	1.00	2.21	0.23	0.18	0.17	0.16

(a) *Stress Sizing Coefficients of Load Case 1*

Parts	Iteration 1	Iteration 2	Iteration 3	Iteration 4	Iteration 5
Upper Shell	1.00	14.37	0.95	0.78	0.77
Lower Shell	1.00	12.76	0.98	0.92	0.91
Spar 1	1.00	10.95	0.79	0.74	0.74
Spar 2	1.00	14.46	0.98	0.92	0.91
Rib Def. 1	1.00	1.71	0.16	0.14	0.14
Rib Def. 2	1.00	6.30	0.46	0.42	0.42
Rib Def. 3	1.00	5.49	0.21	0.20	0.20

(b) *Stress Sizing Coefficients of Load Case 2*

Parts	Iteration 1	Iteration 2	Iteration 3	Iteration 4	Iteration 5	Iteration 6
Upper Shell	1.00	1.74	1.24	1.10	1.03	1.01
Lower Shell	1.00	5.20	1.71	1.17	1.04	1.01
Spar 1	1.00	1.00	1.00	1.02	1.00	1.00
Spar 2	1.00	1.00	1.00	1.02	1.01	1.00
Rib Def. 1	1.00	1.00	1.00	1.00	1.00	1.00
Rib Def. 2	1.00	1.89	1.17	1.04	1.01	1.00
Rib Def. 3	1.00	1.00	1.00	1.00	1.00	1.00

(c) *Stability Sizing Coefficients of Load Case 1*

Parts	Iteration 1	Iteration 2	Iteration 3	Iteration 4	Iteration 5
Upper Shell	1.00	8.39	1.29	1.01	1.00
Lower Shell	1.00	1.00	1.07	1.01	1.00
Spar 1	1.00	1.00	1.00	1.00	1.00
Spar 2	1.00	1.00	1.00	1.00	1.00
Rib Def. 1	1.00	1.00	1.00	1.00	1.00
Rib Def. 2	1.00	1.00	1.03	1.00	1.00
Rib Def. 3	1.00	1.00	1.00	1.00	1.00

(d) *Stability Sizing Coefficients of Load Case 2*

Table B.2 *Optimization Results of Topology 2*

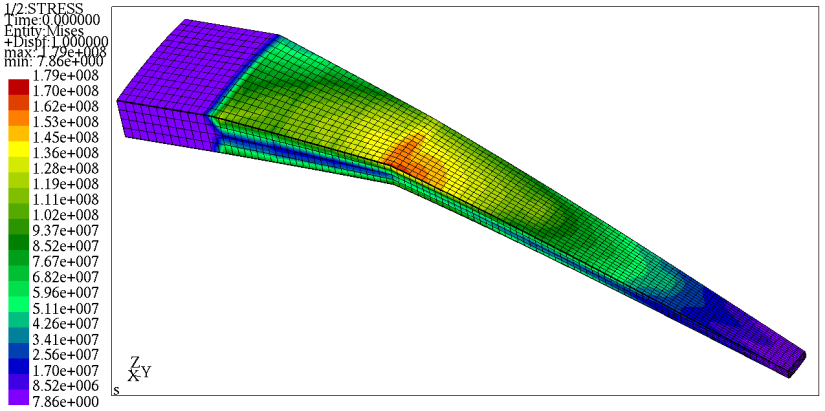

(a) *Stress Distribution of Load Case 1*

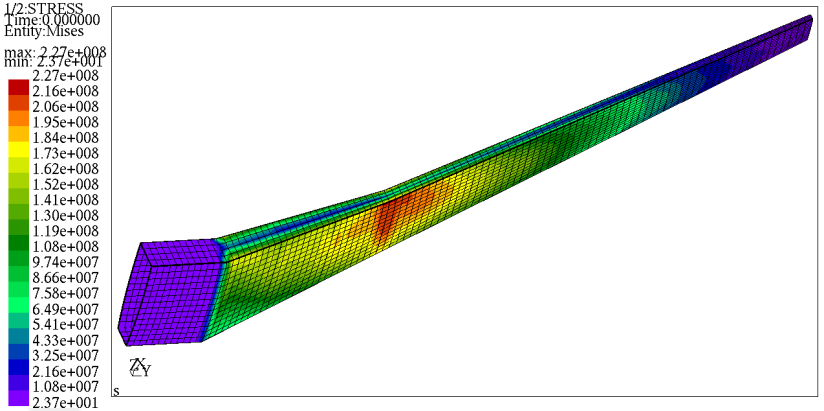

(b) *Stress Distribution of Load Case 2*

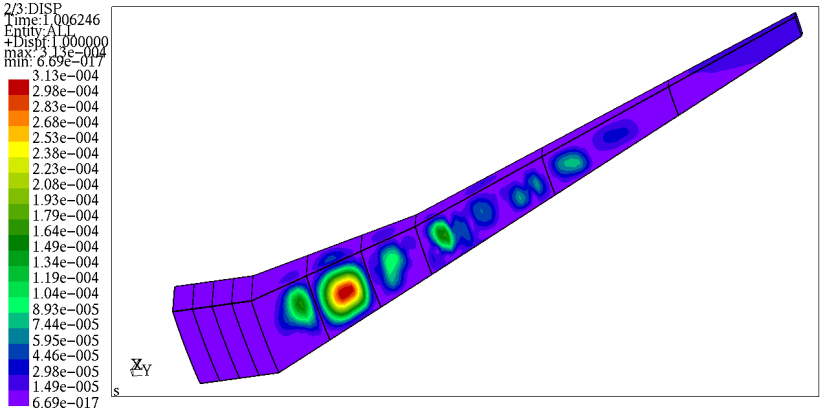

(c) *Buckle Displacements of Load Case 1*

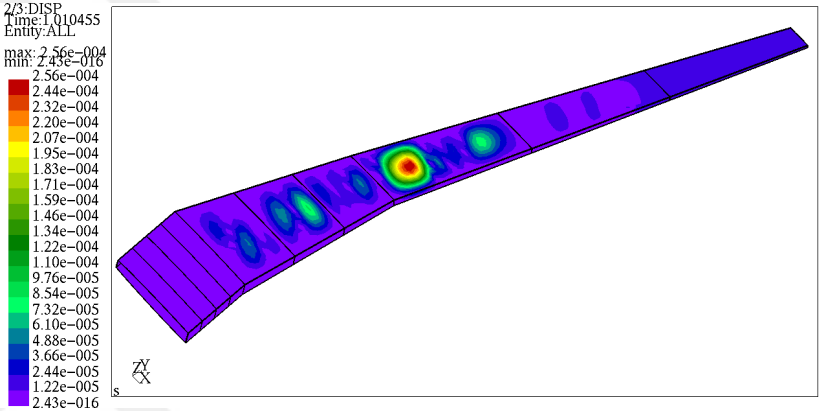

(d) *Buckle Displacements of Load Case 2*

Figure B.2 *Converged FEA Results of Topology 2*

Parts	Iteration 1	Iteration 2	Iteration 3	Iteration 4	Iteration 5	Iteration 6	Iteration 7
Upper Shell	1.00	5.62	0.99	0.81	0.69	0.67	0.66
Lower Shell	1.00	5.59	0.98	0.59	0.49	0.47	0.46
Spar 1	1.00	3.98	0.73	0.58	0.50	0.48	0.48
Spar 2	1.00	5.72	1.02	0.84	0.72	0.69	0.68
Rib Def. 1	1.00	0.71	0.15	0.12	0.11	0.10	0.10
Rib Def. 2	1.00	2.58	0.49	0.38	0.34	0.33	0.33
Rib Def. 3	1.00	1.56	0.27	0.22	0.20	0.19	0.19

(a) *Stress Sizing Coefficients of Load Case 1*

Parts	Iteration 1	Iteration 2	Iteration 3	Iteration 4	Iteration 5
Upper Shell	1.00	14.01	1.00	0.80	0.78
Lower Shell	1.00	12.82	1.01	0.92	0.90
Spar 1	1.00	9.53	0.78	0.71	0.70
Spar 2	1.00	14.07	1.01	0.91	0.89
Rib Def. 1	1.00	1.82	0.17	0.14	0.13
Rib Def. 2	1.00	5.70	0.47	0.43	0.42
Rib Def. 3	1.00	4.07	0.26	0.24	0.23

(b) *Stress Sizing Coefficients of Load Case 2*

Parts	Iteration 1	Iteration 2	Iteration 3	Iteration 4	Iteration 5	Iteration 6	Iteration 7
Upper Shell	1.00	1.00	1.21	1.17	1.05	1.01	1.00
Lower Shell	1.00	5.14	1.78	1.21	1.04	1.01	1.00
Spar 1	1.00	1.00	1.00	1.03	1.01	1.00	1.00
Spar 2	1.00	1.00	1.00	1.03	1.01	1.00	1.00
Rib Def. 1	1.00	1.00	1.00	1.00	1.00	1.00	1.00
Rib Def. 2	1.00	1.81	1.22	1.07	1.02	1.00	1.00
Rib Def. 3	1.00	1.00	1.10	1.02	1.00	1.00	1.00

(c) *Stability Sizing Coefficients of Load Case 1*

Parts	Iteration 1	Iteration 2	Iteration 3	Iteration 4	Iteration 5
Upper Shell	1.00	8.28	1.32	1.04	1.00
Lower Shell	1.00	1.00	1.11	1.02	1.00
Spar 1	1.00	1.00	1.00	1.00	1.00
Spar 2	1.00	1.00	1.00	1.00	1.00
Rib Def. 1	1.00	1.00	1.00	1.00	1.00
Rib Def. 2	1.00	1.90	1.06	1.01	1.00
Rib Def. 3	1.00	1.00	1.00	1.00	1.00

(d) *Stability Sizing Coefficients of Load Case 2*

Table B.3 *Optimization Results of Topology 3*

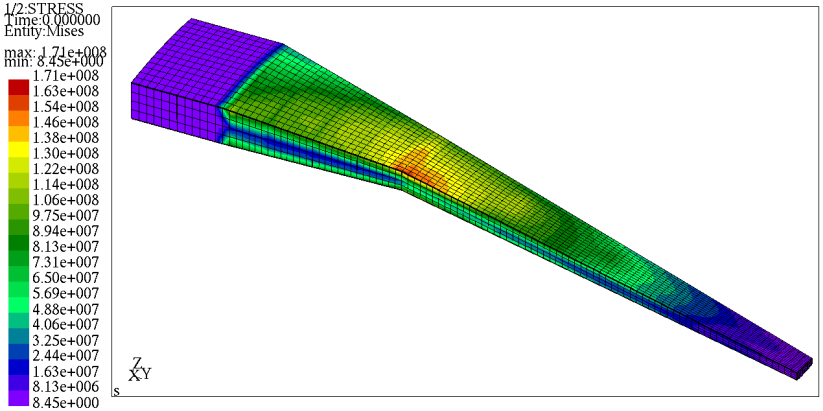

(a) *Stress Distribution of Load Case 1*

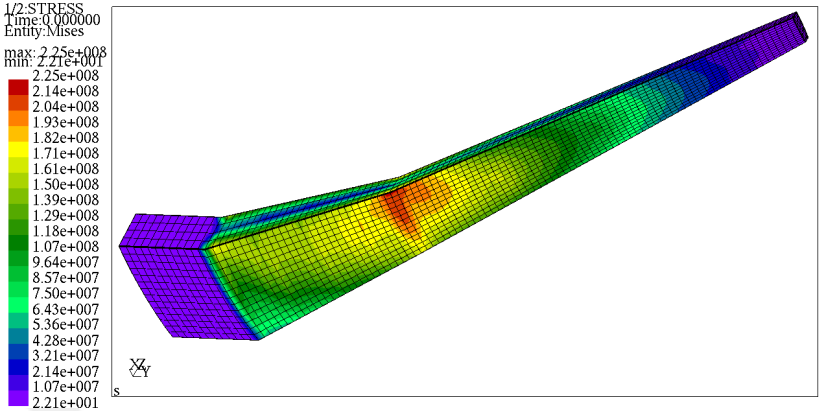

(b) *Stress Distribution of Load Case 2*

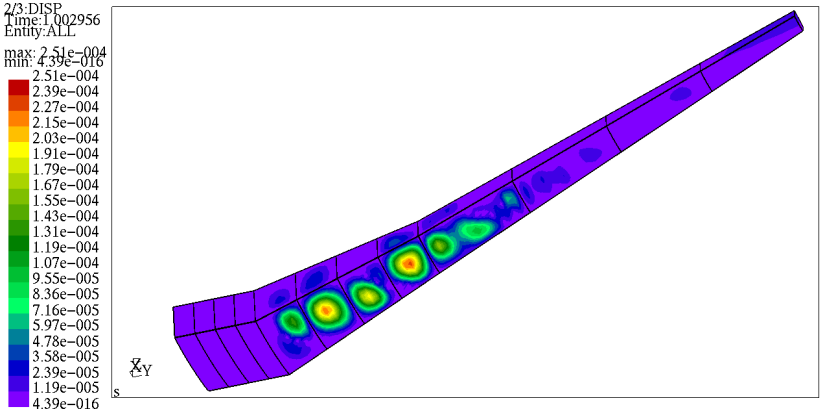

(c) *Buckle Displacements of Load Case 1*

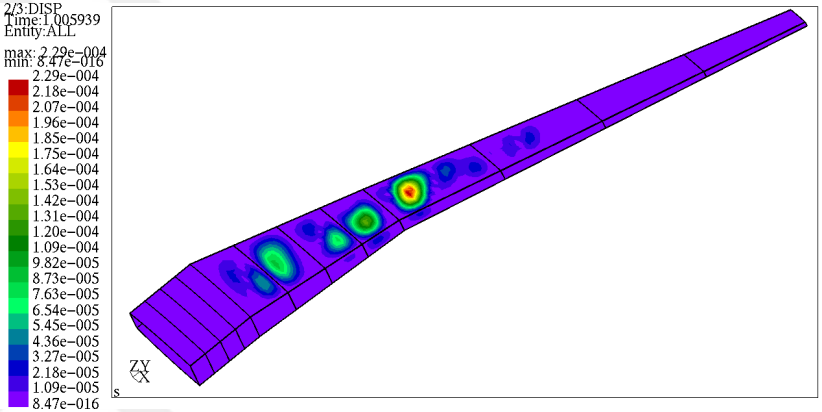

(d) *Buckle Displacements of Load Case 2*

Figure B.3 *Converged FEA Results of Topology 3*

Parts	Iteration 1	Iteration 2	Iteration 3	Iteration 4	Iteration 5	Iteration 6
Upper Shell	1.00	5.75	0.99	0.77	0.69	0.68
Lower Shell	1.00	5.65	0.98	0.60	0.53	0.52
Spar 1	1.00	3.75	0.69	0.53	0.48	0.47
Spar 2	1.00	5.87	1.01	0.79	0.71	0.70
Rib Def. 1	1.00	0.76	0.16	0.12	0.11	0.11
Rib Def. 2	1.00	2.31	0.48	0.37	0.34	0.34
Rib Def. 3	1.00	1.32	0.31	0.26	0.25	0.25

(a) *Stress Sizing Coefficients of Load Case 1*

Parts	Iteration 1	Iteration 2	Iteration 3	Iteration 4	Iteration 5
Upper Shell	1.00	14.07	1.00	0.78	0.75
Lower Shell	1.00	13.07	1.01	0.94	0.93
Spar 1	1.00	9.22	0.74	0.71	0.70
Spar 2	1.00	14.23	1.00	0.93	0.92
Rib Def. 1	1.00	2.02	0.18	0.15	0.14
Rib Def. 2	1.00	5.19	0.48	0.43	0.43
Rib Def. 3	1.00	3.19	0.29	0.27	0.27

(b) *Stress Sizing Coefficients of Load Case 2*

Parts	Iteration 1	Iteration 2	Iteration 3	Iteration 4	Iteration 5	Iteration 6
Upper Shell	1.00	1.00	1.28	1.12	1.02	1.00
Lower Shell	1.00	4.78	1.69	1.14	1.02	1.00
Spar 1	1.00	1.00	1.00	1.01	1.00	1.00
Spar 2	1.00	1.00	1.00	1.00	1.00	1.00
Rib Def. 1	1.00	1.00	1.00	1.00	1.00	1.00
Rib Def. 2	1.00	1.00	1.28	1.07	1.01	1.00
Rib Def. 3	1.00	1.00	1.00	1.02	1.00	1.00

(c) *Stability Sizing Coefficients of Load Case 1*

Parts	Iteration 1	Iteration 2	Iteration 3	Iteration 4	Iteration 5
Upper Shell	1.00	7.88	1.37	1.04	1.00
Lower Shell	1.00	1.00	1.05	1.01	1.00
Spar 1	1.00	1.00	1.00	1.01	1.00
Spar 2	1.00	1.70	1.00	1.01	1.00
Rib Def. 1	1.00	1.00	1.00	1.00	1.00
Rib Def. 2	1.00	1.00	1.08	1.01	1.00
Rib Def. 3	1.00	1.00	1.00	1.01	1.00

(d) *Stability Sizing Coefficients of Load Case 2*

Table B.4 *Optimization Results of Topology 4*

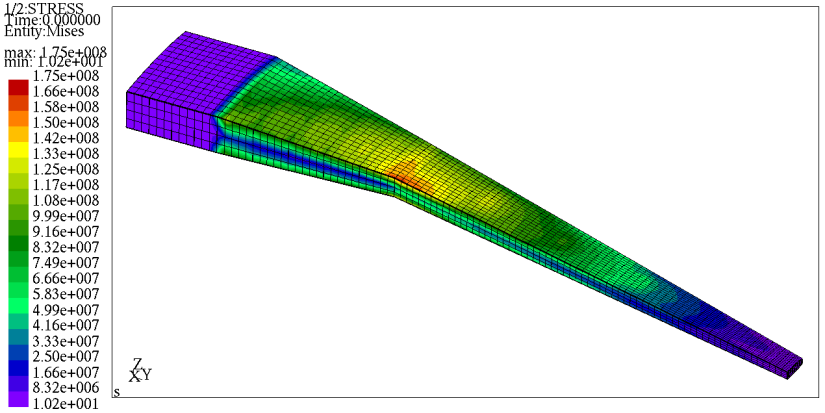

(a) *Stress Distribution of Load Case 1*

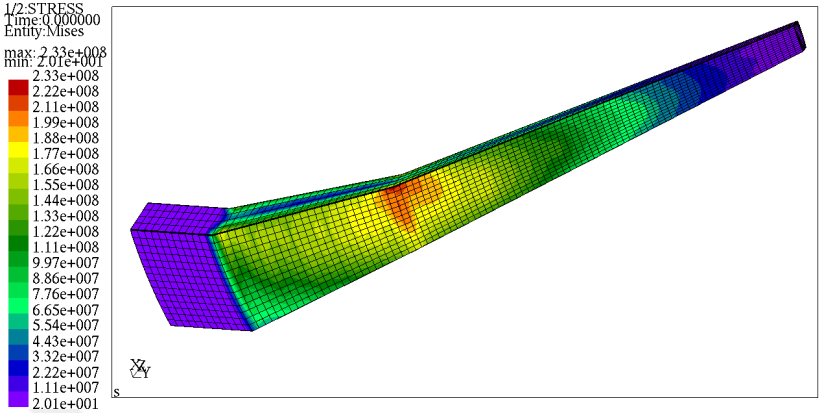

(b) *Stress Distribution of Load Case 2*

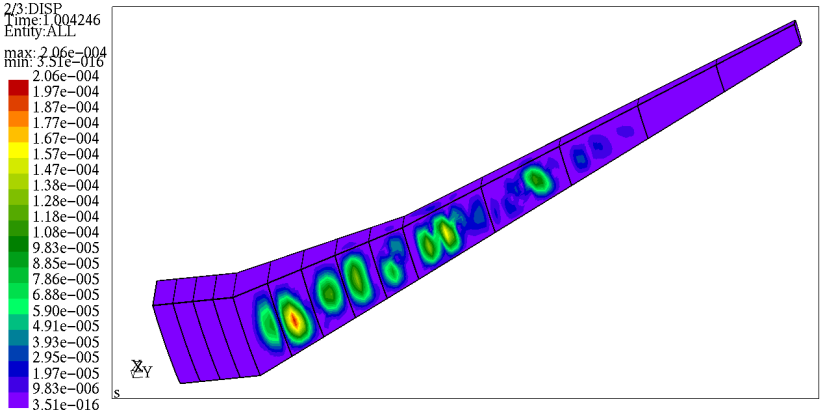

(c) *Buckle Displacements of Load Case 1*

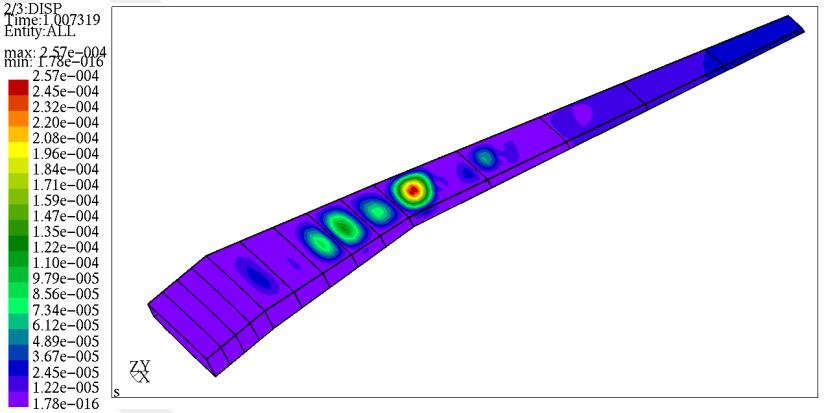

(d) *Buckle Displacements of Load Case 2*

Figure B.4 *Converged FEA Results of Topology 4*

Parts	Iteration 1	Iteration 2	Iteration 3	Iteration 4	Iteration 5
Upper Shell	1.00	5.91	0.99	0.84	0.78
Lower Shell	1.00	5.83	0.98	0.58	0.53
Spar 1	1.00	3.80	0.65	0.57	0.53
Spar 2	1.00	6.06	1.01	0.85	0.79
Rib Def. 1	1.00	0.70	0.14	0.12	0.11
Rib Def. 2	1.00	2.20	0.49	0.40	0.38
Rib Def. 3	1.00	1.33	0.31	0.26	0.25

(a) *Stress Sizing Coefficients of Load Case 1*

Parts	Iteration 1	Iteration 2	Iteration 3	Iteration 4
Upper Shell	1.00	14.47	1.01	0.89
Lower Shell	1.00	13.51	1.01	0.94
Spar 1	1.00	9.42	0.71	0.67
Spar 2	1.00	14.75	0.99	0.92
Rib Def. 1	1.00	1.89	0.16	0.14
Rib Def. 2	1.00	5.00	0.47	0.44
Rib Def. 3	1.00	3.16	0.30	0.28

(b) *Stress Sizing Coefficients of Load Case 2*

Parts	Iteration 1	Iteration 2	Iteration 3	Iteration 4	Iteration 5
Upper Shell	1.00	1.00	1.16	1.08	1.00
Lower Shell	1.00	5.10	1.83	1.12	1.00
Spar 1	1.00	1.00	1.00	1.01	1.00
Spar 2	1.00	1.00	1.00	1.00	1.00
Rib Def. 1	1.00	1.00	1.00	1.00	1.00
Rib Def. 2	1.00	1.79	1.22	1.03	1.00
Rib Def. 3	1.00	1.00	1.10	1.02	1.00

(c) *Stability Sizing Coefficients of Load Case 1*

Parts	Iteration 1	Iteration 2	Iteration 3	Iteration 4
Upper Shell	1.00	8.13	1.17	1.00
Lower Shell	1.00	1.00	1.07	1.00
Spar 1	1.00	1.00	1.04	1.00
Spar 2	1.00	1.00	1.04	1.00
Rib Def. 1	1.00	1.00	1.00	1.00
Rib Def. 2	1.00	3.02	1.04	1.00
Rib Def. 3	1.00	1.00	1.04	1.00

(d) *Stability Sizing Coefficients of Load Case 2*

Table B.5 *Optimization Results of Topology 5*

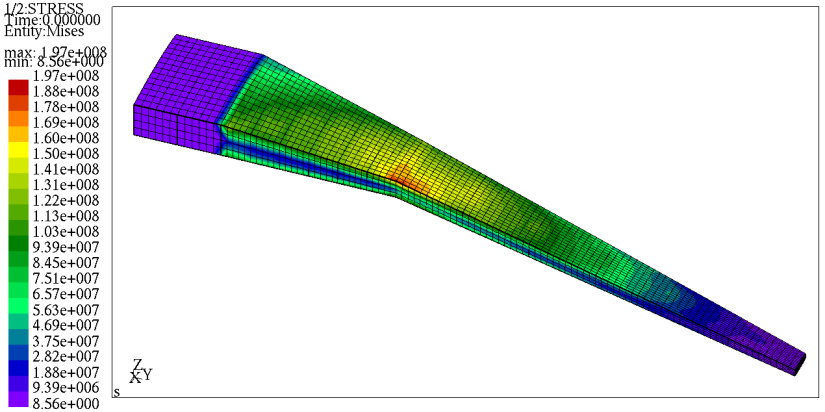

(a) *Stress Distribution of Load Case 1*

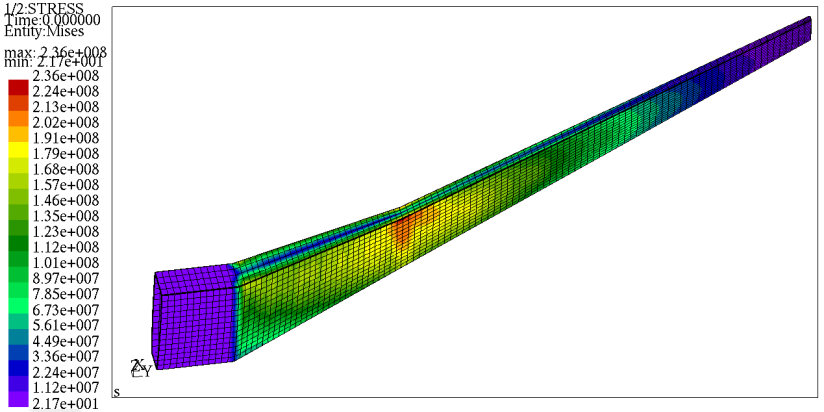

(b) *Stress Distribution of Load Case 2*

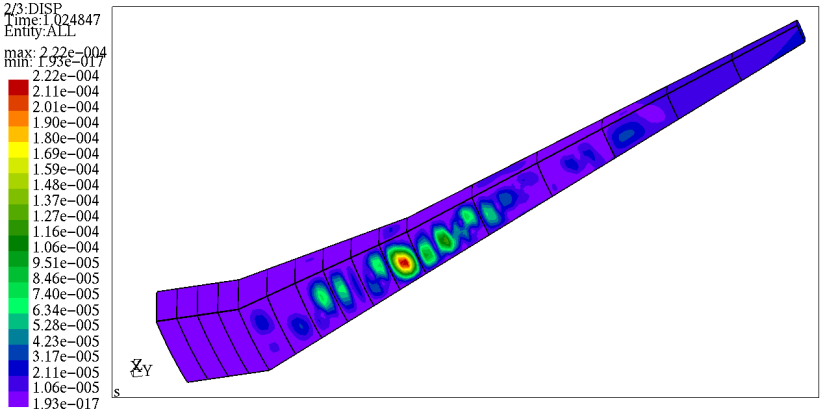

(c) *Buckle Displacements of Load Case 1*

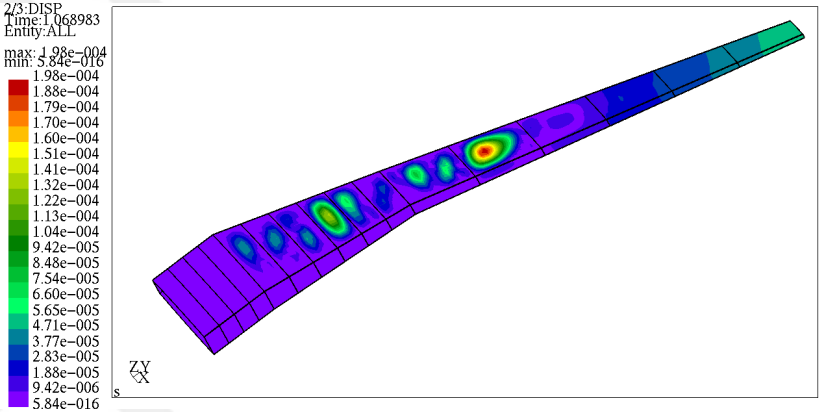

(d) *Buckle Displacements of Load Case 2*

Figure B.5 *Converged FEA Results of Topology 5*

Parts	Iteration 1	Iteration 2	Iteration 3	Iteration 4	Iteration 5
Upper Shell	1.00	5.98	1.00	0.83	0.79
Lower Shell	1.00	5.92	0.99	0.62	0.55
Spar 1	1.00	3.86	0.64	0.54	0.52
Spar 2	1.00	6.13	1.01	0.83	0.79
Rib Def. 1	1.00	0.74	0.15	0.12	0.11
Rib Def. 2	1.00	2.08	0.50	0.41	0.38
Rib Def. 3	1.00	1.35	0.32	0.27	0.26

(a) *Stress Sizing Coefficients of Load Case 1*

Parts	Iteration 1	Iteration 2	Iteration 3	Iteration 4
Upper Shell	1.00	14.64	1.01	0.83
Lower Shell	1.00	13.72	1.01	0.93
Spar 1	1.00	9.54	0.69	0.65
Spar 2	1.00	14.96	0.99	0.91
Rib Def. 1	1.00	2.00	0.17	0.14
Rib Def. 2	1.00	4.77	0.47	0.43
Rib Def. 3	1.00	3.19	0.31	0.29

(b) *Stress Sizing Coefficients of Load Case 2*

Parts	Iteration 1	Iteration 2	Iteration 3	Iteration 4	Iteration 5
Upper Shell	1.00	1.00	1.19	1.05	1.00
Lower Shell	1.00	4.83	1.71	1.14	1.00
Spar 1	1.00	1.00	1.00	1.00	1.00
Spar 2	1.00	1.00	1.00	1.02	1.00
Rib Def. 1	1.00	1.00	1.00	1.00	1.00
Rib Def. 2	1.00	2.06	1.20	1.08	1.00
Rib Def. 3	1.00	1.00	1.00	1.00	1.00

(c) *Stability Sizing Coefficients of Load Case 1*

Parts	Iteration 1	Iteration 2	Iteration 3	Iteration 4
Upper Shell	1.00	7.83	1.28	1.00
Lower Shell	1.00	1.00	1.08	1.00
Spar 1	1.00	1.00	1.03	1.00
Spar 2	1.00	1.00	1.00	1.00
Rib Def. 1	1.00	1.00	1.00	1.00
Rib Def. 2	1.00	2.61	1.08	1.00
Rib Def. 3	1.00	1.00	1.00	1.00

(d) *Stability Sizing Coefficients of Load Case 2*

Table B.6 *Optimization Results of Topology 6*

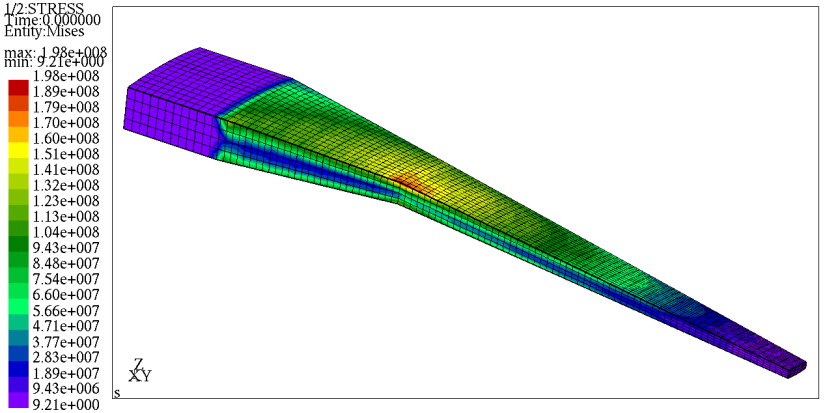

(a) *Stress Distribution of Load Case 1*

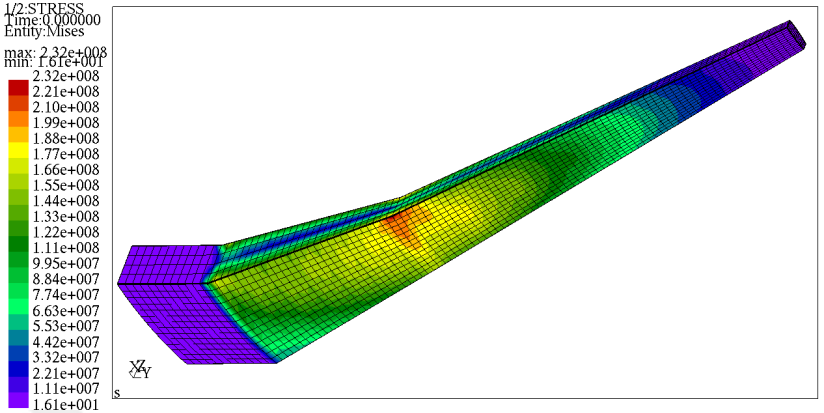

(b) *Stress Distribution of Load Case 2*

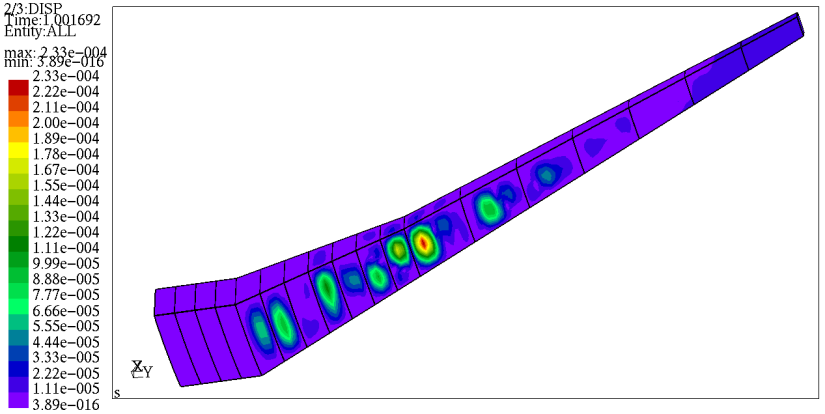

(c) *Buckle Displacements of Load Case 1*

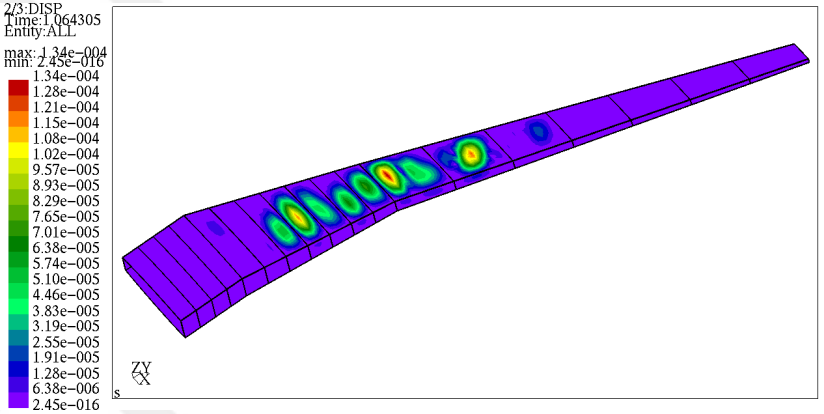

(d) *Buckle Displacements of Load Case 2*

Figure B.6 *Converged FEA Results of Topology 6*

Parts	Iteration 1	Iteration 2	Iteration 3	Iteration 4	Iteration 5
Upper Shell	1.00	6.00	1.01	0.81	0.76
Lower Shell	1.00	5.94	1.00	0.61	0.57
Spar 1	1.00	3.85	0.64	0.52	0.49
Spar 2	1.00	6.16	1.01	0.80	0.76
Rib Def. 1	1.00	0.69	0.14	0.11	0.10
Rib Def. 2	1.00	2.01	0.49	0.36	0.34
Rib Def. 3	1.00	1.36	0.32	0.27	0.26

(a) *Stress Sizing Coefficients of Load Case 1*

Parts	Iteration 1	Iteration 2	Iteration 3	Iteration 4
Upper Shell	1.00	14.66	1.02	0.84
Lower Shell	1.00	13.78	1.02	0.96
Spar 1	1.00	9.51	0.68	0.66
Spar 2	1.00	15.00	1.00	0.94
Rib Def. 1	1.00	1.88	0.16	0.13
Rib Def. 2	1.00	4.62	0.47	0.43
Rib Def. 3	1.00	3.20	0.32	0.30

(b) *Stress Sizing Coefficients of Load Case 2*

Parts	Iteration 1	Iteration 2	Iteration 3	Iteration 4	Iteration 5
Upper Shell	1.00	1.00	1.23	1.07	1.00
Lower Shell	1.00	5.02	1.73	1.08	1.00
Spar 1	1.00	1.00	1.00	1.01	1.00
Spar 2	1.00	1.00	1.00	1.01	1.00
Rib Def. 1	1.00	1.00	1.00	1.00	1.00
Rib Def. 2	1.00	2.08	1.40	1.05	1.00
Rib Def. 3	1.00	1.00	1.00	1.01	1.00

(c) *Stability Sizing Coefficients of Load Case 1*

Parts	Iteration 1	Iteration 2	Iteration 3	Iteration 4
Upper Shell	1.00	8.13	1.27	1.00
Lower Shell	1.00	1.00	1.04	1.00
Spar 1	1.00	1.00	1.03	1.00
Spar 2	1.00	1.00	1.03	1.00
Rib Def. 1	1.00	1.00	1.00	1.00
Rib Def. 2	1.00	3.08	1.08	1.00
Rib Def. 3	1.00	1.00	1.03	1.00

(d) *Stability Sizing Coefficients of Load Case 2*

Table B.7 *Optimization Results of Topology 7*

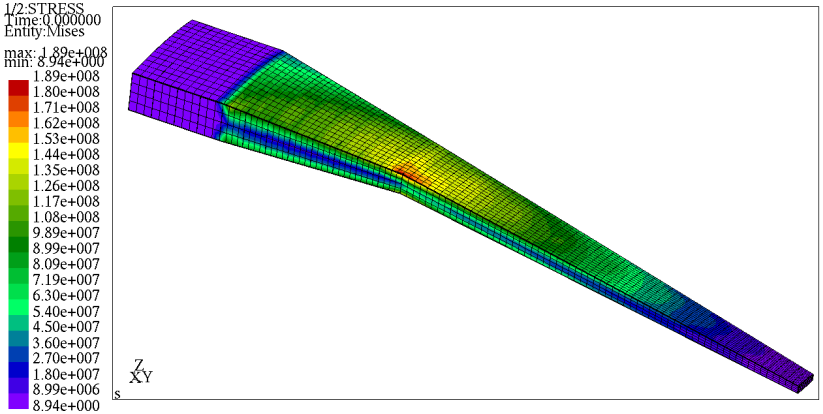

(a) *Stress Distribution of Load Case 1*

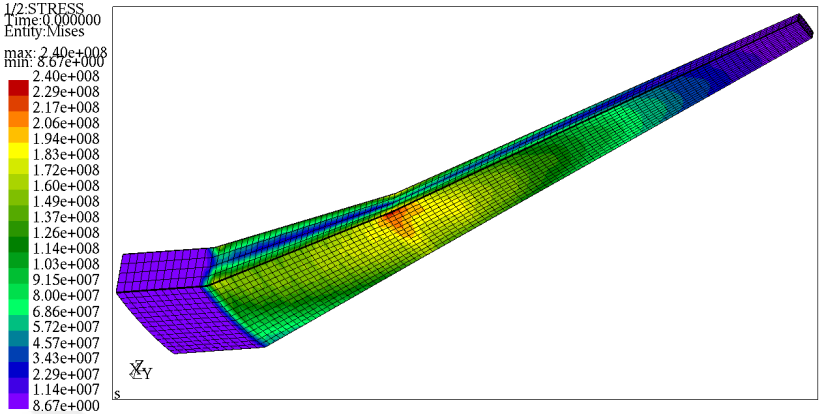

(b) *Stress Distribution of Load Case 2*

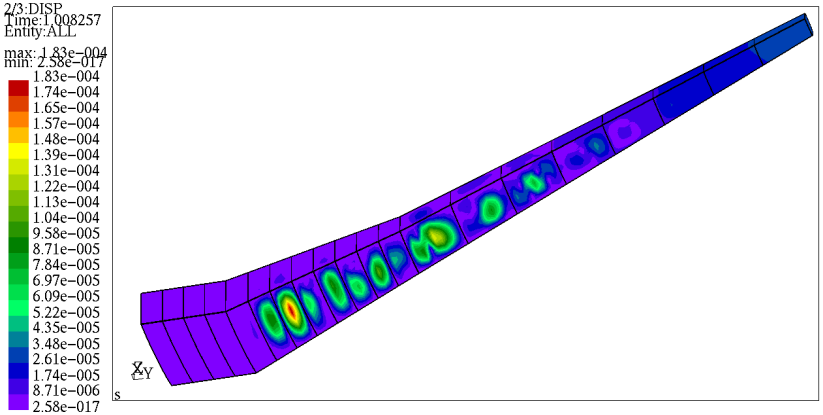

(c) *Buckle Displacements of Load Case 1*

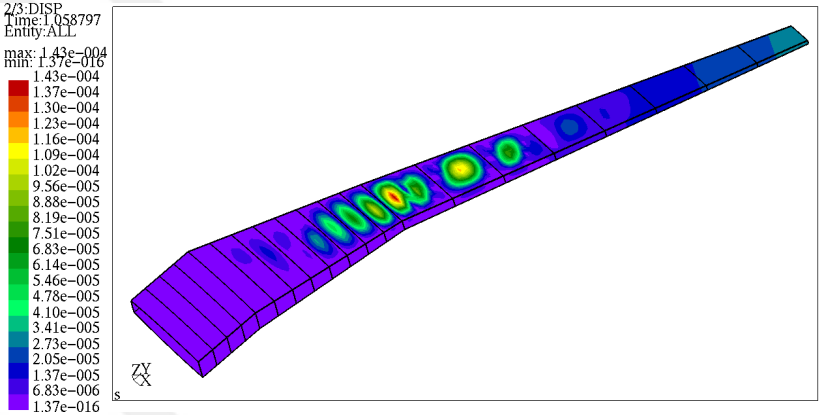

(d) *Buckle Displacements of Load Case 2*

Figure B.7 *Converged FEA Results of Topology 7*

Parts	Iteration 1	Iteration 2	Iteration 3	Iteration 4	Iteration 5	Iteration 6
Upper Shell	1.00	6.01	1.00	0.71	0.65	0.64
Lower Shell	1.00	5.95	0.99	0.68	0.61	0.60
Spar 1	1.00	3.88	0.64	0.44	0.41	0.40
Spar 2	1.00	6.18	1.01	0.71	0.64	0.63
Rib Def. 1	1.00	0.77	0.15	0.11	0.10	0.10
Rib Def. 2	1.00	2.02	0.44	0.31	0.29	0.28
Rib Def. 3	1.00	1.37	0.32	0.23	0.21	0.21

(a) *Stress Sizing Coefficients of Load Case 1*

Parts	Iteration 1	Iteration 2	Iteration 3	Iteration 4	Iteration 5
Upper Shell	1.00	14.66	1.02	0.86	0.85
Lower Shell	1.00	13.80	1.02	0.96	0.95
Spar 1	1.00	9.56	0.68	0.65	0.64
Spar 2	1.00	15.08	1.00	0.93	0.93
Rib Def. 1	1.00	2.09	0.17	0.14	0.14
Rib Def. 2	1.00	4.71	0.46	0.44	0.43
Rib Def. 3	1.00	3.21	0.32	0.30	0.30

(b) *Stress Sizing Coefficients of Load Case 2*

Parts	Iteration 1	Iteration 2	Iteration 3	Iteration 4	Iteration 5	Iteration 6
Upper Shell	1.00	1.00	1.45	1.10	1.02	1.01
Lower Shell	1.00	4.84	1.52	1.12	1.03	1.01
Spar 1	1.00	1.00	1.07	1.02	1.00	1.00
Spar 2	1.00	1.39	1.06	1.02	1.00	1.00
Rib Def. 1	1.00	1.00	1.00	1.00	1.00	1.00
Rib Def. 2	1.00	2.59	1.27	1.04	1.01	1.00
Rib Def. 3	1.00	1.43	1.22	1.04	1.01	1.00

(c) *Stability Sizing Coefficients of Load Case 1*

Parts	Iteration 1	Iteration 2	Iteration 3	Iteration 4	Iteration 5
Upper Shell	1.00	7.79	1.24	1.02	1.00
Lower Shell	1.00	1.00	1.06	1.01	1.00
Spar 1	1.00	1.00	1.02	1.00	1.00
Spar 2	1.00	1.00	1.00	1.00	1.00
Rib Def. 1	1.00	1.00	1.00	1.00	1.00
Rib Def. 2	1.00	2.58	1.00	1.00	1.00
Rib Def. 3	1.00	1.00	1.03	1.00	1.00

(d) *Stability Sizing Coefficients of Load Case 2*

Table B.8 *Optimization Results of Topology 8*

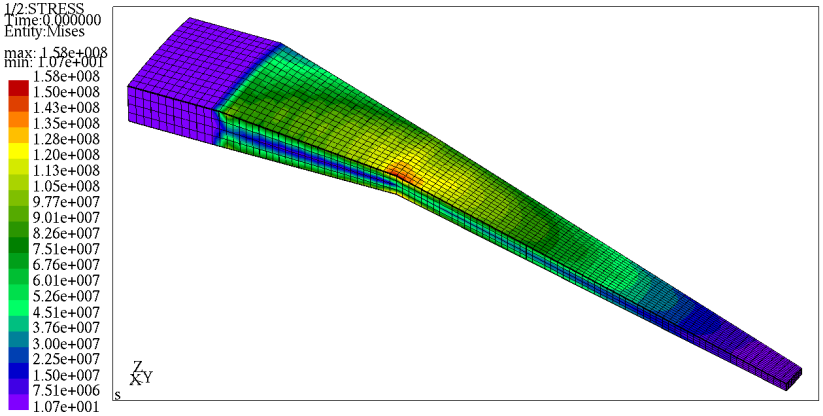

(a) *Stress Distribution of Load Case 1*

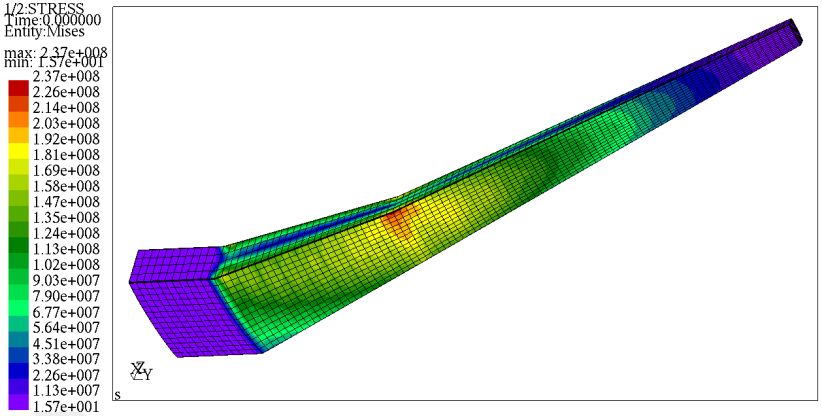

(b) *Stress Distribution of Load Case 2*

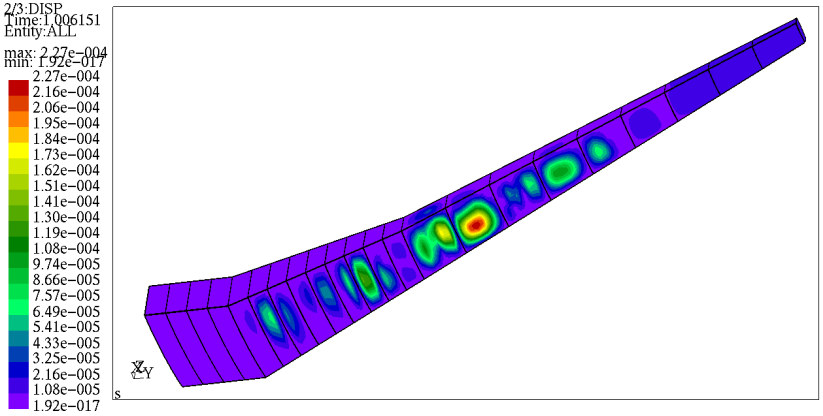

(c) *Buckle Displacements of Load Case 1*

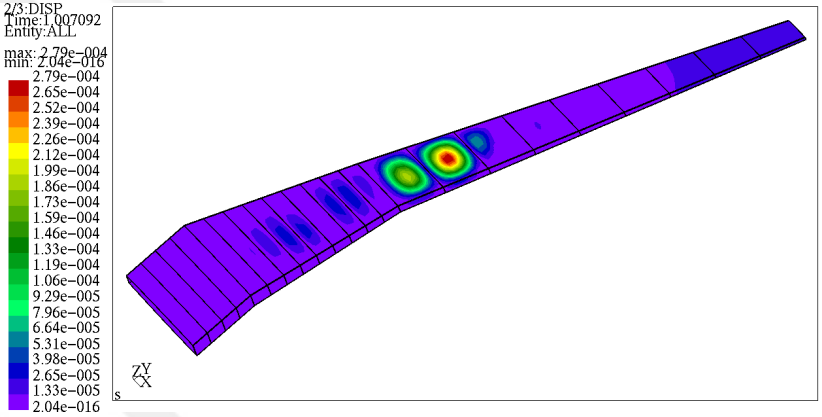

(d) *Buckle Displacements of Load Case 2*

Figure B.8 *Converged FEA Results of Topology 8*

Parts	Iteration 1	Iteration 2	Iteration 3	Iteration 4	Iteration 5
Upper Shell	1.00	6.00	1.00	0.83	0.79
Lower Shell	1.00	5.94	1.00	0.66	0.61
Spar 1	1.00	3.87	0.64	0.53	0.50
Spar 2	1.00	6.17	1.00	0.82	0.78
Rib Def. 1	1.00	0.73	0.15	0.12	0.11
Rib Def. 2	1.00	1.97	0.45	0.37	0.36
Rib Def. 3	1.00	1.32	0.33	0.26	0.25

(a) *Stress Sizing Coefficients of Load Case 1*

Parts	Iteration 1	Iteration 2	Iteration 3	Iteration 4
Upper Shell	1.00	14.62	1.02	0.85
Lower Shell	1.00	13.79	1.02	0.97
Spar 1	1.00	9.55	0.68	0.65
Spar 2	1.00	15.04	1.00	0.94
Rib Def. 1	1.00	1.99	0.17	0.14
Rib Def. 2	1.00	4.58	0.45	0.43
Rib Def. 3	1.00	3.12	0.33	0.31

(b) *Stress Sizing Coefficients of Load Case 2*

Parts	Iteration 1	Iteration 2	Iteration 3	Iteration 4	Iteration 5
Upper Shell	1.00	1.00	1.20	1.05	1.00
Lower Shell	1.00	4.98	1.61	1.09	1.00
Spar 1	1.00	1.00	1.08	1.01	1.00
Spar 2	1.00	1.00	1.00	1.01	1.00
Rib Def. 1	1.00	1.00	1.00	1.00	1.00
Rib Def. 2	1.00	2.33	1.18	1.03	1.00
Rib Def. 3	1.00	1.00	1.19	1.02	1.00

(c) *Stability Sizing Coefficients of Load Case 1*

Parts	Iteration 1	Iteration 2	Iteration 3	Iteration 4
Upper Shell	1.00	8.00	1.27	1.00
Lower Shell	1.00	1.00	1.04	1.00
Spar 1	1.00	1.00	1.00	1.00
Spar 2	1.00	1.00	1.00	1.00
Rib Def. 1	1.00	1.00	1.00	1.00
Rib Def. 2	1.00	1.00	1.03	1.00
Rib Def. 3	1.00	1.00	1.00	1.00

(d) *Stability Sizing Coefficients of Load Case 2*

Table B.9 *Optimization Results of Topology 9*

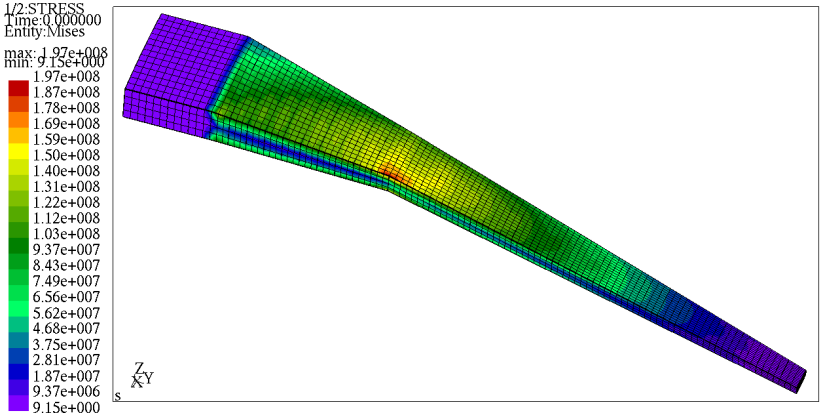

(a) *Stress Distribution of Load Case 1*

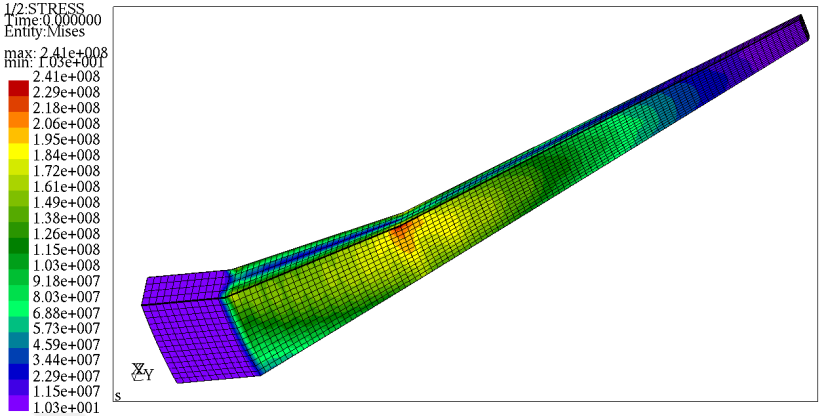

(b) *Stress Distribution of Load Case 2*

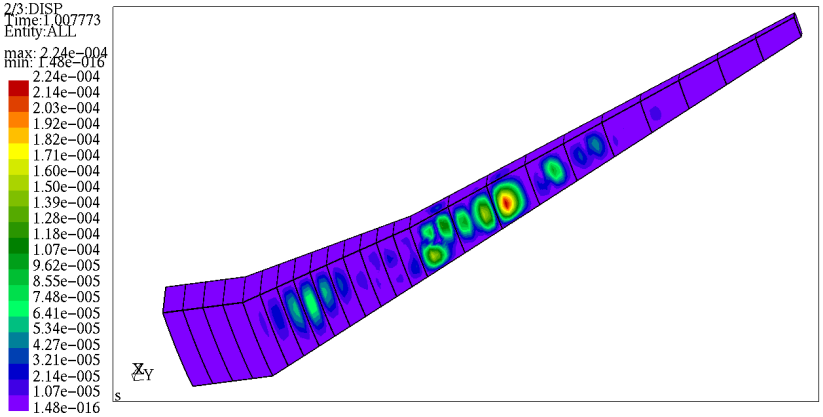

(c) *Buckle Displacements of Load Case 1*

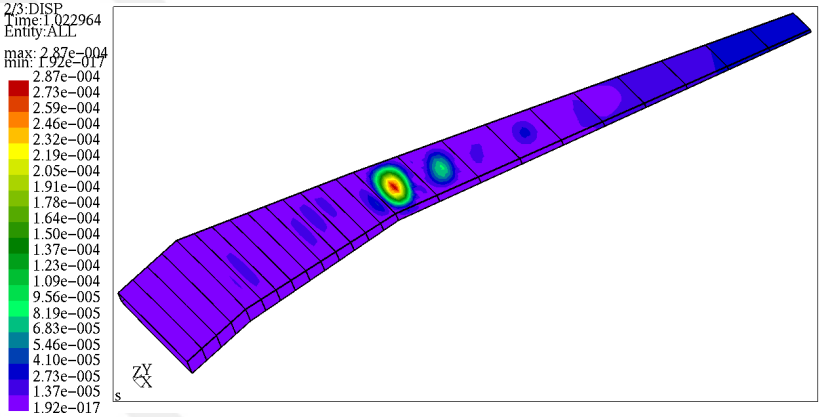

(d) *Buckle Displacements of Load Case 2*

Figure B.9 *Converged FEA Results of Topology 9*

Parts	Iteration 1	Iteration 2	Iteration 3	Iteration 4	Iteration 5	Iteration 6
Upper Shell	1.00	5.97	1.00	0.77	0.72	0.71
Lower Shell	1.00	5.93	1.00	0.65	0.60	0.59
Spar 1	1.00	3.85	0.65	0.50	0.46	0.46
Spar 2	1.00	6.15	1.00	0.77	0.71	0.70
Rib Def. 1	1.00	0.69	0.14	0.11	0.10	0.10
Rib Def. 2	1.00	2.00	0.41	0.29	0.28	0.27
Rib Def. 3	1.00	1.36	0.32	0.25	0.24	0.24

(a) *Stress Sizing Coefficients of Load Case 1*

Parts	Iteration 1	Iteration 2	Iteration 3	Iteration 4
Upper Shell	1.00	14.54	1.03	0.92
Lower Shell	1.00	13.76	1.03	0.95
Spar 1	1.00	9.50	0.67	0.62
Spar 2	1.00	14.97	1.02	0.92
Rib Def. 1	1.00	1.89	0.16	0.14
Rib Def. 2	1.00	4.65	0.45	0.42
Rib Def. 3	1.00	3.21	0.33	0.31

(b) *Stress Sizing Coefficients of Load Case 2*

Parts	Iteration 1	Iteration 2	Iteration 3	Iteration 4	Iteration 5	Iteration 6
Upper Shell	1.00	1.00	1.31	1.08	1.01	1.00
Lower Shell	1.00	4.98	1.63	1.09	1.01	1.00
Spar 1	1.00	1.00	1.00	1.01	1.00	1.00
Spar 2	1.00	1.00	1.00	1.01	1.00	1.00
Rib Def. 1	1.00	1.00	1.00	1.00	1.00	1.00
Rib Def. 2	1.00	3.25	1.23	1.03	1.00	1.00
Rib Def. 3	1.00	1.00	1.13	1.03	1.00	1.00

(c) *Stability Sizing Coefficients of Load Case 1*

Parts	Iteration 1	Iteration 2	Iteration 3	Iteration 4
Upper Shell	1.00	7.97	1.15	1.00
Lower Shell	1.00	1.00	1.09	1.00
Spar 1	1.00	1.00	1.00	1.00
Spar 2	1.00	1.00	1.02	1.00
Rib Def. 1	1.00	1.00	1.00	1.00
Rib Def. 2	1.00	3.29	1.02	1.00
Rib Def. 3	1.00	2.47	1.03	1.00

(d) *Stability Sizing Coefficients of Load Case 2*

Table B.10 *Optimization Results of Topology 10*

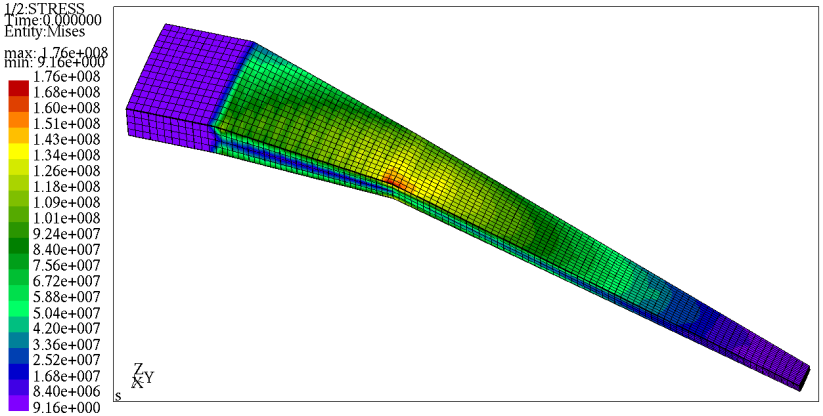

(a) *Stress Distribution of Load Case 1*

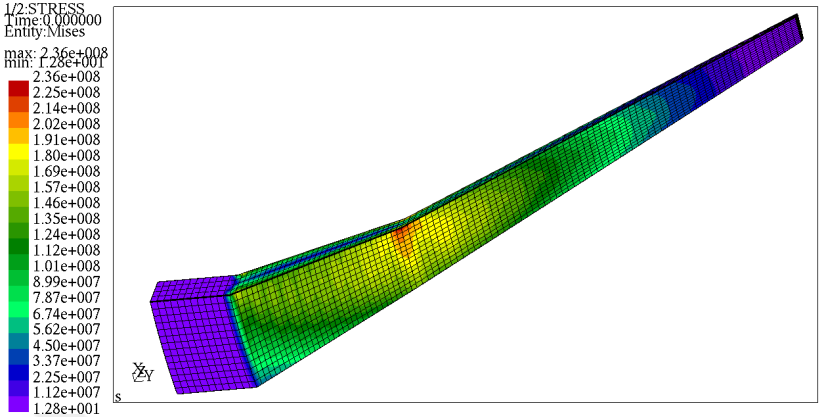

(b) *Stress Distribution of Load Case 2*

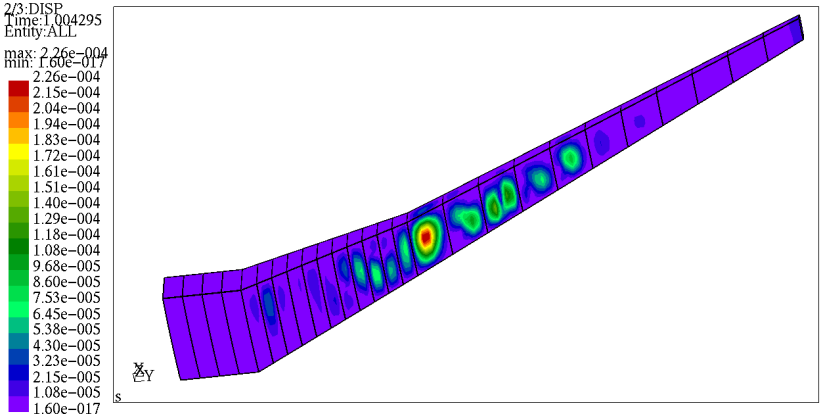

(c) *Buckle Displacements of Load Case 1*

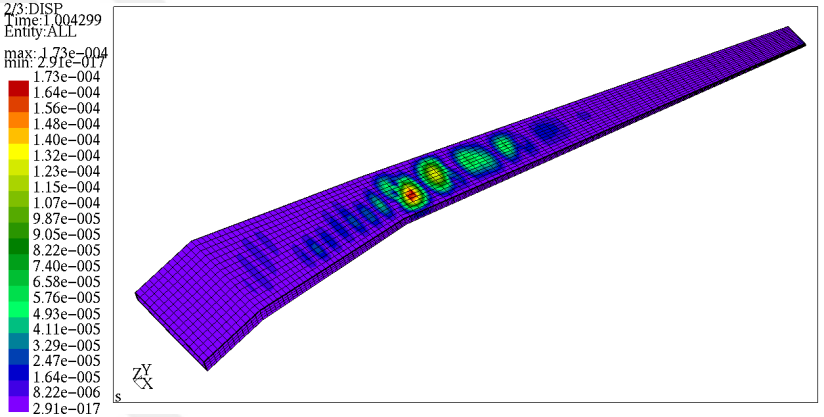

(d) *Buckle Displacements of Load Case 2*

Figure B.10 *Converged FEA Results of Topology 10*

Parts	Iteration 1	Iteration 2	Iteration 3	Iteration 4	Iteration 5	Iteration 6
Upper Shell	1.00	5.98	1.00	0.80	0.78	0.77
Lower Shell	1.00	5.94	1.00	0.67	0.66	0.65
Spar 1	1.00	3.87	0.64	0.50	0.49	0.49
Spar 2	1.00	6.16	1.00	0.79	0.77	0.76
Rib Def. 1	1.00	0.66	0.14	0.11	0.10	0.10
Rib Def. 2	1.00	1.96	0.42	0.32	0.32	0.31
Rib Def. 3	1.00	1.33	0.32	0.26	0.25	0.25

(a) *Stress Sizing Coefficients of Load Case 1*

Parts	Iteration 1	Iteration 2	Iteration 3	Iteration 4	Iteration 5
Upper Shell	1.00	14.56	1.03	0.90	0.89
Lower Shell	1.00	13.80	1.03	0.96	0.95
Spar 1	1.00	9.54	0.67	0.63	0.63
Spar 2	1.00	14.99	1.02	0.93	0.93
Rib Def. 1	1.00	1.81	0.15	0.13	0.13
Rib Def. 2	1.00	4.59	0.45	0.42	0.42
Rib Def. 3	1.00	3.15	0.33	0.31	0.31

(b) *Stress Sizing Coefficients of Load Case 2*

Parts	Iteration 1	Iteration 2	Iteration 3	Iteration 4	Iteration 5	Iteration 6
Upper Shell	1.00	1.00	1.27	1.03	1.01	1.00
Lower Shell	1.00	5.11	1.58	1.02	1.01	1.00
Spar 1	1.00	1.00	1.07	1.00	1.00	1.00
Spar 2	1.00	1.00	1.00	1.00	1.00	1.00
Rib Def. 1	1.00	1.00	1.00	1.00	1.00	1.00
Rib Def. 2	1.00	3.04	1.11	1.01	1.00	1.00
Rib Def. 3	1.00	1.42	1.12	1.01	1.00	1.00

(c) *Stability Sizing Coefficients of Load Case 1*

Parts	Iteration 1	Iteration 2	Iteration 3	Iteration 4	Iteration 5
Upper Shell	1.00	8.18	1.18	1.01	1.00
Lower Shell	1.00	1.00	1.07	1.00	1.00
Spar 1	1.00	1.00	1.00	1.00	1.00
Spar 2	1.00	1.00	1.00	1.00	1.00
Rib Def. 1	1.00	1.00	1.00	1.00	1.00
Rib Def. 2	1.00	3.59	1.04	1.00	1.00
Rib Def. 3	1.00	2.58	1.03	1.00	1.00

(d) *Stability Sizing Coefficients of Load Case 2*

Table B.11 *Optimization Results of Topology 11*

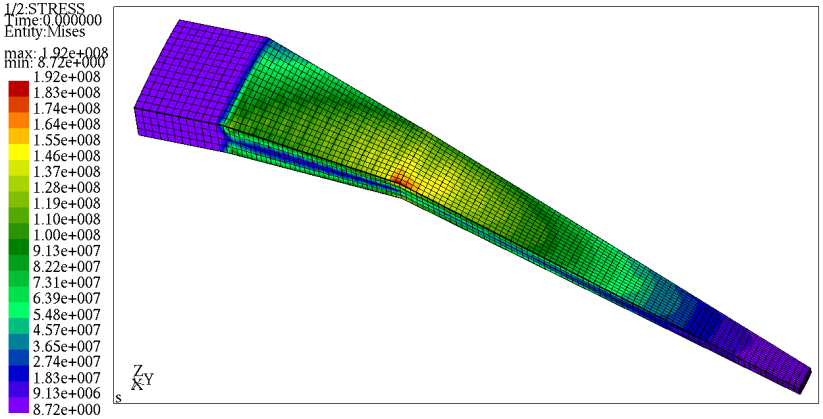

(a) *Stress Distribution of Load Case 1*

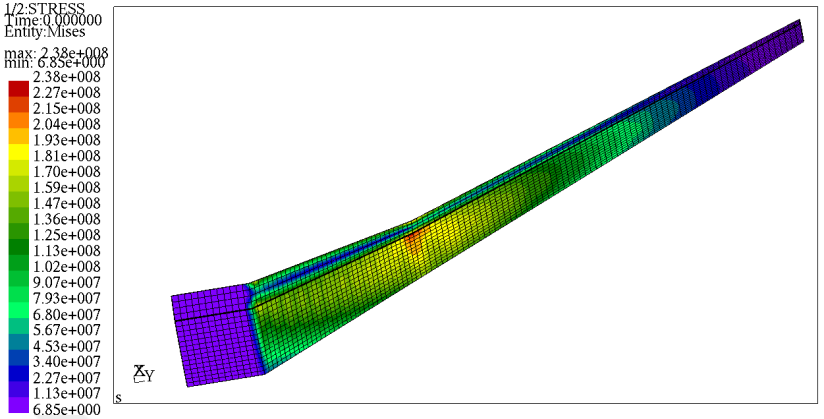

(b) *Stress Distribution of Load Case 2*

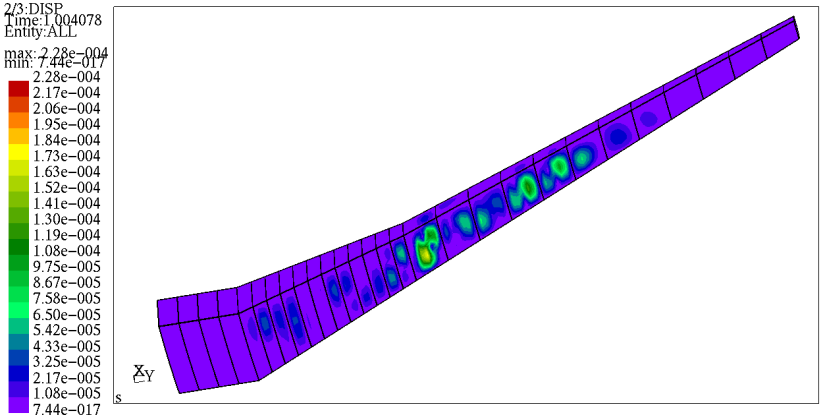

(c) *Buckle Displacements of Load Case 1*

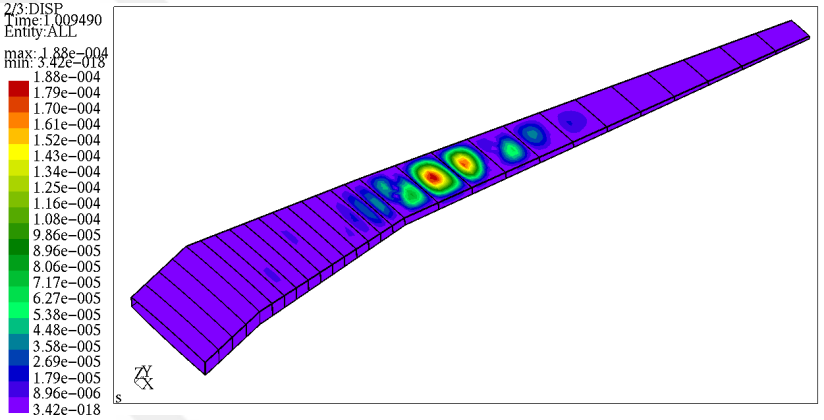

(d) *Buckle Displacements of Load Case 2*

Figure B.11 *Converged FEA Results of Topology 11*

Parts	Iteration 1	Iteration 2	Iteration 3	Iteration 4	Iteration 5
Upper Shell	1.00	5.86	1.02	0.87	0.84
Lower Shell	1.00	5.84	1.02	0.71	0.68
Spar 1	1.00	3.84	0.63	0.54	0.52
Spar 2	1.00	6.03	1.02	0.86	0.83
Rib Def. 1	1.00	0.75	0.16	0.13	0.12
Rib Def. 2	1.00	2.00	0.50	0.42	0.41
Rib Def. 3	1.00	1.36	0.29	0.24	0.23

(a) *Stress Sizing Coefficients of Load Case 1*

Parts	Iteration 1	Iteration 2	Iteration 3	Iteration 4
Upper Shell	1.00	14.26	1.03	1.00
Lower Shell	1.00	13.55	1.02	1.00
Spar 1	1.00	9.45	0.68	0.66
Spar 2	1.00	14.66	1.01	0.98
Rib Def. 1	1.00	2.05	0.18	0.17
Rib Def. 2	1.00	4.64	0.45	0.44
Rib Def. 3	1.00	3.20	0.34	0.33

(b) *Stress Sizing Coefficients of Load Case 2*

Parts	Iteration 1	Iteration 2	Iteration 3	Iteration 4	Iteration 5
Upper Shell	1.00	1.00	1.16	1.04	1.01
Lower Shell	1.00	4.65	1.52	1.05	1.01
Spar 1	1.00	1.00	1.00	1.01	1.00
Spar 2	1.00	1.00	1.06	1.01	1.00
Rib Def. 1	1.00	1.00	1.00	1.00	1.00
Rib Def. 2	1.00	1.67	1.18	1.02	1.00
Rib Def. 3	1.00	2.47	1.11	1.01	1.00

(c) *Stability Sizing Coefficients of Load Case 1*

Parts	Iteration 1	Iteration 2	Iteration 3	Iteration 4
Upper Shell	1.00	7.44	1.03	1.00
Lower Shell	1.00	1.00	1.02	1.00
Spar 1	1.00	1.00	1.00	1.00
Spar 2	1.00	1.00	1.00	1.00
Rib Def. 1	1.00	1.00	1.00	1.00
Rib Def. 2	1.00	1.00	1.00	1.00
Rib Def. 3	1.00	2.85	1.01	1.00

(d) *Stability Sizing Coefficients of Load Case 2*

Table B.12 *Optimization Results of Topology 12*

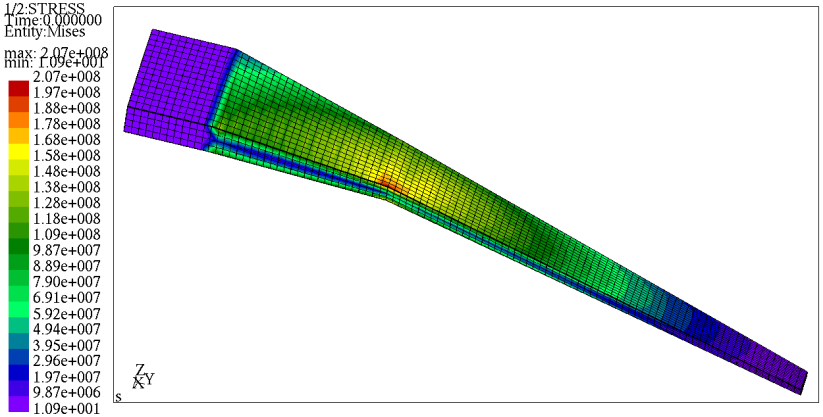

(a) *Stress Distribution of Load Case 1*

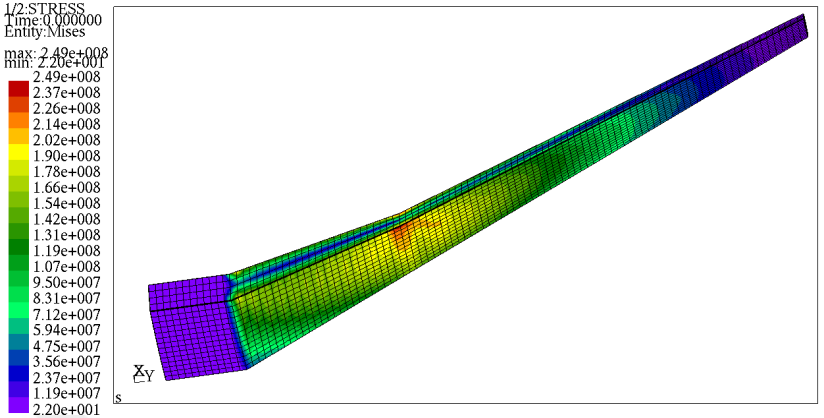

(b) *Stress Distribution of Load Case 2*

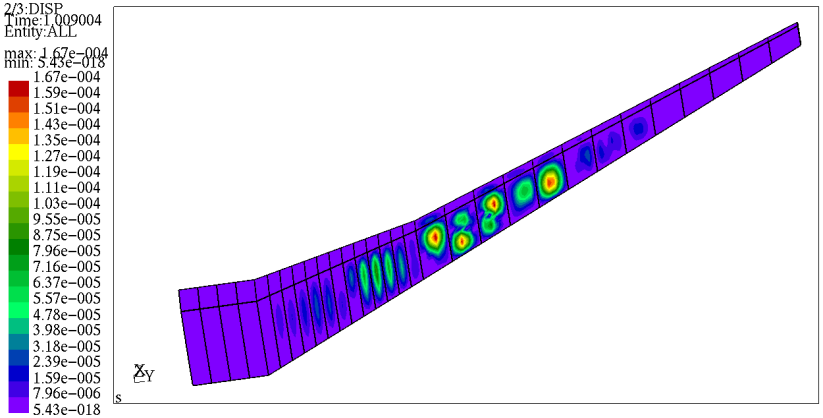

(c) *Buckle Displacements of Load Case 1*

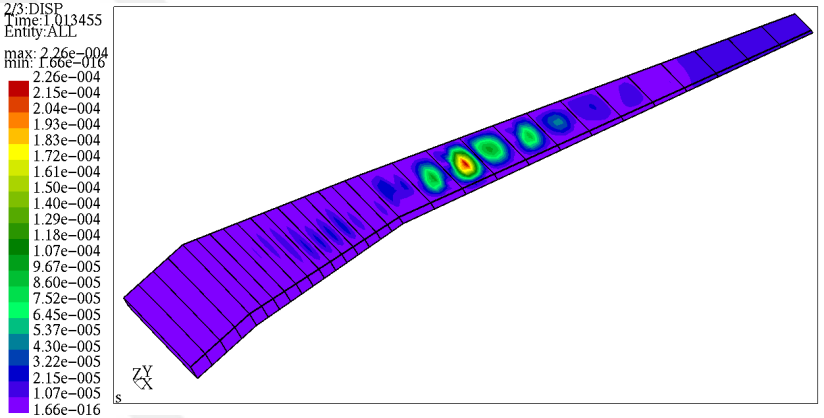

(d) *Buckle Displacements of Load Case 2*

Figure B.12 *Converged FEA Results of Topology 12*

Appendix C

Digital Content

This work is provided beside of paper form, also in digital format with the original materials used during preparation. The original materials were grouped in three separate directories with following names:

SMT_v1.0 contains the initial runable version of the Structural Modeling Tool as MATLAB code, as well as the CPACS input file of the CSR-01 model. The parametric set up condition of the application is as stated in Chapter 5. The structural modeling process in SMT can be started simply by running the "Main.m" file.

Output Files contains the output data of the modeling process and codes for statistical methods. The output data consist of CalculiX input and output files for two separate modeling processes located in own subdirectories named with "CSR01_Wing_12Iterations" and "CSR01_Wing_35Iterations". The first modeling process represent the application that is mentioned in Chapter 5 with 12 iterations, where the latter modeling process is a extended form of the first one with 35 iterations. In each directory, topology optimization results with respect to two introduced load cases were grouped in sub directories, where in each topology group, sizing results were gathered. Also for both directories, an "Output.mat" file was placed with parametric data of the modeling process as well. Images of FEA results from Appendix B were generated from ".frd" files located in "CSR01_Wing_12Iterations" directory using CalculiX Graphix tool. It must be also noted that these files were picked up from the ultimate sizing result in each topology of both load cases, since they represent the converged result.

Literature directory contains the source the material that was gathered during the literature study of thesis. The literature files were grouped under subdirectories for articles, books, dissertations, manuals, presentations and theses. Literature files were named with "*Author Year_Title*" convention, so that the file can be reached by less search effort. Apart from the literature source, the documentation and the XSD tree of CPACS v2.0 can be found in this directory.

Bibliography

[1] Richard von Mises. „Mechanik der festen Körper im plastisch-deformablen Zustand“. In: *Nachrichten von der Gesellschaft der Wissenschaften zu Göttingen* (Nov. 1, 1913), pp. 582–592.

[2] Marvin Minsky. *A Framework for Representing Knowledge*. 1974.

[3] E. Torenbeek. *Synthesis of Subsonic Airplane Design: An introduction to the preliminary design of subsonic general aviation and transport aircraft, with emphasis on layout, aerodynamic design, propulsion and performance*. Springer, 1982. ISBN: 90-247-2724-3.

[4] Karl Heinz Horstmann. „Ein Mehrfach-Traglinienverfahren und Seine Verwendung für Entwurf und Nachrechung nichtplanarer Flügelanordnungen“. DFVLR-FB 87-51. Institut für Entwurfsaerodynamik der Deutschen Forschungs- und Versuchsanstalt für Luft- und Raumfahrt Braunschweig, 1988.

[5] Mike Niu. *Airframe Structural Design: Practical Design Information and Data on Aircraft Structures*. Technical Book Co, 1988. ISBN: 962-7128-04-X.

[6] Peter E. Friedland Edward Feigenbaum. *Expert Systems and Artifical Intelligence*. Study Report. Japanese Technology and Evaluation Center, 1993. URL: `http://www.wtec.org/loyola/kb/toc.htm`.

[7] Hyochoong Bang Young W. Kwon. *The Finite Element Method Using MATLAB*. Taylor & Francis Inc, July 28, 2000. ISBN: 0849300967.

[8] European Commision. *European Aeronautics: A Vision For 2020*. Aircraft and an air transport system that are responding to society's needs, despite a threefold increase in air transport. Luxembourg: Office for Official Publications of the European Communities, 2001. ISBN: 92-894-0559-7.

[9] European Aviation Safety Agency. *Certification Specifications for Large Aeroplanes CS - 25*. Oct. 17, 2003.

[10] Michael Negnevitsky. *Artificial Intelligence. A Guide to Intelligent Systems*. 2005.

[11] M. Najwing, M. J. L. van Tooren, and J. P. T. J. Berends. „Automated Finite Element Analysis in a Knowledge Based Engineering Environment“. In: *44th AIAA Aerospace Sciences Meeting and Exhibit*. American Institute of Aeronautics and Astronautics, Jan. 12, 2006. DOI: `10.2514/6.2006-947`.

[12] Lars Hansen and Peter Horst. „Multilevel Optimization In Aircraft Structural Design Evaluation“. In: *Computers & Structures* 86.1-2 (May 2, 2007), pp. 104–118. DOI: `10.1016/j.compstruc.2007.05.021`.

[13] Johannes Wiedemann. *Leichtbau*. Springer Berlin Heidelberg, Apr. 29, 2007. ISBN: 9783540336570.

[14] Carsten M. Liersch and Martin Hepperle. „A Unified Approach for Multidisciplinary Preliminary Aircraft Design“. In: *CEAS 2009 European Air and Space Conference* (2009). URL: https://elib.dlr.de/63305/.

[15] William J. Fredericks et al. „Aircraft Conceptual Design Using Vehicle Sketch Pad“. In: *48th AIAA Aerospace Sciences Meeting Including the New Horizons Forum and Aerospace Exposition*. American Institute of Aeronautics and Astronautics, Jan. 7, 2010. DOI: 10.2514/6.2010-658.

[16] Florian Hürlimann. „Mass Estimation of Transport Aircraft Wingbox Structures with a CAD/CAE Based Multidisciplinary Process“. PhD thesis. Swiss Federal Institute of Technology in Zurich, June 2010. ISBN: 978-3-909386-46-8.

[17] European Commision. *Flightpath 2050. Europe's vision for aviation : maintaining global leadership and serving society's needs*. Luxembourg: Office for Official Publications of the European Communities, June 11, 2011. ISBN: 978-92-79-19724-6. DOI: 10.2777/50266.

[18] Deutches Zentrum für Luft- und Raumfahrt. *Google Code Arcihe - Long-term storage for Google Code Project Hosting*. Sept. 5, 2011. URL: https://code.google.com/archive/p/cpacs/.

[19] Gianfranco La Rocca. „Knowledge Based Engineering Techniques to Support Aircraft Design and Optimization“. PhD thesis. Delft University of Technology, Apr. 11, 2011. ISBN: 978-90-9026069-3.

[20] Felix Dorbath, Björn Nagel, and Volker Gollnick. „A Knowledge Based Approach for Automated Modelling of Extended Wing Structures in Preliminary Aircraft Design“. In: *60. Deutscher Luft- und Raumfahtkongress*. Sept. 27, 2012.

[21] Felix Dorbath, Björn Nagel, and Volker Gollnick. „A Knowledge Based Approach for Extended Physics-Based Wing Mass Estimation in Early Design Stages“. In: *28th International Congress of the Aeronautical Sciences*. Sept. 23, 2012.

[22] J. Scherer et al. „A Finite Element Based Tool Chain for Structural Sizing of Transport Aircraft in Preliminary Aircraft Design“. In: *62. Deutscher Luft- und Raumfahrtkongress*. Sept. 10, 2013.

[23] European Commision. *What is Horizon 2020?* 2014. URL: https://ec.europa.eu/programmes/horizon2020/en/what-horizon-2020.

[24] Guido Dhondt. *CalculiX CrunchiX USER'S MANUAL Version 2.7*. 2014. URL: http://web.mit.edu/calculix_v2.7/CalculiX/ccx_2.7/doc/ccx/ccx.html.

[25] Guido Dhondt. *Overview of the Finite Element Capabilities of CalculiX Version 2.14*. 2014. URL: http://www.dhondt.de/ov_calcu.htm.

[26] Felix Dorbath. „A Flexible Wing Modeling and Physical Mass Estimation System For Early Aircraft Design Stages“. PhD thesis. Technical University of Hamburg-Harburg, Jan. 10, 2014. DOI: 10.15480/882.1159.

[27] Bernd Klein. *FEM*. Springer Fachmedien Wiesbaden, Dec. 4, 2014. ISBN: 9783658060541.

[28] Vasily Chedrik and Sergey Tuktarov. „Structural Design of Aircraft Wing Based On Topology Optimizaiton and Global-Local Optimization“. In: *11th World Congress on Structural and Multidisciplinary Optimisation*. 2015.

[29] Convergent Mechanical. *bConverged Open Engineering Suite*. 2015. URL: http://www.bconverged.com/.

[30] Kristof Risse et al. „Central Reference Aircraft data System (CeRAS) for research community“. In: *CEAS Aeronautical Journal* 7.1 (2015), pp. 121–133. DOI: 10.1007/s13272-015-0177-9.

[31] Kağan Atçı. „Berücksichtigung der Strukturverformung bei der Erzeugung aerodynamischer Kenndaten im Flugzeug-Vorentwurf“. Bachelor's thesis. Technical University of Berlin, May 15, 2016.

[32] Andreas Schuster et al. „Automated Sizing Process of a complete Aircraft Structure for the Usage within a MDO Process“. In: *65. Deutscher Luft- und Raumfahrtkongress*. Sept. 13, 2016.

[33] Adrian Williams. *Aerospace growth climbs with carbon fiber*. May 25, 2016. URL: https://www.compositesworld.com/columns/aerospace-growth-climbs-with-carbon-fiber.

[34] European Commision. *Turbo electRic Aircraft Design Environment (TRADE) | Projects | H2020 | CORDIS | European Commission*. May 23, 2017. URL: https://cordis.europa.eu/project/rcn/210614_en.html.

[35] Heribert Wessels Klaus Knothe. *Finite Elemente*. Springer Berlin Heidelberg, Jan. 20, 2017.

[36] Daniel Veillard. *The XML C parser and toolkit of Gnome*. Nov. 25, 2017. URL: http://www.xmlsoft.org/.

[37] Technical University of Berlin. *Institut f. Luft- u. Raumfahrt: TRADE*. Ed. by Claire Jacob. July 18, 2018. URL: https://www.luftbau.tu-berlin.de/menue/forschung/trade/.

[38] The Mathworks Inc. *MathWorks - Makers of MATLAB and Simulink - MATLAB & Simulink*. 2018. URL: https://www.mathworks.com/.

[39] Deutsches Zentrum für Luft- und Raumfahrt. *DLR - Simulations- und Softwaretechnik - TiGL (TiGL Geometry Library)*. Ed. by Dr. rer. nat. Martin Siggel. 2018. URL: https://www.dlr.de/sc/desktopdefault.aspx/tabid-12766/22301_read-51485/.

[40] Deutsches Zentrum für Luft- und Raumfahrt. *GitHub DLR-LY/CPACS: CPACS - Common Parametric Aircraft Configuration Schema*. June 7, 2018. URL: https://github.com/DLR-LY/CPACS.

[41] Airbus S.A.S. *A321neo*. 2018. URL: https://www.airbus.com/aircraft/passenger-aircraft/a320-family/a321neo.html#details.

[42] Open Cascade SAS. *OPEN CASCADE*. 2018. URL: https://www.opencascade.com/.

[43] *TiGL: Overview*. 2018. URL: http://tigl.sourceforge.net/Doc/index.html.

[44] *TiXI: 2018*. 2018. URL: http://tixi.sourceforge.net/Doc/index.html.

[45] Daniel Veillard. *The XML C parser and toolkit of Gnome*. 2018. URL: http://www.xmlsoft.org/.

[46] RWTH Aachen, ed. *CeRAS - Central Reference Aircraft data System*. URL: http://ceras.ilr.rwth-aachen.de/.

[47] MatWeb. *ASM Material Data Sheet*. URL: http://asm.matweb.com/search/SpecificMaterial.asp?bassnum=ma2024t4.